Aerodynamics, Scaling, and Performance of a Flexible Flapping Wing

by

Chang-kwon Kang

A dissertation submitted in partial fulfillment
of the requirements for the degree of
Doctor of Philosophy
(Aerospace Engineering)
in the University of Michigan
2011

Doctoral Committee:

Professor Carlos E. Cesnik, Co-Chair
Professor Wei Shyy, Co-Chair
Professor Peretz P. Friedmann
Associate Professor Luis P. Bernal
Associate Professor Yin Lu Young

To my parents and my sister

Acknowledgement

I would like to thank my advisor Prof. Wei Shyy for his guidance, support and patience. His insight and the ability to focus and communicate within and outside research have been inspirational. Much of my development both in professional and personal aspect of life, I owe him for. I would like to thank my co-chair Prof. Cesnik for his guidance and support for the final year of my study and for regarding me as his adopted student. Also, I would like to thank my committee Prof. Bernal, Prof. Friedmann, and Prof. Young for their role in helping finalize the last part of the study.

I would like to thank my group members, office mates in FXB2211, and students in the other side of the FXB for the continuous discussions and entertainment: Knowledge was obtained from the books and classes; however insight and idea were shaped from the interactions and discussions. Especially, I would like to thank Dr. Hikaru Aono, Dr. Amit Gupta, Dr. Pat Trizila, and Dr. Chien-Chou Tseng for the close collaborations and talks during the coffee breaks which I greatly appreciate. Also, I would like to thank the rest of the group members, Dr. Young-Chang Cho, Wenbo Du, Chih-Kuang Kuan, Ez Hassan, Dr. Jaeheon Sim, and Jianing Tang for their support and suggestions and Yee-Chee, Yuntao, Chris, Yongsun, Simon, Ken, Bharat, Brandon, and Clarence for their sympathetic interests.

I would like to thank Dr. Jeff Wright and Dr. ST Thakur for their and support with Loci-STREAM. Without their help and answers to my endless questions the work presented here would not have existed.

I would like to thank Prof. Bernal, Dr. Yeon Baik, and Dr. Michael Ol for the collaboration under RTO of which in part is presented in this dissertation and the invaluable experience of being able to work with.

I would like to thank Prof. Cesnik and Dr. Satish Chimakurthi for their input on the structural dynamics modeling and fluid-structure interaction interface development. I also would like to thank Dr. Abhijit Gogulapati for the fruitful discussions we've had on the flapping wing aerodynamics and aeroelasticity.

I would like to thank the staff in the department not only for their work, but also for creating a friendly environment in the FXB building, in particular Cynthia Enoch, Dave McLean, Denise Phelps, Michelle Shepherd, Sue Smith, and Lisa Szuma.

Finally, I would like to thank my family and friends. I would like to thank my mother, father, and sister for their endless support and love. I would like to thank Dr. Baro Hyun, Dr. Sangmin Lee, and the family of Dr. Insung Kim for making my life warm in Ann Arbor. Also, I would like to thank the weekly tennis group friends, Ambo, Ayaka, Baro, Katsuhide, Ken, Mike, Mitsu, Ryo, Shimpei, Taku, and the previous members, for enjoying playing tennis together which has benefited me a lot. Furthermore, I would like to thank all those that I have not named.

The work supported here has been supported in part by the Air Force Office of Scientific Research's Multidisciplinary University Research Initiative (MURI) grant and by the Michigan/AFRL (Air Force Research Laboratory)/Boeing Collaborative Center in Aeronautical Sciences.

Table of Contents

Dedications……………………………………………………………………………..ii
Acknowledgement iii
List of Figures vii
List of Tables xi
List of Appendices xii
List of Symbols xiii
List of Abbreviation xvi
Abstract xvii
Chapter 1. Introduction 1
1.1 Background and Motivation 1
1.2 Literature Overview 3
1.2.1 Unsteady Aerodynamic Force Enhancement Mechanisms 3
1.2.2 Strouhal Number, Reduced Frequency, and Rigid Wing Aerodynamics 6
1.2.3 Scaling in the Fluid Dynamics, Structural Dynamics, and Aeroelasticity 8
1.2.4 Flexible Wing Structures 11
1.2.5 Aerodynamic Performance of Flexible Flapping Wings 13
1.3 Objectives 15
1.4 Outline 16
Chapter 2. Governing Equations and Numerical Methods 18
2.1 Introduction 18
2.2 Dimensional Analysis and Non-Dimensional Governing Equations 20
2.3 Fluid Dynamics Solver 25
2.4 Turbulence Closure for Flows at $Re = O(10^3 - 10^4)$ 25
2.5 Remeshing 27
2.5.1 Radial Basis Function Interpolation Remeshing 27
2.5.2 Assessment of Remeshing Performance 31
2.6 Structural Dynamics Solver 38
2.7 Fluid-Structure Interaction Interface 38
Chapter 3. Scaling of the Forces Acting on a Moving Body Immersed in Fluid 41
3.1 Introduction 41
3.2 Scaling of Forces 42

3.3 Linearized Aerodynamic Theories 46
3.4 Summary 48
Chapter 4. Fluid Dynamics of Rigid Flapping Wings at $Re = O(10^4)$ and $k = 0.25$ 50
4.1 Introduction 50
4.2 Case Setup 51
4.3 Flow over 2D SD7003 Airfoil at $Re = 6\times10^4$ 52
4.4 Shape Effect: Pitching and Plunging 2D Flat Plate at $Re = 6\times10^4$ 55
4.5 Reynolds Number Effect: $Re = 6\times10^4$ to 1×10^4 for a Pitching and Plunging 2D Flat Plate 58
4.6 Dimensionality Effect: Pitching and Plunging 2D and 3D Flat Plate 63
4.7 Summary 67
Chapter 5. Effects of Flexibility on the Fluid Dynamic Performance of Wings 68
5.1 Introduction 68
5.2 Propulsive Force Generation of Oscillating Flexible Wings 69
5.2.1 Purely Plunging Chordwise Flexible Airfoils in Forward Flight in Water ... 69
5.2.2 Purely Plunging Spanwise Flexible Wings in Forward Flight in Water 75
5.2.3 Lift Generation of a Hovering Isotropic Flapping Zimmerman Wing in Air 80
5.2.4 Scaling Parameterfor the Force Generation 86
5.3 Propulsive Efficiency of Oscillating Flexible Wings 101
5.4 Implications of the Scaling Parameters on the Fluid Dynamic Performance of Oscillating Flexible Wings 107
5.5 Summary 114
Chapter 6. Concluding Remarks 116
6.1 Summary and Conclusions 116
6.2 Main Contributions 120
6.3 Future Work 121
Appendices 124
Bibliography 137

List of Figures

Figure 1-1 Examples of bio-inspired MAVs 2

Figure 1-2 Logarithmic plot of the fire ball radius showing the Taylor's scaling law [61,65]. 10

Figure 2-1 Relevant physical variables shown for a case of hummingbird. The picture is reproduced, by permission, from Wei Shyy © [104]. 21

Figure 2-2 Initial mesh of a two percent thick flat plate in a square domain. Total number of cells, nodes, and boundary nodes are 1224, 1384, and 520, respectively. 32

Figure 2-3 Mesh distribution near the trailing-edge of the flat plate on (a) the initial grid, (b) after rotation, and (c) after translation for the baseline grid (Ng=1). 34

Figure 2-4 Non-smoothness and skewness of the cells on the initial mesh and the rotated mesh for the mesh scalability factors Ng = 1 and 16 of a flat plate in a non-moving square shaped outer boundary under the rotational and translational motions. Note that on the Ng = 16 grid the mesh distribution is not shown for visibility purposes. 35

Figure 2-5 Domain scalabilities of a flat plate in a non-moving square domain under rotation and translation. 36

Figure 2-6 Skewness of the cells on the Ng = 8 grid of a flat plate in a non-moving square shaped outer boundary under the translational motion. Black lines represent the mesh distribution. White arrows indicate the translation motion. 37

Figure 2-7 Skewness contours around a Zimmerman wing mesh after 45 deg flapping motion at once. 37

Figure 2-8 Diagram for time marching loop of fluid-structure interaction. 40

Figure 4-1 Airfoil shapes and the mesh used. 51

Figure 4-2 Time history of effective angle of attack α_e for the pitching and plunging kinematics (red line) and the pure plunging kinematics (blue line). 52

Figure 4-3 $u1*$ contours and the instantaneous streamlines over pitching and plunging SD7003 airfoil at k = 0.25, St =0.08, and at Re = 6×10^4 from numerical, and experimental (UM, AFRL) results. 53

Figure 4-4 $u1*$ contours and the instantaneous streamlines over purely plunging SD7003 airfoil at k = 0.25, St =0.08, and at Re = 6×10^4 from numerical (original SST, modified SST), and experimental (UM, AFRL) results. 54

Figure 4-5 $u1*$ contours and the instantaneous streamlines over pitching plunging flat plate airfoil at k = 0.25, St =0.08, and at Re = 6×10^4 from numerical and experimental (UM, AFRL) results. As a reference the numerical computation of the flow field over the SD7003 airfoil is shown in the first column.................... 56

Figure 4-6 Time histories of pitching and plunging, and pure plunging two-dimensional flat plate (blue line), and SD7003 airfoil (red line) at k = 0.25, and St = 0.04 at Re = 6×10^4.. 57

Figure 4-7 $u1 \ast$ profiles from the numerical and experimental results at constant $x1 \ast = 0.125, 0.25, 0.50, 0.75$, and 0.25 behind the trailing edge at $t \ast = 0.00$ at Re = 1×10^4, 3×10^4, and 6×10^4, k = 0.25, St = 0.04 for the pitching and plunging flat plate. Experimental measurements ×: *Re* = 6×10^4; ○: *Re* = 3×10^4; □: *Re* = 1×10^4; Numerical computations —: *Re* = 6×10^4; —: *Re* = 3×10^4; —: *Re* = 1×10^4; The experimental data are from [132]... 59

Figure 4-8 $u1 \ast$ profiles from the numerical and experimental results at constant $x1 \ast = 0.125, 0.25, 0.50, 0.75$, and 0.25 behind the trailing edge at $t \ast = 0.50$ at Re = 1×10^4, 3×10^4, and 6×10^4, k = 0.25, St = 0.04 for the pitching and plunging flat plate. Experimental measurements ×: *Re* = 6×10^4; ○: *Re* = 3×10^4; □: *Re* = 1×10^4; Numerical computations —: *Re* = 6×10^4; —: *Re* = 3×10^4; —: *Re* = 1×10^4; The experimental data are from [132]... 60

Figure 4-9 Vorticity contours from the numerical and experimental results at $t \ast = 0.500$ for Re = 6×10^4, 3×10^4 and 1×10^4, k = 0.25, St = 0.04 for the pitching and plunging flat plate. The experimental data are from [132]. 61

Figure 4-10 Time histories of (a) lift coefficient and (b) drag coefficient for a pitching and plunging flat plate at k = 0.25, St = 0.04 for Re = 1×10^4, 3×10^4, and 6×10^4. 61

Figure 4-11 Lift coefficient as function of effective angle of attack for a pitching and plunging flat plate at k = 0.25, St =0.04 and Re = 1×10^4, 3×10^4, and 6×10^4........ 62

Figure 4-12 Mean and maximum lift and drag coefficients as function of Reynolds number for the SD7003 airfoil and the flat plate for the pitching and plunging, and the pure plunging at k = 0.25. 63

Figure 4-13 $u1 \ast$ contours and the instantaneous streamlines over pitching and plunging 2D and 3D (AR = 2, 75% span) flat plates at k = 0.25, St =0.04, and at Re = 4×10^4 from the computations. 64

Figure 4-14 $u1 \ast$ profiles from the numerical and experimental results at constant $x1 \ast = 0.125, 0.25, 0.50$, and 0.75 at $t \ast = 0.20$ at Re = 4×10^4, k = 0.25, St = 0.04 for the pitching and plunging 3D flat plate with AR = 2 at 75% span............................ 65

Figure 4-15 Lift coefficient as function of non-dimensional time for pitching and plunging 2D and 3D (AR = 2) flat plates at k = 0.25, St =0.04 and Re = 4×10^4. . 65

Figure 4-16 Q surfaces (a) and spanwise lift distribution (b) to illustrate the difference in the flow structures at the center of the downstroke ($t \ast = 0.25$) and the center of upstroke ($t \ast = 0.25$).. 66

Figure 5-1 Trailing edge displacement as function of non-dimensional time for the purely plunging chordwise flexible airfoils in water in freestream at Re = 9.0×10^3 with $hs* = 1.41\times10^{-3}$ and 0.56×10^{-3} at St = 0.17. The experimental measurements are from [73]. 70

Figure 5-2 Time histories of thrust coefficient contribution due to the teardrop and the flexible plate separately at St = 0.17: (a) response of the teardrop; (b) response of the flexible plate. Extracted from [6]. 71

Figure 5-3 Time histories of thrust and wing tip displacement normalized by the plunge amplitude as function of non-dimensional time. Pressure coefficient and vorticity contours at $t* = 0.25$ for each Strouhal number are shown as well. 72

Figure 5-4 Time-averaged thrust coefficient for a plunging chordwise flexible airfoil at Re = 9.0×10^3 and $\rho* =7.8$ for different flat plate thickness and motion frequencies. The experimental data are extracted from [73]. The symbols on the line indicate the discrete dataset from the experimental measurements. 73

Figure 5-5 Tip deformations of a plunging chordwise flexible airfoil at Re = 9.0×103 and $\rho* =7.8$ for different flat plate thickness and motion frequencies. 74

Figure 5-6 Time history of tip displacements of a plunging spanwise flexible wing at Re = 3.0×10^4 for different wing stiffness, wing density, and motion frequencies. The experimental data are extracted from Ref. [76] and the implicit LES from [95].. 76

Figure 5-7 Time history of thrust coefficient of a plunging spanwise flexible wing at Re = 3.0×10^4 for different wing stiffness, wing density, and motion frequencies. The experimental data are extracted from Ref. [76] and the implicit LES from [95].. 77

Figure 5-8 Pressure coefficient $(p - p\infty)(12/\rho_f U_{ref}^2)$ and vorticity contours at 75% span location for *Flexible* and *Very Flexible* configurations. The arrow indicates the direction of the airfoil motion. 78

Figure 5-9 Time-averaged thrust coefficient of a plunging spanwise flexible wing at Re = 3.0×10^4 for different wing stiffness, wing density, and motion frequencies. The experimental data are extracted from Ref. [76]. The symbols on the line indicate the discrete dataset from the experimental measurements. 79

Figure 5-10 Tip deformations of a plunging spanwise flexible wing at Re = 9.0×10^3 for different wing stiffness, wing density, and motion frequencies. 80

Figure 5-11 Geometry of the Zimmerman planform. 81

Figure 5-12 Time histories of horizontal displacement at the wing tip of an isotropic flapping Zimmerman wing hovering at Re = 1.5×10^3, k = 0.56, and St = 0.25, made of aluminum. 82

Figure 5-13 Design of experiment in logarithmic scale for the design variables $\Pi1$ and $\rho*$. The training points are indicated by cicles and the training points by crosses. 84

Figure 5-14 Surrogate model responses for (a) lift, (b) twist, and (c) bending angles for a flapping isotropic Zimmerman wing at Re = 1.5×10^3 and k = 0.56. 85

Figure 5-15 Tip deformations of a hovering isotropic Zimmerman wing in air at Re = 1.5×10^3 and k = 0.56 for different $\rho*$ and Π_1. The numbers shown next to the markers indicate their case numbers. 86

Figure 5-16 Schematic of the wing approximated as beam and the definitions of the wing deformation w^*, prescribed motion at the root h^*, and the spatial coordinate $x*$. 87

Figure 5-17 Normalized time-averaged force coefficients as function of γ. For the insect flyers the letter c and s correspond to chordwise and spanwise flexibility directions, respectively 97

Figure 5-18 Ratio between maxCL and maxCT multiplied by $hs*$ showing the order of magnitudes of the pressure differentials acting on the flapping Zimmerman wing hovering in air. 98

Figure 5-19 Time-averaged force (thrust or lift) coefficient normalized by the effective stiffness plotted against the maximum relative tip deformations for the current computations. The numbers shown in (c) next to the markers indicate their case numbers 100

Figure 5-20 Propulsive efficiency plotted against the Strouhal number for the chordwise flexible airfoil cases (a) – (b) and the spanwise flexible wing cases (c) – (d). 103

Figure 5-21 Time-average thrust scaling plotted against γ. : chordwise flexible airfoils; ◇: spanwise flexible wings. 104

Figure 5-22 Time-average power input plotted against the Strouhal number 104

Figure 5-23 Time-average power input normalized by $\beta1$plotted against $\gamma2$. : chordwise flexible airfoils; ◇: spanwise flexible wings. 106

Figure 5-24 Propulsive efficiency normalized by $\beta1$plotted against γ. : chordwise flexible airfoils; ◇: spanwise flexible wings. 107

Figure 5-25 Force and propulsive efficiency plotted against the frequency ratio $\omega\omega1$. 111

Figure 5-26 Comparison of the propulsive force and efficiency from the current study and from the measurements obtained by Ramananarivo et al. [69]. 112

List of Tables

Table 2-1 Non-dimensional parameters for the flexible flapping wing systems 22

Table 2-2 Original [117] and modified [116] SST turbulence model 26

Table 2-3 Number of cells, number of nodes, and number of boundary nodes depending on the multiplication factor N_g. 33

Table 2-4 The computational time in components for the translating flat plate in a square domain on the Ng = 8 mesh using single processor. 37

Table 3-1 Summary of the force scaling 49

Table 4-1 Mean and maximum lift and drag coefficients for the investigated Reynolds numbers for the SD7003 airfoil and the flat plate for the pitching and plunging, and the pure plunging at k = 0.25 using the original SST turbulence closure...... 62

Table 5-1. Range of the design variables Π_1 and $\rho *$ with representative examples........ 83

Table 5-2 Range of the non-dimensional parameters considered in this study. The aspect ratio of the two-dimensional chordwise flexible airfoil is set to 1 for the reasons discussed in Section 2.2. The representative Section numbers are shown in the parentheses. 89

Table 5-3 Kinematic, geometric, fluid, and structural parameters for the hawkmoth, bumble bee, and fruit fly obtained from the literature [140,141,142,143,144,70]. 99

Table 5-4 Comparison of the optimal frequency ratios from the values reported in the literature and the current study. 111

Table 5-5 Summary of the scaling proposed. Note β_1 is $\Pi 1$ St k for forward flight in water and Π_1 St $\rho * k$ for hovering flight in air, and $\beta 3$ is St $k\Pi 1$ $1 + 4\pi\rho *$ $hs * \gamma 2$. 113

List of Appendices

Appendix A. Spatial and Temporal Sensitivity Studies 124

A.1 Pitching and Plunging SD7003 at $Re = 6\times10^4$, $k = 0.25$, $St = 0.04$. 124

A.2 Pitching and Plunging Flat Plate at $Re = 6\times10^4$, $k = 0.25$, $St = 0.04$. 125

A.3 Plunging Chordwise Flexible Airfoil in Water at $Re = 9\times10^3$ 127

A.4 Plunging Spanwise Flexible Wing in Water at $\mathrm{Re} = 3\times10^4$, ... 128

A.5 Flapping Zimmerman Wing in Air at $\mathrm{Re} = 1.5\times10^3$, ... 130

Appendix B. Training and Testing Points in the Design of Experiment of the Hovering Zimmerman Wing Case 132

Appendix C. Modal analysis of isotropic Zimmerman wing 135

List of Symbols

A	ratio between the acceleration-reaction force (added mass) and the wing inertia, $A = \pi\,\rho_f c_m/(4\rho_s h_s)$
A_c	cross-sectional area of the wing
AR	aspect ratio of the wing
C_D	drag coefficient
C_F	force coefficient
C_L	lift coefficient
$C_{L,\mathrm{fp},10K,\mathrm{max}}$	max flat plate lift coefficient per unit span at $Re = 1\times10^4$
c_m	mean chord
C_P	power input coefficient
C_p	pressure coefficient, $C_p = (p - p_\infty)/\left(\frac{1}{2}\rho_f U_{\mathrm{ref}}^2\right)$
C_T	thrust coefficient
E	Young’s modulus
F	force acting on a body, such as a wing
$\boldsymbol{F}_\Gamma$	Fluid solver acting on a fluid-structure interaction interface Γ
g	acceleration of gravity
h	non-dimensional plunging position as function of time
h_a	plunging amplitude
h_s	thickness of the wing
h_s^*	thickness ratio
I	second moment of inertia
k	reduced frequency of pitch or plunge, $k = \omega c_\mathrm{m}/(2U_\infty)$ for forward flight; $k = c_m/(2h_a)$ for hover (plunging) based on the maximum tip velocity

k_t	turbulence kinetic energy
p	pressure
p_∞	reference pressure at infinity
$P_t, \tilde{P}_t$	production of turbulence kinetic energy
r	radial basis function radius of influence
$\boldsymbol{r}$	residual of the fluid-structure interaction coupling
R	half span of the wing
Re	Reynolds number, $Re = \rho_f U_\infty c/\mu$
$\boldsymbol{S}_\Gamma$	Structural solver acting on a fluid-structure interaction interface Γ
St	Strouhal number, $St = \omega h_\mathrm{a}/c_\mathrm{m}$
t	time
T	temporal part of the separation of variables: $v(x,t) = X(x)T(t)$
T	airfoil oscillation period, $T = 2\pi/\omega$
u_i	velocity vector
$\bar{u}_i$	mean velocity vector normalized with U_∞
U_∞	free stream (forward) velocity
v	wing displacement relative to the motion at the wing root
V	fluid domain
w	wing displacement
x_i	position vector
x_p	pitch pivot point: fraction of chord downstream from airfoil leading edge
X	spatial part of the separation of variables: $v(x,t) = X(x)T(t)$
α	kinematic angle of incidence due to pitch
α_0	geometric angle of attack
α_a	pitching amplitude
α_e	effective angle of attack
$\beta_1, \beta_2, \beta_2$	normalization coefficients
γ	scaling parameter
Γ	fluid-structure interaction interface

η	propulsive efficiency
θ	twist of the wing
μ	viscosity coefficient
μ_t	eddy viscosity
ν	Poisson's ratio
ξ_{i}	vorticity
Π_0	effective inertia, $\rho^* h_s^* (k/\pi)^2$
Π_1	effective stiffness
ρ_f	fluid density
ρ_s	wing structure density
ρ^*	density ratio, ρ_s/ρ_f
ω	angular motion frequency
ω_t	specific dissipation
σ	radial basis function
τ	relaxation parameter for fluid-structure interaction coupling
τ_{ij}	Reynolds stress
ϕ	flap angle, phase lag between plunge and pitch, or velocity potential
Φ	phase lag between the tip and the root of the wing
ϕ_a	flap amplitude
ψ	bending of the wing
Ψ	scaling function for C_F
Ω	control volume
$\partial\Omega$	boundary of the control volume Ω
$(\ )^*$	non-dimensional variables
$(\ )'$	spatial derivative
$(\dot{\ })$	temporal derivative
$\sim$	proportional to: $a \sim b$ means a is a constant multiple of b
$\approx$	approximately: $a \approx b$ means a is approximately equal to b involving some simplifications

List of Abbreviation

AFRL:	Air Force Research Lab
CFD:	Computational Fluid Dynamics
CSD:	Computational Structural Dynamics
FSI:	Fluid-Structure Interaction
iLES:	implicit Large Eddy Simulation
LE:	Leading Edge
LES:	Large Eddy Simulation
LEV:	Leading Edge Vortex
MAV:	Micro Air Vehicle
PDE:	Partial Differential Equation
PIV:	Particle Image Velocimetry
RANS:	Reynolds Averaged Navier-Stokes
RBF:	Radial Basis Function
SST:	Shear Stress Transport
TE:	Trailing Edge
TEV:	Trailing Edge Vortex
TKE:	Turbulence Kinetic Energy
UM:	University of Michigan

Abstract

Effects of flexibility on the force generation and the propulsive efficiency of flapping flexible wings are elucidated. First, based on a control volume analysis around a moving body immersed in viscous fluid, different types of forces, as a function of the Reynolds number, reduced frequency, and Strouhal number, acting on the moving body are identified based on a scaling argument. i) At the Reynolds number regime of $O(10^4)$ and reduced frequency of 0.25 the vortex force term is the most dominant: for a thin rigid flat-plate massive leading-edge separation is observed due to its sharp leading-edge under a combined pitch-plunge kinematics. This geometric effect is seen to dominate over the viscosity effects, such that the Reynolds number dependence on both the flow field and the lift is small. Compared to a SD7003 airfoil with blunter leading-edge, small radius of curvature in the leading-edge of the flat-plate leads to an earlier and stronger leading-edge vortex, which enhances the resulting lift; ii) At the Reynolds number regime of $O(10^3 - 10^4)$ and the reduced frequency of $O(1)$, the added mass forces, which are proportional to the acceleration of the wing, are dominant. In this parameter space, chordwise, spanwise, and isotropic flexibilities are considered to identify the dominant mechanisms in the force generation and propulsive efficiency of flapping wings. By modeling the wing as a linear beam, a relationship between the propulsive force and the maximum relative wing tip deformation is established by considering the energy balance of the wing: The lift generation of insect flyers, approximated by its weight, largely follows the same scaling relationship. Furthermore, a scaling for the propulsive efficiency is found. The current study predicts that the maximum propulsive force is obtained when the motion is near the resonance, whereas the optimal propulsive efficiency is reached when the wing flaps at about half of the natural frequency, consistent with the results reported in the literature. The resulting scaling parameter, given as a combination of *a priori* known wing geometry, structural and fluid properties, and motion kinematics, helps to gain more insight in the combined fluid and structural dynamics.

Chapter 1.
Introduction

1.1 Background and Motivation

The flapping mechanisms inherent to the biological flyers, such as insects and birds, have inspired the most exotic dreams, ever since the history of human beings, from Daedalus and Icarus in the Greek mythology, via Leonardo Da Vinci's ornithopter, to a recent successfully sustained human powered flapping flight [1] at human scale of $O(1\text{ m})$. At smaller scales of 15 cm or less, micro air vehicles (MAVs) are of great interest in remote sensing and information gathering capabilities both in military as well in civilian applications. Smaller sizes and lower flight speeds lead to lower Reynolds numbers and higher sensitivity to wind gust effects than for the conventional airplanes. Furthermore, wing structures of MAVs are often made flexible and deform during flight [2,3,4,5,6]. Because of the common characteristics shared by MAVs and biological flyers, the aerospace and biological science communities are now actively communicating and collaborating.

Recently, a bio-inspired bird-like MAV has successfully demonstrated its ability to hover (Nano Hummingbird) [7]. At larger scales of wing span of two meters (SmartBird) [8] a bird-like flapping motion was integrated into fully automated robotic flyer, see Figure 1-1. Other examples of MAVs are the Delfly [9], Microrobotic Fly [10], among others. In order to operate under wind gust, to avoid objects, or to hover, highly deformed wing shapes and coordinated wing-tail movement in the biological flight are often observed. Understanding the aerodynamic, structural, and control implications of these modes is essential for the development of high performance and robust flapping wing MAVs for accomplishing desirable missions. Moreover, the large flexibility of the wings leads to complex fluid-structure interactions, while the kinematics of flapping and the spectacular maneuvers performed by natural flyers result in highly coupled nonlinearities in fluid dynamics, structural dynamics, flight dynamics, and control systems.

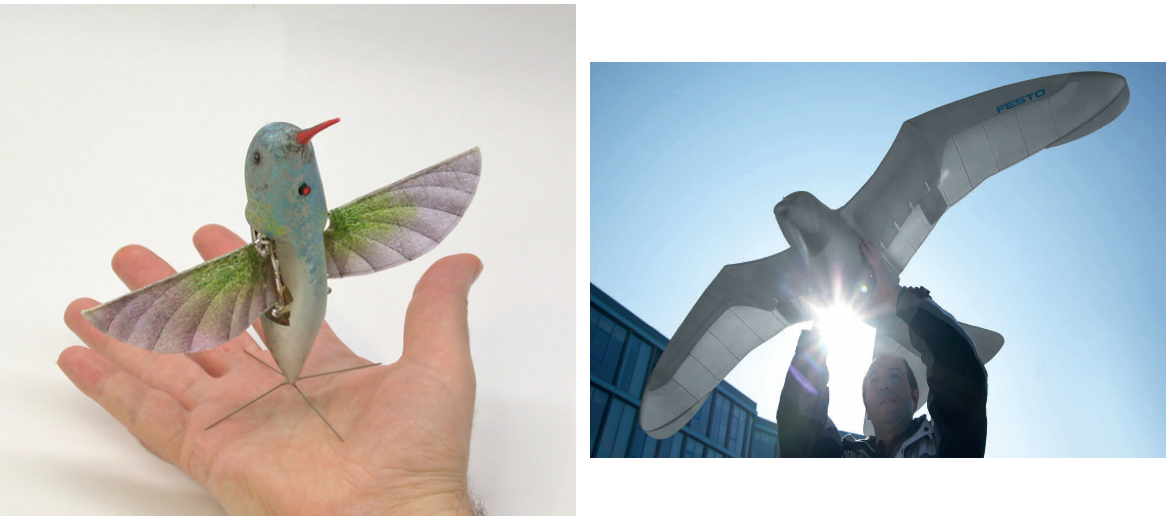

(a) nano hummingbird,
AeroVironment [7]

(b) SmartBird,
Festo [8]

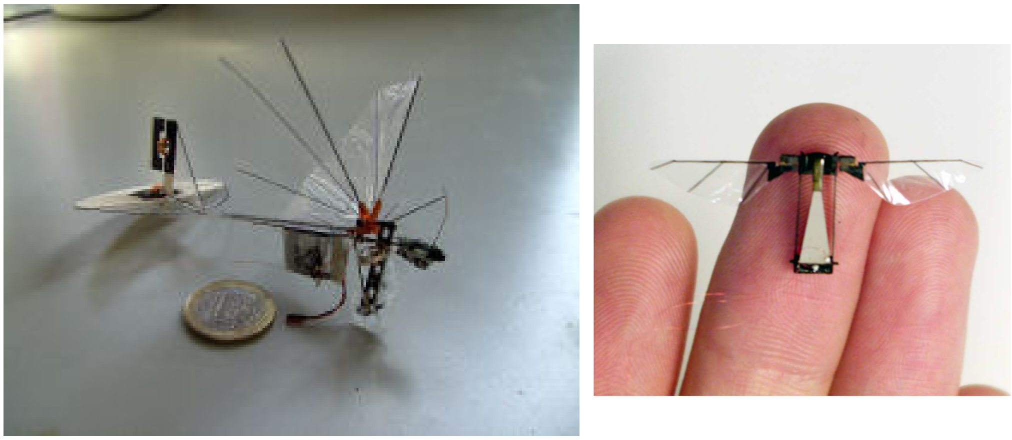

(c) Delfly Micro,
Delft University of Technology [11]

(d) Microrobotic Fly,
Harvard University [10]

Figure 1-1 Examples of bio-inspired MAVs

As reviewed and illustrated by numerous studies [3,6,12,13,14,15,16,17,18,19], biological flyers showcase desirable flight characteristics and performance objectives and the strategies exhibited in nature have the potential to be utilized in the design of flapping wing MAVs. In particular, wing flexibility is likely to have a significant influence on the resulting aerodynamics. Based on a literature study, see Section 1.2, it was found that several questions in flexible wing aerodynamics have not been adequately addressed in the existing literature, among which, the key ones include: (i) What are the dominant non-dimensional parameters, e.g., the Reynolds number (Re) that indicates the ratio of the fluid dynamic inertial forces to the viscous forces, the Strouhal number (St) giving the ratio between the wing velocity to the fluid convection velocity, the reduced frequency (k) that measures the unsteadiness of the flow, and the effective stiffness defined as the wing rigidity normalized by the fluid dynamic pressure, etc., for the aerodynamic performance of flexible flapping wings? (ii) What are the underlying mechanisms of force generation or propulsive efficiency of flexible flapping wings? (iii) Do optima exist for the aerodynamic performances? If so, what are these and how do these optima relate to the non-dimensional parameters listed above? This dissertation explores these questions using high-fidelity computational models and analytic scaling methods.

1.2 Literature Overview

1.2.1 Unsteady Aerodynamic Force Enhancement Mechanisms

The fluid dynamics of flapping wings is inherently related to the unsteadiness of the flow field due to the motion of the wing. The unsteady aerodynamic mechanisms that natural flyers utilize to generate lift and thrust have been discussed and reviewed extensively in the literature [3,6,18,17,20] and this section will only highlight the main results.

Clap and fling

Weis-fogh [16] studied the wing motion of a chalcid wasp, *Encarsia Formosa* and observed that a chalcid wasp claps two wings together and then flings them open about the horizontal line of contact to fill the gap with air. During the fling motion, the air around each wing acquires circulation in the correct direction to generate additional lift to stay aloft, that otherwise could not have been explained based on the steady-state approximation. The clap-and-fling mechanism is beneficial in producing a time-averaged lift coefficient to keep a low weight flyer aloft: it has been observed by hawkmoths, butterflies, fruitflies, wasps, and thrips [16,21,22,23,24,25]. The Delfly flapping-wing MAV, which has the ability to hover, also uses this mechanism to enhance its unsteady lift generation [9].

Wake capture

The wake capture mechanism is observed during a wing-wake interaction. When the wings reverse their translational direction, the wings meet the wake created during the previous stroke, by which the effective flow velocity increases and an additional aerodynamic force peak is generated. Lehmann, Sane and Dickinson [26], Dickinson et al. [27], and Birch and Dickinson [28] examined the effect of wake capturing of several simplified fruit fly-like wing kinematics using a dynamically-scaled robotic fruit fly wing model at Re= 1.0 to 2.0×10^2. They compared the force measurement data with the quasi-steady approximation, and then isolated the aerodynamic influence of the wake. Results demonstrated that wake capture force represented a truly unsteady phenomenon dependent on temporal changes in the distribution and magnitude of vorticity during stroke reversal. Wang [20] and Shyy et al. [3,29] clarified the wake capture mechanism and lift augmentation of the instantaneous lift peak using two-dimensional numerical simulations. The effectiveness of the wake capture mechanism was a function of wing kinematics and flow structures around the flapping wings [3,26,27,28].

Leading Edge Vortex

One of the main unsteady lift mechanisms is suggested by Ellington et al. [30,31,32] that the delayed stall of leading edge vortex (LEV) can significantly promote lift associated with a flapping wing. The LEV creates a region of lower pressure above the wing and hence it would enhance lift. Multiple follow-up investigations [33,34,35] were conducted for different insect models, resulting in a better understanding on the role played by the LEV and its implications on lift generation. When a flapping wing travels several chord lengths, the flow separates from the leading and trailing edges, as well as at the wing tip, and forms large organized vortices, a LEV, a trailing edge vortex (TEV), and a tip vortex (TiV). In flapping wing flight, the presence of LEVs is essential to delay stall and to augment aerodynamic force production during the translation of the flapping wings. Employing three-dimensional NS computations, Liu and Aono [36] and Shyy and Liu [35] demonstrated that a LEV is a common flow feature in flapping wing aerodynamics at Reynolds numbers O(10^4) and lower, which correspond to the flight regime of insects and flapping wing MAVs. However, main characteristics and implications of the LEV on the lift generation varied with changes in the Reynolds number, the reduced frequency, the Strouhal number, the wing flexibility, and flapping wing kinematics [6].

Tip Vortex

Tip vortices associated with fixed finite wings in steady flows are seen to decrease lift and induce drag [37]. However, in unsteady flows, TiVs can influence the total force exerted on the wing in three ways: i) creating a low pressure area near the wing tip [29,38,39], ii) interacting with the LEV and the TiV [29,38,39], and iii) constructing wake structure by downward and radial movement of the root vortex and TiV [71]. The first two mechanisms ((i) and (ii)) also were observed for impulsively started flat plates normal to the motion with low aspect ratios: Riguette et al. [40] presented experimentally that the TiVs contributed substantially to the overall plate force by interacting with the LEVs at $Re = 3.0\times10^3$. Taira and Colonius [41] utilized the immersed boundary method (IBM) to highlight the 3-D separated flow and vortex dynamics for a number of low aspect ratio flat plates at different angles of attacks. At Re of 3.0×10^2 to 5.0×10^2, they showed that the TiVs could stabilize the flow and exhibited nonlinear interaction with the shed vortices. Stronger influence of downwash from the TiVs resulted in reduced lift for lower aspect ratio plates.

For flapping motion in hover, however, depending on the specific kinematics, the TiVs could either enhance or degrade the aerodynamics of a low aspect ratio flapping wing. Shyy et al. [29] demonstrated that, for a flat plate with $AR = 4$ at $Re = 64$ with delayed rotation kinematics, the TiV anchored the vortex shed from the leading edge increasing the lift compared to a two-dimensional computation under the same kinematics. On the other hand, under different kinematics with small angle of attack and synchronized rotation, the generation of TiVs was small and the aerodynamic loading was captured by the analogous 2-D computation. They concluded that the TiVs could either promote or have small impact on the aerodynamics of a low aspect ratio flapping wing by varying the kinematic motions.

Passive pitch

Wing torsional flexibility can allow for a passive pitching motion due to the inertial forces during wing rotation at stroke reversals [42]. There are three modes of passive pitching motions which were similar to those suggested by rigid robotic wing model experiments [27]; i) delayed pitching, ii) synchronized pitching, and iii) advanced pitching. It was found that the ratio of flapping frequency and the natural frequency of the wing were important to determine the modes of passive pitching motions of the wing [42,43]. When the flapping frequency was less than the natural frequency of the wing, the wing experienced an advanced pitching motion, which led to lift enhancement by intercepting the stronger wake generated during the previous stroke [43,44,45]. Moreover, it was shown for two-dimensional flows, the LEVs produced by the airfoil motion with passive pitching seemed to attach longer on the flexible airfoil than on a rigid airfoil [42].

1.2.2 Strouhal Number, Reduced Frequency, and Rigid Wing Aerodynamics

The relation between the fluid physics and the non-dimensional parameters, such as the Strouhal number or the reduced frequency has been investigated extensively in the literature, mostly for rigid wings. The interplay between kinematics, wing shapes, and the resulting forces and flow structures were investigated. In forward flight, the reverse von Kármán vortex street was characteristic for a thrust generating flapping wing [46,47,48,49,50]. A von Kármán vortex street is a well-known unsteady viscous flow behavior at the Reynolds number regime of O(100) behind a blunt object, such as a circular cylinder. The two attached eddies behind the cylinder grow in size and start to alternate as the Reynolds number increases from O(10) to O(100) resulting in unsteady force generation on the cylinder. Depending on the prescribed kinematics of the periodically oscillating wings, the wake behind the wing would show similar flow topology as the von Kármán vortex street, but with reversed direction of the vorticity distribution, hence the nomenclature. If the LEV and the TEV shed from oscillating wing would have the correct alignment [48], which is called the reverse von Karman vortex street, the resulting induced velocity would be such that characterizes propulsion [46,47].

Furthermore, the thrust generation and the propulsive efficiency was observed to be dependent on the Strouhal number: [51,52,53,54,55,56], with the optimum efficiency obtained for Strouhal numbers in the range of 0.01 – 0.235 [51,52,53]. Anderson et al. [49] considered harmonically oscillating NACA0012 airfoils in a water tunnel to measure the thrust. After a parametric study as a function of the amplitude of the angle of attack (α_a), plunge amplitude, and the phase lag between pitch and plunge (ϕ) to find the optimum flow condition for the thrust generation at Re= 4.0×10^4, k = 0.5, St = 0.15 – 0.2, α_a = 30 deg, ϕ = 75 deg) they show that the presence of a reverse von Kármán vortex street formed by the vortices shed from the leading and trailing edges for St in the range of 0.15 and 0.2 at Re= 1.1×10^3. Triantafyllou and co-workers [51,52,53] also performed parametric investigations using experiments in a water tunnel on the performance of a pitching and plunging NACA0012 airfoil in forward flight at Re between 2.0×10^4 and 4.0×10^4, and St between 0.05 and 0.23. Systematic measurements of the fluid force showed a unique peak efficiency of more than 70% for the optimal combinations of the parameters (k = 0.5, St = 0.13, α_a = 15 deg, ϕ = 90 deg) and higher thrust could be expected when increasing the Strouhal number and/or the amplitude of the angle of attack. Lai and Platzer [54] used Laser Doppler Velocimetry and dye injection techniques to visualize the velocity field and the wake structures of an oscillating NACA0012 airfoil in water at Re ranging from 5.0×10^2 to 2.1×10^4. The transition from drag to thrust was found for $St > 0.13$.

Under the Research and Technology Organization (RTO) arrangement of the North Atlantic Treaty Organization (NATO), there was a community-wide effort organized, which offered a wide range of experimental and computational data for both SD7003 airfoil and flat plate, with kinematics causing different levels of flow separation. The detailed information can be found in [57]. For of Re (10^4) and higher, turbulence influences the development of the flow structures and forces. Baik et al. [58] investigated the fluid physics at $Re = O(10^4)$ of a pitching and plunging SD7003 airfoil and flat plate, experimentally using PIV focusing on the second order turbulence statistics. They observed laminar boundary layer and laminar-to-turbulence transition. Baik et al. [59] conducted an experimental study of a pitching and plunging flat plate at $Re = 1.0\times10^4$ where the motion kinematics and flow parameters were such that the resulting time history of effective angle of attack was purely sinusoidal. The effect of non-dimensional parameters governing pitching and plunging motion including Strouhal number, reduced frequency, and the plunge amplitude was investigated for the same effective angle of attack kinematics. The formation phase of the LEV was found to be dependent on k: the LEV formation is delayed for higher k value. It was found that, for cases with the same k, the velocity profiles normal to the airfoil surface closely follow each other in all cases independent of pitch rate and pivot point effect. Visbal et al. [60] computed the unsteady transitional flow over a plunging two-dimensional and three-dimensional SD7003 airfoil with high reduced frequency (k= 3.93) and low plunge amplitude ($h_\mathrm{a}/c_\mathrm{m}$= 0.05) using implicit Large Eddy Simulations (iLES) at $Re = 1.0\times10^4$ and 4.0×10^4. The results showed that the generation of dynamic-stall-like vortices near the leading edge was caused by motion-induced high angles of attack and three-dimensional effects in vortex formation around the wing.

1.2.3 Scaling in the Fluid Dynamics, Structural Dynamics, and Aeroelasticity

Scaling parameters resulting from dimensional analysis help identify key characteristics of the model. The Buckingham's Π-theorem reduces the number of involved parameters to a sufficient number of combinations [61,62,63,64]. The Π-theorem states that a physical relationship between a dimensional variable and other dimensional governing parameters can be rewritten as a relationship between a dimensionless parameter and a number of dimensionless combinations parameters where this number is equal to the difference between the total number of governing parameters and the number of fundamental dimensions in the system. Examples of the well-known dimensionless parameters appearing in fluid dynamics are Reynolds number, Mach number, Strouhal number, Froude number, etc. One of the first examples of such use of scaling and its self-similarity is the G.I. Taylor's analysis of a basic intermediate stage of a nuclear explosion [61,65]. By considering the conservation equations and under several simplifying assumptions, he was able to obtain a scaling law for the radius of the shock wave which propagates inside the atmosphere due to the explosion, see Figure 1-2. Another famous example in the field of fluid dynamics is Kolmogorov's K41 theorem that states that the smallest scales in turbulence are universal and only depend on the the energy dissipation per unit mass and the kinematic viscosity of the fluid. Dimensional analysis is applicable to all physical relationships because it is based on the fundamental covariance principle that all physical relationships can be represented in a form that is equally valid for all observers [61]. Under certain circumstances, the result obtained from the dimensional analysis can be reduced to a simpler relation with a reduced number of arguments as a property of the special problem under consideration. An example hereof is the power law and the universal logarithmic law in the vicinity of the wall in a turbulent flow [61]. Furthermore, the non-dimensional parameters arising from a dimensional analysis can lead to physical similarity, often critical when an exact mathematical formulation is missing [61]. Physical phenomena are called similar if they only differ in the numerical value of the governing parameters and are equal in the corresponding non-dimensional parameters. Such concepts are used to measure fluid flow characteristics around a scaled-down airplane model in wind tunnels to determine actual flow field conditions.

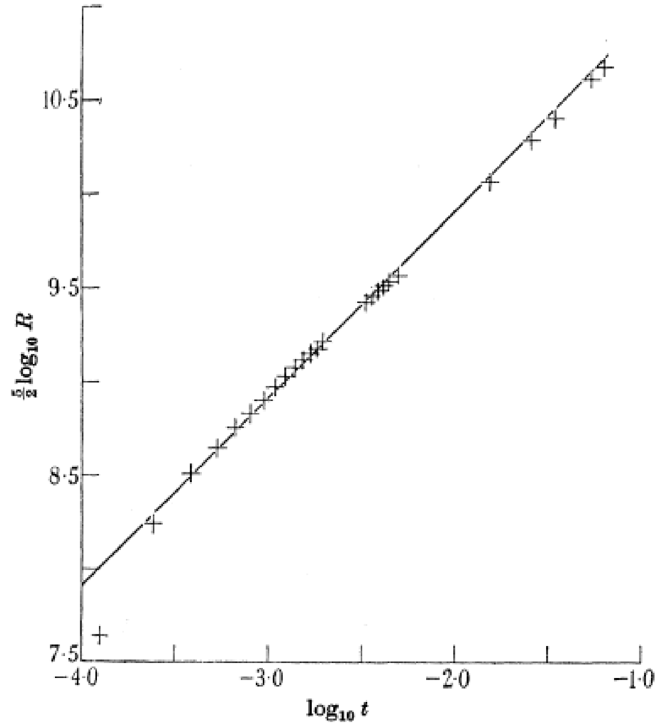

Figure 1-2 Logarithmic plot of the fire ball radius showing the Taylor's scaling law [61,65].

In the field of flexible flapping wing aerodynamics numerous efforts using scaling arguments have increased our knowledge of the complex interplay between flexibility and resulting aerodynamics. Depending on the type of the model and the governing equations the resulting set of scaling parameters may vary. For example, for flexible flapping wings, Shyy *et al.* [6] considered the Navier-Stokes equation for out-of-plane motion of an isotropic flat plate and Chimakurthi [66] non-dimensionalized the anisotropic flat plate equation. Ishihara *et al.* [43] investigated the Navier-Stokes equation along with the linear isotropic elasticity equations to study the effects of flexibility on wing pitch changes in dipteran flapping flight. Furthermore, Ishihara *et al.* [67] have measured the lift generated by a dynamically scaled flexible wing model. They introduced the Cauchy number that describes the ratio between the fluid dynamic pressure and elastic reaction force and presented correlation between time-averaged lift and the Cauchy number. More recently, Thiria and Godoy-Diana [68] and Ramananarivo, Godoy-Diana, and Thiria [69] have measured the thrust and the propulsive efficiency of a self-propelled flapping flyer with flexible wings in air. Since the density ratio is high, the elastic deformation of the wing was mostly balanced by the wing inertia. They have introduced the elastoinertial number using scaling arguments to define the ratio between the inertial forces and the elastic restoring forces and showed that the measured thrust scales with the elastoinertial number. Furthermore, in Ref. [69] a nonlinear damping term was linked to the effects of flexibility on the aerodynamic performance. It should be mentioned that these two studies only consider a portion of the parameter-space and for example the effects of density ratios on the force generation of flexible flapping wings have not been considered. Hence, the parameter-space involving the scaling parameters for the fluid-structure interaction needs to be mapped out in a systematic fashion to understand the role of flexibility and density ratio on the fluid dynamic force generations and the propulsive efficiency of coupled systems.

1.2.4 Flexible Wing Structures

Small size flapping flyers such as insects have flexible wing structures. Their wing structures are complex to model since wings are made up of an extremely thin membrane with veins running throughout. Combes and Daniel [70] have shown that a variety of insects possess anisotropy in their wing structures. The spanwise flexibility was 1 or 2 orders of magnitudes larger than the chordwise flexural rigidity. Although research has been conducted to assess the effects of orthotropic wings (e.g. [71,72]), due to the complexity inherent to the nonlinear fluid flow coupled to the anisotropic wing structures with large deformations, most investigations were on simplified wing structural models to assess the benefit of structural flexibilities in force generation. For forward flight, Heathcote and Gursul [73], Zhao *et al.* [44], and Shyy *et al.* [6] established that the chordwise flexibility affects the redistribution of the resulting fluid forces in the lift and the thrust directions. The airfoil shape undergoes deformation leading to camber variation and modified effective angle of attack, resulting in enhanced thrust generation. In parallel, Gopalakrishnan and Tafti [74] showed that the force generation for an oscillating linear membrane in forward flight increases due to camber deformation resulting in delayed leading-edge vortex detachment. They analyzed the effects of chordwise flexibility of a rectangular membrane flapping wing on aerodynamics using a linear elastic membrane solver coupled with an unsteady LES method. The membrane pre-stresses were varied to assess the camber effects on the aerodynamic loading. On the other hand, for rigid wings, which were also considered, the leading edge vortex lifted off from the surface resulting in low force production. Similar LEV – deformed wing interaction leading to better performance was experimentally observed and reported by Zhao et al. [44]. Gulcat [75] reported that the viscous effects obtained by the unsteady boundary-layer solution show very little alteration to the oscillatory behavior of the net propulsive force. They only reduced the amplitude of the leading edge suction force obtained by the unsteady aerodynamic theory. It was found that the major contribution to the thrust is due to heaving plunging; therefore, it is possible to get high propulsion efficiency with limited camber flexibility.

With spanwise flexibility, a thrust enhancement was seen when the wing motion was in phase with the variation of the wing deformation in spanwise direction [76,77,6]. For flapping flexible wings in hover, Eldredge, Toomey, and Medina [78] found that a hovering flexible airfoil allows for lift generation even when the leading edge remains nearly vertical, as the airfoil passively deflects to create an effectively smaller angle of attack, similar to the passive pitching mechanism recently identified for rigid wings [6]. Furthermore, Ishihara *et al*. [67] showed that the wing torsional flexibility leads to an advanced pitching motion in cranefly hovering that can increase the lift by intercepting the wake from the previous stroke [3]. Despite the identification of benefit of flexural wing structures to the fluid dynamic performance, there are many parameters involved and a clear description and quantification of the role of these parameters and associated physical mecanisms for force generation is still lacking. The fluid-structure density ratio also affects the thrust generation: Zhu [79] has shown numerically that the thrust and the propulsive efficiencies increased for a plunging chordwise flexible airfoil in water than immersed in air. Hence structural flexibility, including the density ratio, seems capable of substantially influencing forces generated from wing motion. Daniel and Combes [80] and Combes and Daniel [81] have suggested that aerodynamic loads are relatively unimportant in determining bending patterns in oscillating wings in air or helium compared to the inertial load when the density ratio between the structure and the fluid is high. On the other hand, they have speculated that if the density ratio is low, for example in water, the fully coupled set of equations from both fluid and solid dynamics may be needed to understand the effects of flexibility on the resulting fluid loads. Following the same scaling arguments, Thiria and Godoy-Diana [68] concluded that when the density ratio is sufficiently high, the wing deformation is dominantly determined by the inertia force, rather than the fluid dynamic forces. Then computing the forces acting on a flexible wing would be a two step process, where first the deformed shapes can be obtained under inertia forces only, then the fluid dynamic forces can be found based on the determined time evolution of the wing shape.

1.2.5 Aerodynamic Performance of Flexible Flapping Wings

Recent review by Shyy *et al.* [6] and experimental study by Ramananarivo, Godoy-Diana, and Thiria [69] give a good overview of the current state of the investigation of the role of the flexibility on the fluid dynamic performance of flapping wings. The maximum propulsive force, such as thrust in forward flight or lift in hover motion, was generated at a frequency which was slightly lower than the natural frequency of the system [45,82,68,69,72,83]. Zhang, Liu, and Lu [45] studied numerically using the lattice Boltzmann method a flexible flat plate modeled as a rigid plate with a torsional spring at the pivot point on the leading edge of the wing. They conclude that the flat plate would move forward, hence generate thrust when the leading edge plunges at a motion frequency that is lower than the natural frequency of the system and backward if the frequency ratio, the ratio between the motion frequency and the natural frequency, is greater than one. Similarly, Masoud and Alexeev [82] used the lattice Boltzmann method to show that at the frequency ratio of 0.95 the maximal propulsive force was obtained. The magnitude of the maximal force would increase when the inertial effects became more important than the fluid inertia. Michelin and Llewellyn Smith [83] used potential flow theory to describe the flow over a plunging flexible wing. The trailing-edge flapping amplitude and the propulsive force are shown to be maximal at resonance conditions. In a series of experiments using self-propelled simplified insect model, Thiria and Godoy-Diana [68] and Ramananarivo, Godoy-Diana, and Thiria [69] also show that the maximum thrust force was around frequency ratio of 0.7. More recently, Gogulapati and Friedmann [72] coupled an approximate aerodynamic model, which was extended to forward flight including the effects of fluid viscosity, to a nonlinear structural dynamic model. For various setups of composite anisotropic Zimmerman wings [71], they investigated the propulsive force generation in forward flight. The maximum propulsive force was also obtained at the frequency ratio slight lower than one. These observations are consistent with the general perception of the resonance phenomena in which even small external force can induce large amplitude deformations and potentially be efficient as well.

However, it was reported for the insect flyers, that the flapping frequency of the insects is below the natural frequencies of the wing, only a fraction of the resonance frequency [84,85]. Sunada, Zeng, and Kawachi [84] measured the natural frequencies of vibration in air and the wing beat frequencies for four different dragonfly wings. The wing beat frequency ratio were in the range of 0.30 – 0.46. Chen, Chen, and Chou [85] have also measured the wing beat frequencies and natural frequencies of the dragonfly wings. In their measurements the average flapping frequency was 27 Hz while the natural frequency, calculated using a spectrum analyzer, was 170 Hz when it is clamped at the wing base, resulting in a frequency ratio of about 0.16. The propulsive efficiency was also investigated numerically [86,82] and experimentally using a self-propelled model [68,69]. Vanella et al. [86] conducted numerical investigations on a two link model and found that the optimal performance as realized when the wing was excited at the frequency ratio of 0.33. For all Reynolds numbers considered in the range of 75 to 1000 the wake capture mechanism was enhanced due to a stronger flow around the wing at stroke reversal, resulting from a stronger vortex at the trailing edge. Thiria and Godoy-Diana [68] and Ramananarivo, Godoy-Diana, and Thiria [69] also show using the experimental setup that is described above that the maximum efficiency is obtained at a frequency ratio lower than that of the maximum propulsion at 0.7. They conclude that the performance optimization is not by looking at the resonance, but adjusting the temporal evolution of the wing shape. On the other hand, Masoud and Alexeev [82] showed that the optimal efficiency for a hovering flat plate at $Re = 100$ was when the motion was excited at the frequency ratio of 1.25. In their setup the flexible flat plate has a geometric angle of attack of 40 deg in contrast to the previously mentioned studies where the plunging motion was symmetric. “Despite the convergence of many observations pointing out this feature, the underlyding mechanisms explaining how the elastic nature of the wing is related to propulsive efficiency remain unclear” [69].

1.3 Objectives

The objective of the this dissertation is three-fold:

(i) Provide framework to systematically analyze the effect of flexibility on oscillating wings;

(ii) Elucidate the interplay between the fluid dynamic forces on the wing and the non-dimensional parameters; and

(iii) Understand the underlying physics of force generation and propulsive efficiency of flapping wings that uses wing flexibility.

First, starting from the Navier-Stokes equations the forces acting on a moving body immersed in a fluid, such as a wing in air or water, will be scaled by properly normalizing the equations. The concepts such as added mass effects, that denotes the force on the wing that is proportional to the wing acceleration and the hydrodynamic impulse will be introduced. For a Reynolds number regime of $O(10^4)$ and low reduced frequency and low Strouhal number flow, the interaction between the wing shape, motion kinematics, and the Reynolds numbers will be probed. The analysis of the fluid dynamic performance of flexible wings is similar to that of flutter in the aeroelasticity community: in flutter research the wing oscillations are results of the interaction between the wing deformations and the aerodynamic loading, here the kinematic motion at the root of the wing is given and we look for the response of the wing structures, the aerodynamics, and the interaction between these two. Our aim is:

(i) to quantify the interplay of the imposed kinematics and the response of the flexible wing structure and

(ii) to identify the dominant parameter in the resulting fluid dynamics, with sufficient fidelity so that main physical mechanisms can be elucidated.

Three canonical cases with sinusoidal kinematics will be considered to assess the role of the chordwise flexible, spanwise flexible, and isotropic wings on the resulting fluid dynamic forces. Based on these canonical cases, we will identify the underlying physical mechanism and propose a scaling parameter for the force generation and the propulsive efficiency of flexible oscillating wings that depends on known non-dimensional parameters. Identifying this scaling parameter leads to an order of magnitude estimation of the flexilibity enhanced fluid dynamic performance. Furthermore, we will extrapolate the scaling parameter to the insects by assuming that the weight of the insects are sustained by the lift and show that the generated lift also follows the same scaling.

1.4 Outline

The outline of this dissertation is as follows.

In Chapter 2, first, a dimensional analysis will be performed in Section 2.2, followed by the non-dimensionalization of the governing equations. The numerical framework for flexible flapping wings is introduced in the subsequent sections: The fluid dynamics solver (Section 2.1), applied turbulence model (Section 2.4), remeshing algorithm (Section 2.5), structural dynamics solver (Section 2.6), and the fluid-structure interaction interface (Section 2.7) are described.

Then in Chapter 3, the scaling of the forces will be discussed based on a control volume analysis (Section 3.1). Furthermore, for high Reynolds numbers the effects of the curvature of the airfoil shape, the kinematics of the motion, and the Reynolds number on the flow structure and the forces are assessed in Chapter 4.

In Chapter 5 the scaling relationships for the force generation and the propulsive efficiency for flexible flapping wings will be established for high Reynolds number and high reduced frequency systems. Based on the numerical computations of i) the thrust generation of a plunging chordwise flexible airfoil in Secion 5.2.1, ii) spanwise flexible wing in Section 5.2.2 in forward flight in water for different wing stiffnesses and motion frequencies, the physics of fluid-structure interaction between the plunging wing and the fluid flow will be explored. Furthermore, the lift generation of a flapping isotropic Zimmerman wing in hover in air (Section 5.2.3) will be shown to follow a similar mechanism. For this case a surrogate model will be constructed based on the variations of Young's modulus and wing density. Furthermore, based the identified mechanism, a scaling parameter for the force generation due to the flexibility of the wing will be proposed using a dynamic beam analysis in Section 5.2.4, with an extrapolation of the scaling to insects. Finally, a scaling parameter will be obtained for the propulsive efficiency in Section 5.3 with a discussion on the applicability of the scaling on the MAV design and interpretation of the observed physics.

Chapter 2.Governing Equations and Numerical Methods

2.1 Introduction

To understand flapping wing phenomena where the wings can undergo large deformations, numerous computational techniques have been applied. Two main categories are based moving meshes [87,88] or stationary meshes with cut cell or immersed boundary methods [87,89] have been developed. The physical models include NS as well as approximate treatments [90,91,72].

Different levels of fidelity and diverse numerical algorithms, depending on the objective of the study and accuracy and cost of the computations, can be incorporated into a numerical framework of flexible flapping wing simulations. High-fidelity framework can be used to conquer the rich and complex physics behind flexible flapping wing aerodynamics, while a low-fidelity model can be used for quick yet reliable design optimization of a complex and multi-dimensional design space. The aeroelastic coupling can be based on a time-domain partitioned process where the interaction between the fluid and the solid fields occurs at a shared boundary iteratively at a given time step. An advantage is that for the solutions of both fields, which are described by different nonlinear partial differential equations, well-established solvers can be used. Tang et al [92], Chimakurti *et al.* [77], and Aono et al. [93] have coupled an in-house finite-volume based Navier-Stokes solver to a beam model [92], a commercial nonlinear finite-element solver, MSC.Marc, a geometrically nonlinear active beam solver [77], and a co-rotational shell finite element model [94]. Furthermore, Gordnier *et al.* [95] coupled an in-house high-order Navier-Stokes solver to a geometrically nonlinear active beam solver, McClung *et al.* [96] developed the OVERFLOW Navier-Stokes solver to a modal representation of two-dimensional beam, and Stanford *et al.* [97] combined a two-dimensional quasi-steady blade element model to a nonlinear co-rotational beam model.

Gogulapati and Friedmann [72] coupled an approximate aerodynamic model, which is capable of predicting vorticity field and forces acting on the wing in hover and forward motions including the effects of fluid viscosity, to a nonlinear structural dynamic model that can model anisotropic composite wings.

Some of the numerical challenges associated with aeroelastic coupling of highly deformable three-dimensional flapping wings are that large number of cells are required to resolve the necessary flow field phenomena such as vorticity generation near the wing as well as convection and diffusion of large scale vortical structures away from the wing and that large flapping amplitudes and deformations lead to large mesh deformations that require numerically robust and efficient remeshing algorithms. To obtain the three-dimensional flow solutions with the number of cells in the orders of $O(10^6)$ a Navier-Stokes equations solver is often parallelized, which introduces obvious implementation challenges for the problems involving moving meshes: how to efficiently communicate information between multiple processors about the displacements stored in other processors to remesh the grid; and how to provide interface for the communication for the fluid-structure interaction involving two distinct solvers, where one or both solvers are parallelized. Two strategies have been studied for unstructured grids. In the first category the computational mesh is considered as an elastic solid, where the new nodal displacements are obtained by solving the structural dynamics equations. For example, Stein *et al.* [98] proposed to solve the linear elastostatics equations with a stiffening factor to reduce the volumetric distortion to maintain the mesh quality in finite element formulation. Smith and Wright [99] recast the linear elastostatics equations in finite-volume discretization, which involves similar terms as the Navier-Stokes equations, so that the remeshing algorithm could be implemented based on the readily available momentum equation solver as a template. In the second category the nodal displacements are interpolated using Radial Basis Functions (RBF) based on the displacements given at the boundary conditions, either prescribed or from the structural dynamics solver. This method, as the cell connectivity information is not required, can be applied to structured and unstructured meshes and is seen to keep initial mesh qualities well and efficiently [100,101,102,103].

Chimakurthi *et al*. [77] have presented a computational framework capable of computing flexible flapping wing aerodynamics and aeroelasticity. They have detailed fluid and structural solvers as well as the coupling strategies. Aono *et al*. [93] have further developed the techniques and investigated the dynamic characteristics associated with spanwise flexibility of a plunging wing. In this Chapter, the advanced computational capabilities presented in Ref [77] is revisited. Furthermore, new remeshing techniques, similar to that reported by De Boer *et al*. [100] and Rendall and Allen [101,102,103], have been developed and tested. The added capabilities can handle a variety of wing structures with large flapping translation and rotation that is able to efficiently deform large number of nodes under large wing movements, while keeping the initial mesh qualities. The relevance of this framework is three-fold. The computed fluid flow field and the structural response can be studied to understand the nonlinear coupled field problem for flapping wing flyers, also these results can function as a validation for lower order tools or experimental results. Moreover, this framework can serve as a tool to construct a quick and reliable design guideline for MAV applications.

2.2 Dimensional Analysis and Non-Dimensional Governing Equations

As discussed in Section 1.2.3, it is useful by the means of dimensional analysis to i) identify characteristic properties of the system under consideration, ii) to reduce the number of parameters, and iii) to indicate which combination of parameters becomes important under a given condition. From the view point of fluid-structure interaction, several dimensionless parameters arise during the non-dimensionalization process of the fluid and structural dynamics equations using a set of suitable reference scales. Depending upon the problem at hand and the type of equations used to model the physical phenomena involved, the resultant set of scaling parameters could vary.

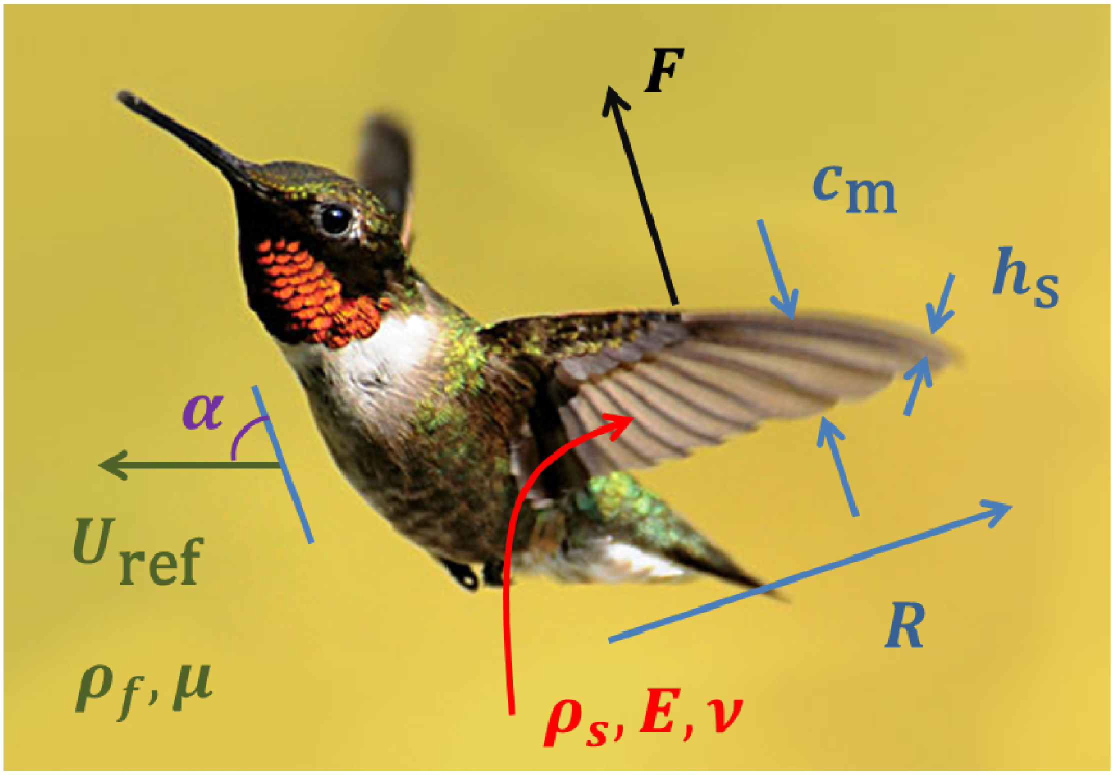

Figure 2-1 Relevant physical variables shown for a case of hummingbird. The picture is reproduced, by permission, from Wei Shyy © [104].

The relevant physical quantities related to the system of flexible flapping wing fluid dynamics are the density, and the viscosity, , of the fluid; the reference velocity, , of the fluid flow field; the half span, , the mean chord, , and the thickness, , of the wing geometry; the density, and the Young's modulus, , and the Poisson's ratio, , of the wing structure; the flapping (plunging) amplitude, ( ), the flapping frequency, , and the geometric angle of attack, ; and finally the resulting aerodynamic force, . There are 13 variables and three fundamental dimensions, i.e. mass, time, and length, leading to 10 non-dimensional parameters. With , , and as the basis variables to independently span the three fundamental dimensions, the dimensional analysis leads to the non-dimensional parameters shown in Table 2-1 and Figure 2-1. The resulting set of non-dimensional parameters consists of most of the well-known parameters in the flapping wing aerodynamics community, however it is not unique.

Table 2-1 Non-dimensional parameters for the flexible flapping wing systems

Non-dimensional parameter	Symbol	Definition	Note
Reynolds number	Re	$\rho_f U_{\mathrm{ref}} c_m / \mu$	
Aspect ratio	AR	R/c_m	
Thickness ratio	h_s^*	h_s/c_m	
Density ratio	ρ^*	ρ_s/ρ_f	
Poisson's ratio	ν	ν	
Effective stiffness	Π_1	$Eh_s^{*3}/\{12(1-\nu^2)\rho_f U_{\mathrm{ref}}^2\}$	plate
		$Eh_s^{*3}/\{12\,\rho_f U_{\mathrm{ref}}^2\}$	beam
Reduced frequency	k	$\omega c_m/(2U_{\mathrm{ref}})$	
Strouhal number	St	$\phi_a\, AR\, k/\pi$	flapping
		$h_a\, k/(c_m \pi)$	plunging
Effective angle of attack	α_e	$\alpha + \mathrm{atan}(2\pi\, St)$	plunging
Force coefficient	C_F	$F/\left(\frac{1}{2}\rho_f U_{\mathrm{ref}}^2 c_m^2 AR\right)$	

The governing equations are non-dimensionalized with the reference velocity, U_{ref}, as the velocity scale, inverse of the motion frequency, $2\pi/\omega$ as the time scale, and the mean chord, c_{m}, as the length scale. For forward flight cases the forward velocity of the wing, i.e. the incoming velocity in the frame of reference of the wing, is chosen as U_{ref} and for hovering the mean tip velocity during half stroke is taken as the reference velocity. The resulting governing equations for the incompressible fluid modeled by the unsteady three-dimensional Navier-Stokes equations with constant density and viscosity are

$$
\begin{gathered}
\frac{\partial}{\partial x_i^*}(u_i^*) = 0 \\
\frac{k}{\pi}\frac{\partial}{\partial t}(u_i^*) + \frac{\partial}{\partial x_i^*}\left(u_j^*\, u_i^*\right) = -\frac{\partial p^*}{\partial x_i^*} + \frac{1}{Re}\frac{\partial}{\partial x_j^*}\left\{\frac{\partial u_i^*}{\partial x_j^*}\right\}
\end{gathered}
\tag{1}
$$

where $(\cdot)^*$ indicates non-dimensional variables. The reduced frequency k is a measure of unsteadiness by comparing the spatial wavelength of the flow disturbance to the chord [105]. For hover, the reference velocity is based on the mean wing tip velocity, thus reduced frequency is inversely proportional to the flapping (plunging) amplitude and aspect ratio of the wing and is not related to the flapping frequency. On the other hand, the reduced frequency based on the forward speed is proportional to flapping frequency and the mean chord length, and inversely proportional to the flight speed. Another interpretation of the reduced frequency is that it gives the ratio between the fluid convection time scale, $c_{\mathrm{m}}/U_{\mathrm{ref}}$, and the motion time scale, $2\pi/\omega$. The Reynolds number Re is the ratio between the inertial and the viscous forces in the fluids. In hover the Reynolds number is proportional to the flapping (plunging) amplitude, the flapping frequency, square of the mean chord length, and the aspect ratio of the wing.

The flexible wing structure is modeled locally by

$$\rho^* h_s^* \left(\frac{k}{\pi}\right)^2 \left(\frac{L}{c_m}\right) \frac{\partial^2 w^*}{\partial t^{*2}} + \Pi_1 \left(\frac{c_m}{L}\right)^3 \Delta^{*2} w^* = f_f^*, \tag{2}$$

where w is the displacement due to bending motion, $\Delta^* = \partial^{*2}/\partial x_i^{*2}$ the Laplacian operator, and f_f^* the distributed transverse fluid force on the wing per unit span. A special care is given in the direction of the wing bending, because the correct length-scale for the spanwise bending is the half span R and not the chord c_m. The correction factor that arises is expressed as (L/c_m), where $L/c_m = 1$ for the chordwise flexible airfoil case (Section 5.2.1), and $L/c_m = AR$ for the spanwise flexible wing (Section 5.2.2) and isotropic Zimmerman (Section 5.2.3) wings, where AR is the aspect ratio of the wing: For the three-dimensional wings the bending motion is aligned with R, so that a factor of AR is required to renormalize the transverse displacement. The density ratio ρ^* is the ratio between the wing density and the fluid density and the effective stiffness Π_1 gives the ratio between the elastic bending forces and the fluid dynamic forces. The coefficient of the inertial term will be used frequently later in the discussion of the fluid dynamic performance of flexible wings in Chapter 5 and is abbreviated as the effective inertia $\Pi_0 = \rho^* h_s^* (k/\pi)^2$. In this dissertation the prescribed motion at the root of the wing is sinusoidal of the form

$$\phi(t^*) = \frac{St}{AR}\frac{\pi}{k}\sin(2\pi t^*), \tag{3}$$

for the flapping motion and

$$h(t^*) = St\frac{\pi}{k}\sin(2\pi t^*), \tag{4}$$

for the plunging motion, where the sine function can be replaced by the cosine function. The Strouhal number St appears in combination with k to give the plunge amplitude h_a/c_m. The Strouhal number indicates the ratio between the flapping speed and the reference velocity. It characterizes the vortex dynamics of the wake and shedding behavior of vortices of a flapping wing in forward flight [3,106]. Still unclear is the meaning and the role of the Strouhal number in hover, since for hover the Strouhal number will reduce to a constant. The pitching motion is given as

$$\alpha(t^*) = \alpha_0 + \alpha_a \sin(2\pi t^* + \phi), \tag{5}$$

Finally, the force coefficient is then given by a to-be-determined relation

$$C_F = \widetilde{\Psi}\,(Re, AR, h_s^*, \rho^*, \nu, \Pi_1, k, St, \alpha). \tag{6}$$

In this dissertation the aim is to simplify Eq. (6) by reducing the number of non-dimensional parameters involved. The time-averaged force $\langle C_F \rangle$ of C_F are calculated as

$$\langle C_F \rangle = \frac{\omega}{2\pi}\int_{2\pi m/\omega}^{2\pi(m+1)/\omega} C_F\,dt. \tag{7}$$

where $m = 2$ unless otherwise specified. The reason for setting $m > 1$ is to avoid initial transient effects.

2.3 Fluid Dynamics Solver

The governing equations for the fluids given by Eq. (1) are solved with Loci-STREAM [107,108,109], which is a three-dimensional, unstructured, pressure-based finite volume solver written in the LOCI-framework. It employs implicit first or second order time stepping and treats the convection terms using the second order upwind-type scheme and the pressure and viscous terms using second order schemes. The system of equations resulting from the linearized momentum equations are handled with the symmetric Gauss-Seidel solver. The pressure correction equation is solved with either the GMRES linear solver with Jacobi preconditioner provided by PETSc [110,111,112], or the BoomerAMG [113] linear solver provided by hypre. The LOCI-framework is by design rule-based highly parallelizable framework for finite volume methods [114]. The geometric conservation law [115], a necessary consideration in domains with moving boundaries, is satisfied [116]. The mesh deformations are realized using radial basis function (RBF) interpolations [100].

2.4 Turbulence Closure for Flows at $\boldsymbol{Re} = \boldsymbol{O}(\mathbf{10^3 - 10^4})$

For the flow fields at $Re = O(10^3 - 10^4)$ the Reynolds-Averaged Navier-Stokes (RANS) equations are solved by coupling the turbulence closure with Menter's Shear Stress Transport (SST) model [117], and the continuity equation for incompressible flow, written below in dimensional variables

$$\frac{\partial}{\partial x_i}(\bar{u}_i) = 0$$

$$\frac{\partial}{\partial t}(\bar{u}_i) + \frac{\partial}{\partial x_j}(\bar{u}_j\bar{u}_i) = -\frac{1}{\rho_f}\frac{\partial p}{\partial x_i} + \frac{1}{\rho_f}\frac{\partial}{\partial x_j}\left\{(\mu + \mu_t)\frac{\partial \bar{u}_i}{\partial x_j}\right\}$$

$$\frac{\mu_t}{\rho_f} = \frac{a_1 k_t}{\max(a_1\omega_t, \mathrm{S}\,F_2)}$$

$$\tau_{ij} = -\rho_f\overline{u_i'u_j'} = \mu_t\left(\frac{\partial \bar{u}_i}{\partial x_j} + \frac{\partial \bar{u}_j}{\partial x_i}\right) - \frac{2}{3}\rho_f\, k_t\, \delta_{ij}$$

$$\frac{\partial k_t}{\partial t} + \frac{\partial}{\partial x_j}(\bar{u}_j k_t) = \hat{P}_k - \beta^*\omega_t k_t + \frac{1}{\rho_f}\frac{\partial}{\partial x_j}\left\{(\mu + \sigma_k\mu_t)\frac{\partial k_t}{\partial x_j}\right\}$$

$$\begin{aligned}\frac{\partial \omega_t}{\partial t} &+ \frac{\partial}{\partial x_j}\left(\bar{u}_j \omega_t\right) \\ &= -\frac{\gamma}{\mu_t}\tau_{ij}\frac{\partial u_i}{\partial x_j} - \beta {\omega_t}^2 + \frac{1}{\rho_f}\frac{\partial}{\partial x_j}\left\{(\mu + \sigma_\omega \mu_t)\frac{\partial \omega_t}{\partial x_j}\right\} \\ &+ 2(1-F_1)\sigma_{\omega 2}\frac{1}{\omega_t}\frac{\partial k}{\partial x_i}\frac{\partial \omega_t}{\partial x_i}\end{aligned} \tag{8}$$

where a_1, β, β^*, γ, σ_k, σ_ω, $\sigma_{\omega 2}$, F_1, F_2 are defined as in Menter's SST formulation [117], μ_t is the eddy viscosity, $S = \sqrt{2S_{ij}S_{ij}}$ is the invariant measure of the strain rate. The Reynolds averaged values are indicated by an over-bar and the fluctuations with a prime. Compared to Menter's original SST turbulence model [118] a limiter has been built in to the production term, $\hat{P}_k$, in the turbulence kinetic energy equation, as

$$\begin{gathered} P_k = \mu_t \frac{\partial \bar{u}_i}{\partial x_j}\left(\frac{\partial \bar{u}_i}{\partial x_j} + \frac{\partial \bar{u}_j}{\partial x_i}\right), \\ \hat{P}_k = \min(P_k, 10\ \cdot \beta^* \rho k_t \omega_t), \end{gathered} \tag{9}$$

where P_k is the production term in the original SST formulation, to prevent the build-up of turbulence in stagnation regions. Another change is the use of invariant measure of the strain-rate tensor in the formulation for the eddy viscosity instead of the vorticity magnitude, $\Omega = \sqrt{2\Omega_{ij}\Omega_{ij}}$. The strain-rate invariant is considered to be a better measure for the fluid deformation, since the Boussinesq approximation is also based on the strain-rate. The two differences between the original and the modified SST formulation are summarized in Table 2-2.

Table 2-2 Original [118] and modified [117] SST turbulence model

	Original SST	Modified SST
TKE Production term	$P_k = \mu_t \frac{\partial \bar{u}_i}{\partial x_j}\left(\frac{\partial \bar{u}_i}{\partial x_j} + \frac{\partial \bar{u}_j}{\partial x_i}\right)$	$\hat{P}_k = \min(P_k, 10\ \cdot \beta^* \rho k \omega)$
Eddy viscosity	$\nu_t = \frac{a_1 k}{\max(a_1 \omega, \Omega\, F_2)}$	$\nu_t = \frac{a_1 k}{\max(a_1 \omega, S\, F_2)}$

The effects of a limiter on the production term in the turbulence kinetic energy equation for pitching and plunging airfoils have been discussed by Kang, *et al*. [119] and later in Section 4.4. The differences between results the original and the modified SST turbulence model are small for a flat plate in freestream at $Re = 6\times10^4$. Although the accumulation of eddy viscosity is reduced by limiting the production of turbulence kinetic energy at the leading edge compared to the computation using the original version of SST turbulence closure, in the critical regions above the plate, the two models produce comparable eddy viscosity distributions due to the leading edge effect. Consequently, the resulting flow structures from the two models are similar as well. In this study all numerical results have been obtained using the original version of SST turbulence model unless otherwise noted.

2.5 Remeshing

2.5.1 Radial Basis Function Interpolation Remeshing

De Boer *et al*. [100] and Rendall and Allen [101,102,103] have shown the effectiveness of using RBF interpolation method to remesh the unstructured grids. There are two distinctive advantages: i) Connectivity information is unnecessary for the RBF interpolation method, that means any arbitrary order of nodal information will result in the same mesh. However, ordering the nodes based on the distances between the nodes will make the linear system more diagonally dominant for the compact RBFs [100], which will reduce the computational time. ii) The resulting mesh keeps the original mesh quality, especially the orthogonality near the moving boundary surface [100,101], which is important in viscous fluid computation where the cells are usually stretched and clustered to capture small length scale flow phenomena.

Given the boundary displacement vector $\Delta w_{\mathrm{b}_{ij}}$ at the node j, with the position $w_{\mathrm{b}_{ij}}$ either on the fluid dynamic surface mesh of a flexible body, or any other prescribed boundary surface, for instance zero displacements at the tunnel wall, the displacement vector, Δw_{ik}, of a node k, with the position w_{ik}, of the fluid dynamic volume mesh with respect to the initial grid, is given as with summation of repeated indices as

$$\Delta w_{ik} = \alpha_{ij}\sigma_{kj}^{\mathrm{ab}} + \beta_{ik}, \tag{10}$$

where index i represents the three components in three-dimensional space, $\sigma_{ij}^{\mathrm{ab}}$ is the coupling matrix from the fluid dynamic surface nodes to the aerodynamic volume nodes given as

$$\sigma_{kj}^{\mathrm{ab}} = \sigma\left(\left\| w_{\mathrm{a}_{lk}} - w_{\mathrm{b}_{lj}} \right\|_l\right), \tag{11}$$

with $\|\cdot\|$ being the Euclidean distance measure acting on the index $l = 1,2,3$, σ is a radial basis function, and β_{ik} is a polynomial. If the radial function is conditionally positive definite, and β_{ik} is a linear polynomial, then a unique remeshing will result [100,120]. In this dissertation a linear polynomial will be used:

$$\beta_{ik} = \beta_{ik}^{0} + \beta_{i}^{j}\, w_{\mathrm{a}_{jk}}, \tag{12}$$

For remeshing the compact C^2 RBF constructed by Wendland [120] will be used motivated by the previous results [100,101,120] that showed it to be computationally efficient while being able to retain the mesh qualities, given as

$$\sigma(x) = \left(1 - \frac{x}{r}\right)^4 \left(\frac{4x}{r} + 1\right), \tag{13}$$

where r is the support radius of this compact function. As the support radius increases a node acquires more information about the displacements of neighboring nodes, leading to better approximation. On the other hand if the support radius is small the resulting linear system will be sparse, hence the computational cost would decrease. However if r is too small, negative jacobian or volume of a cell might occur. All RBFs, compact and global, listed in Ref. [100] are available in the current framework for interpolation purposes.

The unknowns in Eq. (10) are the weight coefficients, α_{ij} ($i = 1,2,3,\ j = 1, \dots, N_{\mathrm{b}}$), and the polynomial coefficients, β_i^j, that can be solved by the requirements that the prescribed nodal displacements must be recovered by the RBF interpolation at these nodes, i.e.,

$$\Delta w_{\mathrm{b}_{ik}} = \alpha_{ij}\sigma\left(\left\| w_{\mathrm{b}_{lk}} - w_{\mathrm{b}_{lj}} \right\|_l\right) + \beta_{ik}^0 + \beta_i^j\, w_{\mathrm{b}_{jk}}, \tag{14}$$

and the additional requirement for unique solution [120],

$$\alpha_{ij} 1_j = 0_i, \qquad \alpha_{ij} x_{\mathrm{b}_{jk}} = 0_{ik}, \tag{15}$$

where 1_j is a summation vector that sums all elements along j, 0_i the zero vector over the index i, and 0_{ik} the zero matrix over the index ik. In vector notation the resulting linear system is shown below and is exactly the same as found in Refs [100,120]:

$$\begin{bmatrix} \mathbf{M}_{\mathrm{b,b}} & \mathbf{Q}_{\mathrm{b}} \\ \mathbf{Q}_{\mathrm{b}}^T & \mathbf{0} \end{bmatrix} \begin{bmatrix} \boldsymbol{\alpha} \\ \boldsymbol{\beta} \end{bmatrix} = \begin{bmatrix} \Delta \boldsymbol{w}_{\mathrm{b}} \\ \mathbf{0} \end{bmatrix}, \tag{16}$$

with for each i index

- $\sigma\left(\left\| w_{\mathrm{b}_{lk}} - w_{\mathrm{b}_{lj}} \right\|_l\right) \rightarrow \mathbf{M}_{\mathrm{b,b}}$,
- $\left[1_j \;\; w_{\mathrm{b}_{jk}}\right] \rightarrow \mathbf{Q}_{\mathrm{b}}$,
- $\alpha_{ij} \rightarrow \boldsymbol{\alpha}_i$, $\beta_i^j \rightarrow \boldsymbol{\beta}_i$, $\Delta w_{\mathrm{b}_{ik}} \rightarrow \Delta \boldsymbol{w}_{\mathrm{b}_i}$.

This linear system is solved using PETSc's GMRES iterative solver with Jacobian preconditioner using multiple processors.

To capture the three-dimensional flow phenomena the number of cells is typically in the order of millions. To enhance the computational speed the fluid-solver is parallelized using Message Passing Interface (MPI) where the computational domain is decomposed optimally for the computation of velocity and pressure fields. This implies that the boundary nodes on the moving surfaces are randomly distributed among the processors. To implement the RBF interpolation remeshing method efficiently in parallel the following steps are taken by noting that the nodal coordinates on the boundary surfaces, $w_{b_{ij}}$, stay stationary in time:

(i) Preprocessing step:

a. $w_{b_{ij}} \rightarrow \mathbf{Q}_{\mathrm{b}}$: identify the local nodes on the boundary surfaces. Using ALLGATHER operation assemble and distribute the coordinates of all nodes on the boundary surfaces into a matrix $\mathbf{Q}_{\mathrm{b}}$.

b. $\left(w_{b_{ij}}, \mathbf{Q}_{\mathrm{b}}\right) \rightarrow \sigma\left(\left\|w_{\mathrm{b}_{lk}} - w_{\mathrm{b}_{lj}}\right\|_{l}\right) = \mathbf{M}_{\mathrm{b,b}}$: iterate over the local nodes on the boundary surface and by computing the distances to all elements in $\mathbf{Q}_{\mathrm{b}}$ construct the local partition of the system matrix having a sparse matrix structure provided by PETSc.

(ii) Remeshing:

a. $\Delta\boldsymbol{w}_{\mathrm{b}} \rightarrow (\boldsymbol{\alpha}_i, \boldsymbol{\beta}_i)$: solve the linear system to obtain the weight and the polynomial coefficients locally. Using the ALLGATHER operation, distribute the coefficients globally.

b. $\left(\boldsymbol{\alpha}_i, \boldsymbol{\beta}_i, \mathbf{Q}_{\mathrm{b}}, w_{b_{ij}}\right) \rightarrow \Delta w_{ik}$: Compute the nodal displacements for all volume nodes by applying Eq. (10).

Since the assembly of the system matrix is performed before the time integration begins, and the parallel communication during the computation is only needed for the linear solver and for the ALLGATHER operation of the coefficients, $\boldsymbol{\alpha}_i$ and $\boldsymbol{\beta}_i$, this method is suitable for parallelization. Further improvements can be obtained by using the Schur-complement techniques which involve the inversion of $\mathbf{M}_{\mathrm{b,b}}$ has the potential to accelerate the remeshing process since $\mathbf{M}_{\mathrm{b,b}}$ is a positive-definite symmetric matrix so that well-known iterative solvers can be used such as PCG, and during the time integration only matrix multiplications are needed to obtain the new displacements for the volume nodes [102].

2.5.2 Assessment of Remeshing Performance

To assess the performance in terms of the mesh qualities, and domain scalability of the RBF interpolation remeshing method, two test cases previously reported by Stein *et al*. [98] and Smith and Wright [99] are computed. The initial mesh consists of a computational domain in a square shape with length of two and a two percent thick flat plate of chord length one in the center of the domain, see Figure 2-2. This test case is in particular relevant for flapping wing simulations because this case reflects the large displacement wing motions including translations and rotations. Furthermore, to be able to compare to experiments done in water or wind tunnels the remeshing capabilities need to be robust under large deformations with non-moving outer computational domain. The latter is more challenging as the computational domain is smaller. In all solutions shown in this Section the new mesh is obtained after one time step. For the RBF the Wendland's C^2 polynomial Eq. (13) is used with a support radius of 2.0. The linear solver converged to the imposed absolute tolerance level of 1.0×10^{-30}. In the first case the flat plate is rotated 60 deg around its mid-chord point of the plate. The order of this angle corresponds to typical flapping angle amplitudes [3]. In the second case the flat plate translates half chord length upwards. Note that the mesh is three-dimensional with unit span length with one cell in spanwise direction to simulate two-dimensional fluid flow in a three-dimensional fluid solver. This doubles the number of grid nodes from the two-dimensional situation.

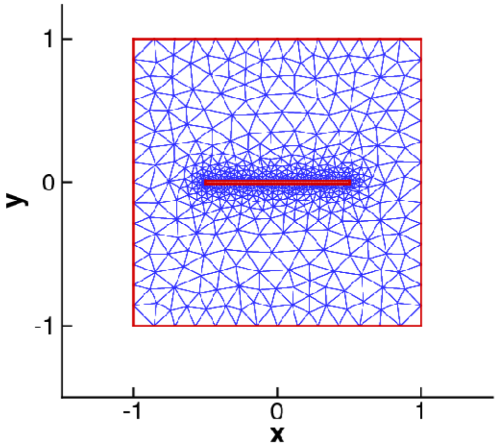

Figure 2-2 Initial mesh of a two percent thick flat plate in a square domain. Total number of cells, nodes, and boundary nodes are 1224, 1384, and 520, respectively.

Two grid measures are computed to assess the mesh qualities: non-smoothness, which measures the cell volume change in space, defined as

$$\text{non-smoothness} = -\ \text{—}\qquad\text{—} \tag{17}$$

where is the cell volume, is the cell area. To measure the skewness of a cell the following quantities are determined

$$\text{skewness} = \tag{18}$$

For both mesh quality metrics high values would result in worse accuracy of the fluid flow solutions and small values are desired. The domain scalability of the current remeshing method with respect to the mesh size is measured by refining the initial mesh by multiplying the number of nodes on the boundary faces by = 2, 4, 8, and 16, see Table 2-3.

Table 2-3 Number of cells, number of nodes, and number of boundary nodes depending on the multiplication factor N_g.

N_g	Number of cells	Number of nodes (N_v)	Number of boundary nodes (N_b)
1	1224	1384	520
2	3272	3592	1040
4	10142	10782	2080
8	35896	34616	4160
16	127496	130056	8320

As the RBF interpolation remeshing method acts on the distances, the cells near the flat plate being more influenced by the motion of the flat plate than the cells away, the cells around the flat plate move almost rigidly, see Figure 2-3. Figure 2-4 shows the non-smoothness and the skewness of the cells on the initial mesh and the resulting mesh under the rotation and translation for the baseline case (N_g=1) and the maximally refined case (N_g=16). The focus is given to how well the initial mesh qualities are preserved under remeshing process. In small region between the edge of the flat plate and the outer boundary of the computational domain both non-smoothness and skewness suffer due to the shearing effect between the moving flat plate and the non-moving outer boundary. However, overall, both the non-smoothness and the skewness near the flat plate are well preserved. On the refined mesh the cells are so small that the smoothness remains intact, which was also observed for N_g = 2, 4, and 8. Regarding the skewness, again due to the shearing behavior, the skewness increases between the flat plate and the boundaries of the computational domain, still the mesh qualities remain well near the flat plate, which is important to capture smaller near-wall flow phenomena accurately.

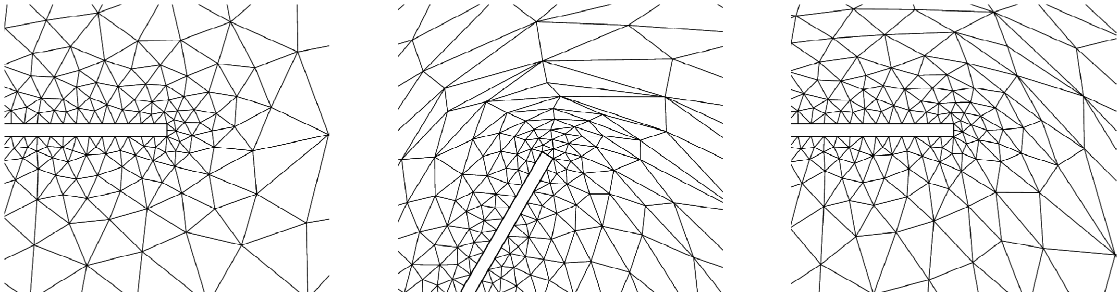

(a) initial distribution (b) after rotation (c) after translation

Figure 2-3 Mesh distribution near the trailing-edge of the flat plate on (a) the initial grid, (b) after rotation, and (c) after translation for the baseline grid (=1).

The domain scalabilities are shown in Figure 2-5, which is defined as

$$\frac{\qquad}{\qquad} \qquad (19)$$

On a single processor the domain scalability is assessed for the rotation and translation cases. The complexity of the linear solver scales with and the RBF evaluation process of Eq. (10) with where . If the number of boundary nodes is doubled, i.e. =2, then the domain scalability would be , which is confirmed in Figure 2-5.

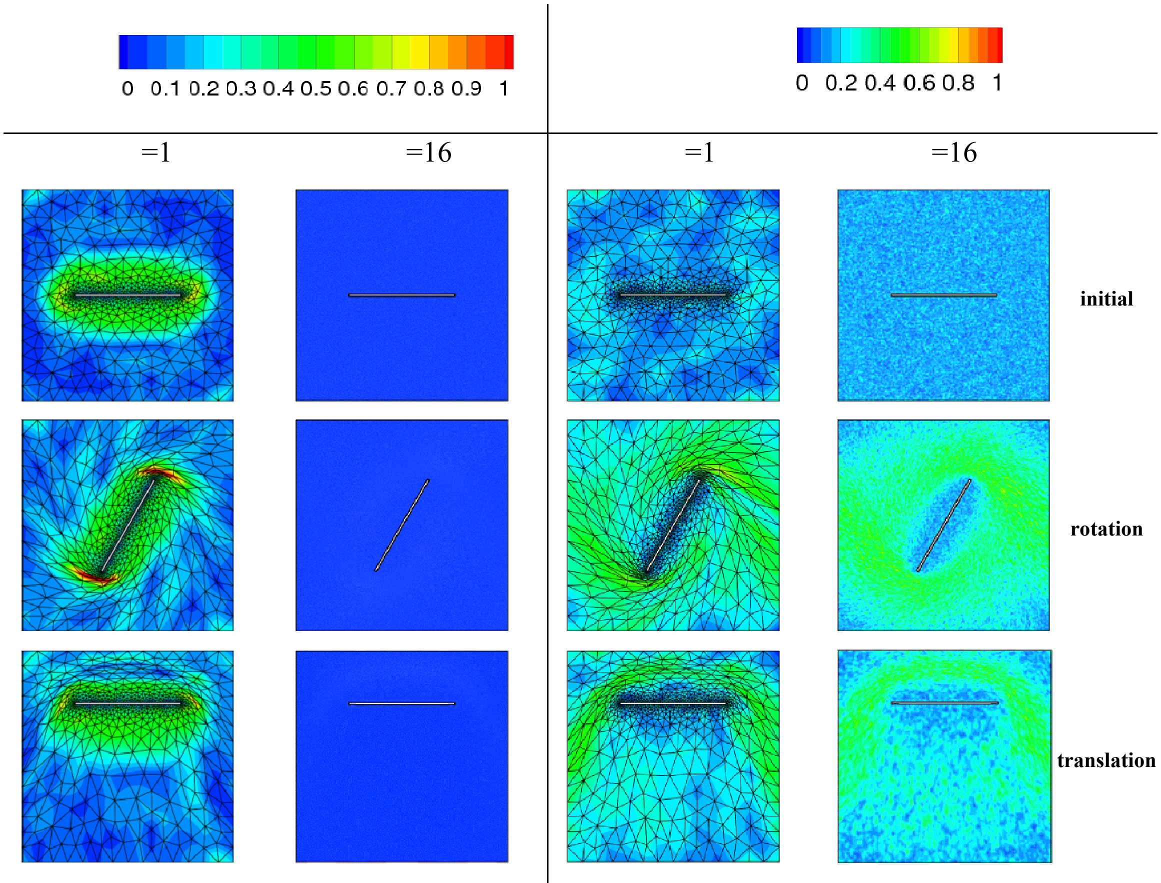

(a) non-smoothness (b) skewness

Figure 2-4 Non-smoothness and skewness of the cells on the initial mesh and the rotated mesh for the mesh scalability factors = 1 and 16 of a flat plate in a non-moving square shaped outer boundary under the rotational and translational motions. Note that on the = 16 grid the mesh distribution is not shown for visibility purposes.

The influence of the support radius, , on the resulting computational time and mesh qualities are assessed by varying the radius from 2 to 1 and 3 on the = 8 grid using single processor for the translational motion. For the compact radial basis functions, such as Wendland's function, Eq. (13), used here, the support radius sets the radius influence by setting the radial basis function value to zero if the distance between two points becomes larger than the radius. Table 2-4 shows the computational time taken for different support radius. By reducing the support radius from = 2 to = 1 the computational cost reduces because the coupling matrix in Eq. (16) is sparser. On the other hand, increasing to 3 introduces more coupling between the boundary nodes and results in 23% increase in computational time. However, for smaller , the influence of the moving nodes is propagated only for smaller distances and the resulting mesh distortions remain close to the flat plate. This behavior is shown in Figure 2-6 where the skewness is shown for = 1, 2, and 3. For = 1 the deformation occurs close to the flat plate and the cells are more clustered, while for = 3 the skewness is smoothened out over larger area.

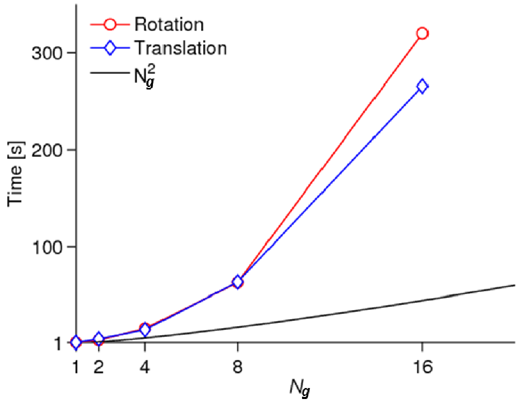

Figure 2-5 Domain scalabilities of a flat plate in a non-moving square domain under rotation and translation.

Finally, as a test case, a three-dimensional mesh around the Zimmerman wing planform, which will be used later in Section 5.2.3 to study the effects of isotropic elasticity on a flapping motion in hover, is deformed using the RBF interpolation method described in this section. In the original mesh the Zimmerman wing is placed horizontally in the center of the computational mesh. The symmetry plane is constrained in space in all directions, representing for example a wing-body configuration. A 45 deg flapping motion is imposed at once during one computational time step to simulate a large deformation motion, which is not unusual for insect flyers. The resulting skewness distribution illustrated in Figure 2-7 shows that the orthogonality of the cells near the wing is well preserved.

Table 2-4 The computational time in components for the translating flat plate in a square domain on the = 8 mesh using single processor.

	Linear solve (s)	Applying Eq. (10) [s]	Total time [s]
1	0.30	6.1	6.4
2	0.76	12	13
3	1.8	14	16

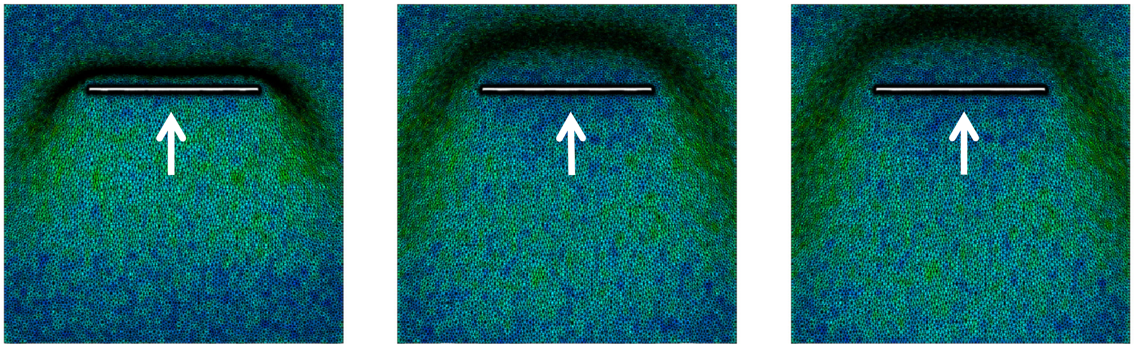

(a) = 1 (b) = 2 (c) = 3

Figure 2-6 Skewness of the cells on the = 8 grid of a flat plate in a non-moving square shaped outer boundary under the translational motion. Black lines represent the mesh distribution. White arrows indicate the translation motion.

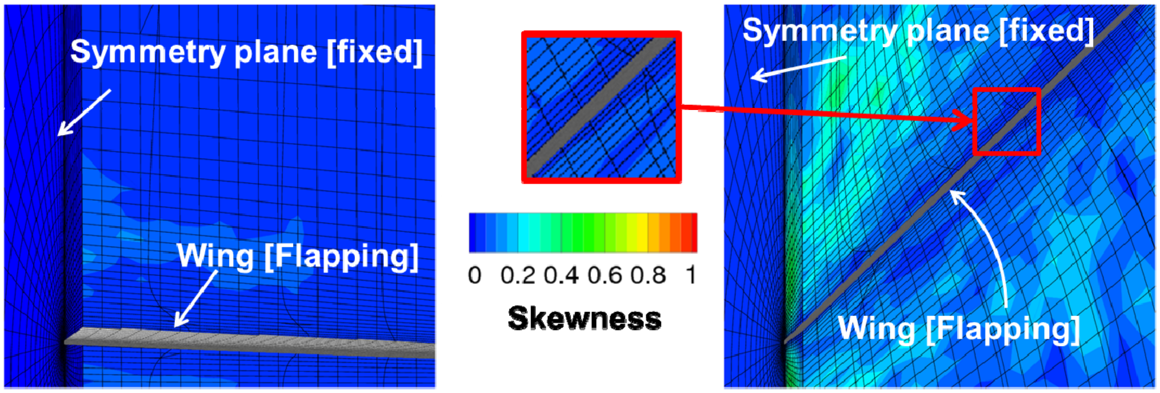

Original configuration **After 45 deg flap**

Figure 2-7 Skewness contours around a Zimmerman wing mesh after 45 deg flapping motion at once.

2.6 Structural Dynamics Solver

Two structural dynamics solvers with different fidelity have been incorporated. For linear analysis of a beamlike flat plate, the Euler-Bernoulli beam model has been incorporated to solve Eq. (2) in one-dimension, i.e. $\Delta = \partial^2/\partial x^2$. To simulate large displacement wing motions geometrically nonlinear structural dynamics equations are modeled with a flexible multi-body type finite element using triangular shell elements [94]. The rigid-body motions are prescribed in the global frame of reference in addition to a co-rotational framework to account for the geometric nonlinearities. By applying the co-rotational frame transformations the motion of an element is decomposed into the rigid-body motion part and the pure deformation part. By using linear elasticity theory for the latter, the co-rotational formulation can efficiently solve for the structural dynamics with small strains, yet large rotations. A linear combination of an optimal membrane element and a discrete Kirchhoff triangle plate bending element is employed for the elastic stiffness of a shell element [121].

2.7 Fluid-Structure Interaction Interface

The fluid-structure interaction (FSI) is based on a time-domain partitioned solution process in which the nonlinear partial differential equation governing the fluid and the structure are solved independently and spatially coupled through the interface between the fluid and the structure. An interface module has been added to the fluid solver to communicate the parallelized flow solutions on the three-dimensional wetted surface to and from the serial structural solver. At each time step the fluid and the structural solvers are called one after the other until sufficient convergence on the displacements on the shared boundary surface are reached in an inner-iteration before advancing to the next time step. Full details of this algorithm are described in Ref. [77]. In this dissertation, in order to accelerate and ensure the convergence of the FSI the Aitken relaxation method [122] has been incorporated. The Aitken relaxation method is a fixed-point FSI-coupling method with dynamic relaxation. The FSI-coupling for partitioned domain can be summarized for the FSI-interface Γ as,

$$\tilde{\boldsymbol{w}}_{\Gamma}^{n+1} = \boldsymbol{S}_{\Gamma}^{-1}\left(\boldsymbol{F}_{\Gamma}\left(\boldsymbol{w}_{\Gamma}^{n+1}\right)\right). \tag{20}$$

where $\boldsymbol{F}_{\Gamma}$ denotes the fluid solver, $\boldsymbol{S}_{\Gamma}$ is the structural solver, $\boldsymbol{w}_{\Gamma}^{n+1}$ is the displacement of the interface Γ at the next time level $n+1$, and $\tilde{\boldsymbol{w}}_{\Gamma}^{n+1}$ is the displacement output from the structural solver.

For weakly coupled systems $\tilde{\boldsymbol{w}}_{\Gamma}^{n+1} \approx \boldsymbol{w}_{\Gamma}^{n+1}$ and the so-called explicit coupling can be used where the information between the fluid solver and the structural solver is communicated only once. If a structure is very light and flexible, the fluid forces will impact the structural deformations dominantly. Then the added mass effects become important and either monolithic solver or strongly coupled implicit scheme with sub-iterations is necessary [122]. In such an iterative coupling Eq. (20) becomes

$$\tilde{\boldsymbol{w}}_{\Gamma,i+1}^{n+1} = \boldsymbol{S}_{\Gamma}^{-1}\left(\boldsymbol{F}_{\Gamma}\left(\boldsymbol{w}_{\Gamma,i}^{n+1}\right)\right). \tag{21}$$

where now i is the iterator over the FSI-coupling.

In order to ensure and accelerate convergence of the iteration, a relaxation step is needed after each FSI-subiteration in Eq. (21),

$$\boldsymbol{w}_{\Gamma,i+1}^{n+1} = \tau_i \tilde{\boldsymbol{w}}_{\Gamma,i+1}^{n+1} + (1-\tau_i)\boldsymbol{w}_{\Gamma,i}^{n+1} \tag{22}$$

A relaxation factor τ_i should be sufficiently small to prevent the divergence of the FSI coupling, but large enough to reduce unnecessary FSI-iterations. If a prefixed relaxation factor is used trial and error type of experimentation is needed to find an optimum value for each case. There are a number of methods to dynamically determine the relaxation factor. In the Aitken's relaxation method, by using secant like method for the unknown displacements, a recursive expression for the relaxation parameter can be estimated as

$$\tau_{i+1} = -\tau_i \frac{(\boldsymbol{r}_{\Gamma,i+1})^T (\boldsymbol{r}_{\Gamma,i+2} - \boldsymbol{r}_{\Gamma,i+1})}{|\boldsymbol{r}_{\Gamma,i+2} - \boldsymbol{r}_{\Gamma,i+1}|^2} \tag{23}$$

where the residual is given as $\boldsymbol{r}_{\Gamma,i+1} = \widetilde{\boldsymbol{w}}_{\Gamma,i+1} - \boldsymbol{w}_{\Gamma,i}$. The idea is to use the residuals from the previous two iterations to predict the solution using the secant method. In a vector extrapolation method [123] the relaxation factor is predicted based on all the residuals. In Ref. [123] it has been shown that the Aitken method is simpler to implement and often provides faster convergence.

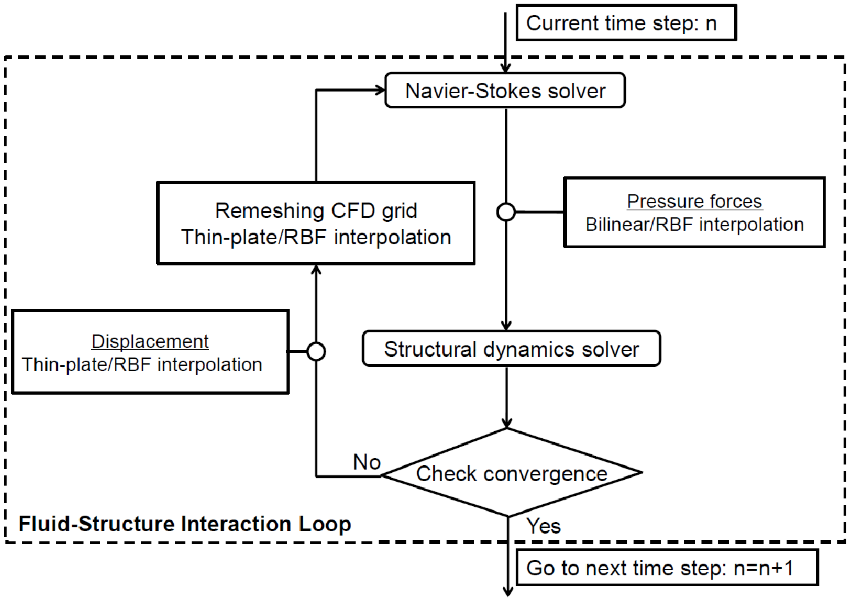

Figure 2-8 Diagram for time marching loop of fluid-structure interaction.

The fluid and the structural solutions are considered to be synchronized for given tolerance ϵ, if $|\boldsymbol{r}_{\Gamma,i+1}|_2 < \epsilon$ for $i \geq N_{\mathrm{FSI}}$. N_{FSI} gives the number of FSI-subiterations. In this dissertation the numerical computations utilize the Aitken's method with the convergence tolerance of $\epsilon = 1.0\times10^{-6}$. See Figure 2-8 for a flow chart of the implemented FSI-coupling used in this dissertation.

Chapter 3.

Scaling of the Forces Acting on a Moving Body Immersed in Fluid

3.1 Introduction

This Chapter starts with a quote from Prandtl: “The undoubted value of theorems [of control-volume analysis] lies in the fact that their application enables one to obtain results in physical problems from just a knowledge of the boundary conditions. There is no need to be told anything about the interior of the fluid or about the mechanism of the motion. These theorems are usually helpful where equations of motion cannot be written down, or at least cannot be integrated, and they give knowledge of the general flow without going into details.” [124]. The conservation equations given by Eq. (1) can be written in an integral form for a given control volume, which can provide a convenient framework in which the balance between the changes inside the volume, transport across the boundary, and the forces acting on a material in the volume can be expressed.

For the case of flapping wings the control volume is time dependent because of the motion of the wing: the boundary surface attached to the wing moves with the motion of either rigid or deforming wing. This motion of the control volume leads to additional terms in the integral balance equations that can be related to the added mass, or apparent mass, terms. The term added mass, or also sometimes called virtual mass [125] originates from the potential theory: For a moving cylinder with radius a in an inviscid fluid at rest at infinity, the integrated pressure on the surface of the cylinder can be found by computing the energy of the fluid motion as [126]

$$2T = M' U_\infty^2 = \pi \rho_f a^2 U_\infty^2, \tag{24}$$

where T is the kinetic energy of the fluid and U_∞ is the velocity of the cylinder. In case of a rectilinear motion, the equation of energy yields

$$(M + M')\frac{dU_\infty}{dt} = F, \tag{25}$$

where M is the mass of the cylinder and F is some external force on the cylinder. Thus the effect of the fluid pressure is equivalent to an addition of inertia of the cylinder, hence the notation ‘added mass’. Note that M' is equal to the fluid mass displaced by unit length of the cylinder. In case of sphere M' is equal to the half of the fluid mass displaced [126].

Following the work by Saffman [125] and Noca [127] a control volume analysis will be performed to obtain an expression for the force acting on a moving body immersed in a fluid. This expression will be then normalized as a function of Reynolds number, Strouhal number, and reduced frequency, introduced in Section 2.2. Finally, by considering limiting cases, different regimes of forces will be proposed that is applicable in flapping wing aerodynamics.

3.2 Scaling of Forces

Consider a control volume of fluid domain V_∞ bounded by S_∞ at infinity in which a body Ω moves in time t and space $x \in V$. Integration of Eq. (1) in V_∞ yields,

$$\begin{aligned} \frac{d}{dt}\int_{V_\infty(t)} \rho_f \boldsymbol{u}\, dV + \int_{\partial\Omega(t)} \boldsymbol{n}\cdot(-p\mathbf{I} + \mathbf{T})\, dS \\ = \int_{S_\infty} \boldsymbol{n}\cdot(-p\mathbf{I} + \mathbf{T})\, dS - \int_{S_\infty} \boldsymbol{n}\cdot(\boldsymbol{u} - \boldsymbol{u}_s)\, \rho_f \boldsymbol{u}\, dS \\ - \int_{\partial\Omega(t)} \boldsymbol{n}\cdot(\boldsymbol{u} - \boldsymbol{u}_s)\, \rho_f \boldsymbol{u}\, dS \end{aligned} \tag{26}$$

where $\partial\Omega(t)$ is the boundary surface of Ω, $\boldsymbol{n}$ the unit normal pointing outward from the body, $\boldsymbol{u}_s$ is the velocity of the surface, $\mathbf{I}$ the unit tensor, and $\mathbf{T}$ the viscous stress tensor.

The force $\boldsymbol{F}$ acting on a moving body Ω immersed in an incompressible viscous fluid is

$$\boldsymbol{F} = \rho_f \int_{\partial\Omega(t)} \boldsymbol{n} \cdot (-p\mathbf{I} + \mathbf{T})\, dS. \tag{27}$$

With no-flow through boundary condition, $(\boldsymbol{u} - \boldsymbol{u}_s) \cdot \boldsymbol{n} = 0$ on $\partial\Omega$ and under the assumption that the viscous terms and convective terms are negligible at S_∞, Eq. (26) simplifies to

$$\boldsymbol{F} = -\frac{d}{dt}\int_{V_\infty(t)} \rho_f \boldsymbol{u}\, dV + \int_{S_\infty} \boldsymbol{n} \cdot (-p\mathbf{I})\, dS - \int_{\partial\Omega(t)} \boldsymbol{n} \cdot (\boldsymbol{u} - \boldsymbol{u}_s)\, \rho_f \boldsymbol{u}\, dS. \tag{28}$$

Based on Eq. (28), Noca [127] derived an expression for $\boldsymbol{F}$ for a doubly connected infinite fluid domain V_∞ as

$$\frac{\boldsymbol{F}}{\rho_f} = -\frac{1}{\mathcal{N} - 1}(\boldsymbol{F}_{\mathrm{im}} + \boldsymbol{F}_{\mathrm{a}}) \tag{29}$$

where

$$\boldsymbol{F}_{\mathrm{im}} = \frac{d}{dt}\int_{\mathrm{V}_\infty} \boldsymbol{x} \times \boldsymbol{\xi}\, dV \tag{30}$$

$$\boldsymbol{F}_{\mathrm{a}} = \frac{d}{dt}\int_{\partial\Omega(t)} \boldsymbol{x} \times (\boldsymbol{n} \times \boldsymbol{u})\, dS \tag{31}$$

where $\mathcal{N}$ is the spatial dimension and $\boldsymbol{\xi} = \boldsymbol{\nabla} \times \boldsymbol{u}$ is the vorticity. The first integral, $\boldsymbol{F}_{\mathrm{im}}$, represents the time derivative of the hydrodynamic impulse, see e.g. [125], which is equal to the non-conservative external body forces for inviscid flows. Following the discussion given by Saffman [125], consider a three-dimensional flow field resulting from a motion of a moving body, such that the vortices are confined in a material volume, V_{v}. Then we have for the impulse

$$\begin{aligned}\boldsymbol{F}_{\mathrm{im}} &\approx \frac{d}{dt}\int_{V_{\mathrm{v}}} \boldsymbol{x}\times\boldsymbol{\xi}\,dV_{\mathrm{v}} = \int_{V_{\mathrm{v}}} \boldsymbol{x}\times\frac{D\boldsymbol{\xi}}{Dt}+\boldsymbol{u}\times\boldsymbol{\xi}\,dV_{\mathrm{v}} \\ &= 2\int_{V_{\mathrm{v}}} \frac{\mu}{\rho_f}\,\boldsymbol{x}\times\nabla^2\boldsymbol{\xi}\,dV_{\mathrm{v}} + 2\int_{V_{\mathrm{v}}} \boldsymbol{u}_{\mathrm{e}}\times\boldsymbol{\xi}\,dV_{\mathrm{v}}\end{aligned} \tag{32}$$

where the external velocity $\boldsymbol{u}_{\mathrm{e}}$ is due to other vortices not confined in V_{v} or the motion of the body. Because of the time evolution of the vorticity in the flow field, the force due to this term may have different phase than the motion of the body. Saffman [125] also proves that for inviscid, irrotational flow without net circulation around Ω the second integral in Eq. (29), $\boldsymbol{F}_{\mathrm{a}}$, represents the acceleration-reaction force, or the force due to added mass. Noca [127] further shows that for an impulsively starting flat plate in a viscous flow with no-slip boundary condition on Ω in quiescent fluid the force acting on the body has the same expression immediately after the start of the motion.

Using the non-dimensionalization procedure introduced in Section 2.2 the magnitudes of the force components in Eq. (29) are estimated as follows. For the hydrodynamic impulse term, if we assume that the vorticity is confined in a rectangular fluid region in the order of $O(c_{\mathrm{m}})$ in the streamwise direction and $O(h_a)$ in the normal direction and that $x \sim c_{\mathrm{m}}$, $\xi \sim U_{\mathrm{ref}}/c_{\mathrm{m}}$, and $u_{\mathrm{e}} \sim \omega h_a$ in the integrand Eq. (32),

$$C_{F,\mathrm{im}} \sim St\left\{\frac{1}{Re\,k}\,O(1)+\frac{St}{k}\,O(1)\right\}. \tag{33}$$

as a first order approximation. Hence the force due to the hydrodynamic impulse scales with St, however if the viscous time scale, c_{m}^2/ν, is much greater than the motion time scale, $1/\omega$, such that $Re\,k \gg 1$, then the first term in Eq. (33) becomes negligible. Moreover, when the plunge amplitude $h_a/c_{\mathrm{m}} \sim St/k$ is small the second term in Eq. (33) will only have a small contribution to the total force felt on the wing. In general, however, complex fluid dynamics mechanisms, such as the wing-wake interaction, or the wake-wake interactions would additionally affect the vorticity distribution in the flow field.

Similarly, the acceleration-reaction force can be non-dimensionalized as

$$C_{F,\mathrm{a}} \sim St\, k, \tag{34}$$

with $u \sim \omega h_a$ in the integrand of Eq. (31). This non-dimensionalization process reveals that for high St the fluid dynamic force is expected to be great. On the other hand, if the motion is highly unsteady, i.e. k is high, the force due to the motion of the body appearing as the acceleration-reaction component, dominates over the forces due to vorticity in the flow field. It should be noted that this scaling is not unique. For example, if the normal direction of the material volume in Eq. (32) is to be estimated as to be proportional to $O(c_{\mathrm{m}})$, then the scaling for the hydrodynamic impulse term would loose the factor St/k, however the added mass term would still be dominant for high k and high Re flows.

A parametrization of special interest for flapping wing community is the dependence of the force on the flapping motion frequency, ω. The current scaling shows that for forward flight with $U_{\mathrm{ref}} = U_\infty$ the added mass has the largest order of frequency as $\sim \omega^2$. The resulting dimensional force is then proportional to square of the motion frequency. Similarly, for hovering motions the current scaling shows that the non-dimensional force is independent of the motion frequency since the Strouhal number is a constant and the reduced frequency only a function of flapping (plunging) amplitude. However, since $U_{\mathrm{ref}} \sim \omega^2$ the resulting dimensional force is also proportional to square of the motion frequency. Similar observations were reported by Gogulapati and Friedmann [72] who conducted potential theory based aerodynamic analysis of hovering wings.

At the reduced frequency of 3.93, Visbal, Gordnier, and Galbraith [60] considered a high frequency small amplitude plunging motion at $Re = O(4)$ over a three-dimensional SD7003 wing (α_0 = 4 deg; k = 3.93; St = 0.06; Re = 1×10^4, 4×10^4). They used the iLES simulations to solve for the flow structures including the laminar-to-turbulence transition and the forces on the wing. The flow field exhibits formation of dynamic-stall like leading edge vortices, breakdown due to spanwise instabilities, and transitional features, however the forces on the wing could still be well predicted by the Theodorsen Eq. (38) formula for lift. The time history of lift was “independent of Reynolds number and of the 3-D transitional aspects of the flow field” [60]. They explained that the lift is dominated by the acceleration of the airfoil, which is proportional to the square of the motion frequency. This observation is also consistent with the scaling that the hydrodynamic impulse term Eq. (30) is small compared to the added mass term Eq. (31) for the given non-dimensional parameters.

On the other hand, at lower Reynolds numbers, Trizila *et al.* [128] have shown at Re = 100 and k in the range of 0.25 – 0.5 that the formation and interaction of leading edge and trailing edge vortices with the airfoil and previous shed wake substantially affect the lift and power generation for hover and forward flight. Furthermore, three-dimensionality effects play a significant role, for instance for a delayed rotation kinematics (k = 0.5; low angle of attack; Re = 100) the tip vortex generated at the tip of the AR = 4 flat plate would interact with the leading edge vortex enhancing lift compared to its two-dimensional counterpart, which contrasts the classical steady-state thin wing theory [128], [29] which predicts the formation of wing tip vortices as lift reducing flow feature. This complex interplay between the kinematics, the wing-wake, wake-wake interactions, and the fluid dynamic forces on the wing at the given range of non-dimensional parameters is also consistent with the scaling analysis described in this Section.

In Chapter 4 the interplay between the airfoil shape, kinematics, Reynolds number, and the resulting aerodynamics will be probed at $Re = O(10^6)$. The reduced frequency is k = 0.25 and the Strouhal number is St = 0.04. According to the scaling proposed in this section not only the acceleration-reaction term, but also the hydrodynamic impulse term, i.e. interaction with the vorticity distribution in the flow field, will contribute to the force on the wing. Furthermore, in Chapter 5 the effects of flexibility will be investigated by approximating the fluid force by the acceleration-reaction term at Reynolds number $O(10^3 - 10^4)$ and k between $O(1 - 10)$.

3.3 Linearized Aerodynamic Theories

When a body accelerates in a fluid, the fluid kinetic energy changes. The rate of work done by pressure moving the body in an inviscid fluid yields a force that is proportional to the acceleration (see e.g. [129]). Then, the constant of proportionality has the dimension of mass, hence the name added mass. The added mass term is usually some fraction of the fluid mass displaced by the body. Determination of the added mass, which is a tensor, because it relates the acceleration vector to the force vector, is not easy in general because the local acceleration of the fluid is not necessarily the same as the acceleration of the body and depending on the direction of the motion, cross-correlation terms appear [90]. However, for simple geometries in translating motions, the added mass can be obtained explicitly. For an accelerating thin flat plate with a chord length of c_{m} normal to itself, the force acting normal to the flat plate, can be computed as follows. The velocity potential difference is (e.g. [90]),

$$\Delta\phi = c_m v_i \sqrt{1 - \left(\frac{x}{c_m/2}\right)^2} \tag{35}$$

where v_i is the vertical velocity component. Hence the vertical component of the force acting on the flat plate due to added mass becomes,

$$\begin{aligned} \rho_f F_{\mathrm{a}} &= \rho_f \frac{d}{dt} \int_{\Omega(t)} \boldsymbol{x} \times (\boldsymbol{n} \times \boldsymbol{u}) dS \\ &= \rho_f \frac{d}{dt} \int_{\Omega(t)} \boldsymbol{x} \times (\boldsymbol{n} \times \boldsymbol{\nabla}\phi) dS \\ &= -\rho_f \int_{\Omega(t)} \phi \boldsymbol{n} dS = -\rho_f \frac{d}{dt} \int_{\frac{c_m}{2}}^{-\frac{c_m}{2}} \Delta\phi \, dx \\ &= \frac{d}{dt} \left(\rho_f \frac{\pi}{4} v_i c^2\right) \end{aligned} \tag{36}$$

whence the added mass of a vertically accelerating thin flat plate is equal to the displaced fluid cylinder with radius $c_m/2$.

For a harmonically plunging thin rigid flat plate in a freestream the lift coefficient can be derived assuming inviscid incompressible flow as

$$C_L = 2\pi^2 St\, k \cos(\omega t) + 4\pi^2\, St \sin(\omega t) \tag{37}$$

assuming quasi steady-state flow where the influence of the wake vorticities are neglected. The first term in Eq. (37) is the non-circulatory term which is consistent with the added mass force derived in Eq. (31). The second term in Eq. (37) is the circulatory term, which can be expressed in a more familiar form, $2\pi\alpha_{\mathrm{e}}$, by recognizing that $2\pi\, St \sin(\omega t) \approx \alpha_{\mathrm{e}}$ where α_{e} is the effective angle of attack for purely plunging motions. Both terms are also consistent with the scaling found in Eq. (33) and Eq. (34).

A more accurate representation of the lift coefficient beyond the quasi-steady approximation was Theodorsen [130], for sinusoidal pitch-plunge of a thin airfoil, by assuming a planar wake and a trailing-edge Kutta condition, in incompressible inviscid flow. The lift coefficient time history is then

$$\begin{aligned} C_L &= 2\pi\{1 - C(k)\}\alpha_0 \\ &+ \pi k\{\alpha_a i e^{\psi i} - 2\pi St - \alpha_a k(2x_p - 1)e^{\psi i}\}e^{2\pi t^* i} \\ &+ 2\pi C(k)\left\{2\pi St\, i + \alpha_a e^{\psi i} + \alpha_a\left(\frac{3}{2} - 2x_p\right)ki\, e^{\psi i}\right\}e^{2\pi t^* i}. \end{aligned} \tag{38}$$

The pitch and plunge motions are described by the complex exponentials, $\alpha(t^*) = \alpha_0 + \alpha_a e^{(2\pi t^* + \psi)i}$ and $h(t^*) = St\, \pi/k\, e^{2\pi t^* i}$. The phase lead of pitch compared to plunge is denoted by ψ. In the most common case, motivated by considerations of maximum propulsive efficiency, pitch leads plunge by 90º, which results in $\psi = \pi/2$ [131]. The $C(k)$ is the complex-valued *Theodorsen function* with magnitude ≤ 1. It accounts for attenuation of lift amplitude and time-lag in lift response, from its real and imaginary parts, respectively. The first term is the steady-state lift and the second term is the noncirculatory lift due to acceleration effects. The third term models circulatory effects. Setting $C(k) = 1$ recovers the quasi-steady thin airfoil solution. Note that $C(k) = 1$ for pure plunge kinematics with $\alpha_0 = \alpha_a = 0$ yields Eq. (37).

3.4 Summary

This Chapter proposes a scaling for the force acting on a moving body immersed in a viscous fluid. Based on a control volume analysis of conservation of momentum, an integral equation was derived involving two terms: i) hydrodynamic impulse term and ii) added mass term. The scaling for these terms are summarized in Table 3-1. The scaling shows that for low reduced frequency motions or low Reynolds number flows the hydrodynamic impulse term, which indicate the interaction between the vortices and the wing become important. On the other hand, when the reduced frequency increases the added mass term will dominate over the hydrodynamic terms. Both components are proportional to the Strouhal number.

Table 3-1 Summary of the force scaling

Force	Scaling	Note
Hydrodynamic Impulse	$\frac{St}{Re\ k}.$	viscous term
	$\frac{St^2}{k}$	vortex force due to motion of moving body
Added mass	$St\ k$	

An interesting consequence that needs to be investigated more is that for hover motion where both Strouhal number and reduced frequencies are independent of motion frequency, the normalized force will be independent of frequency, for high Reynolds number flows.

Chapter 4.

Fluid Dynamics of Rigid Flapping Wings at $Re = O(10^4)$ and $k = 0.25$

4.1 Introduction

In this Chapter the numerical modeling aspects and the interplay between the imposed kinematics, the resulting flow structures, and the resulting force on the rigid wings of nominally two-dimensional wings undergoing combined pitching and plunging at Reynolds numbers 1×10^4, 3×10^4, and 6×10^4 are studied. The reduced frequency k is kept fixed at 0.25, which is low, such that the hydrodynamic impulse term in Eq. (29) will play a non-negligible role. The focus of this chapter is to probe the implications of the kinematics, the airfoil shapes and the Reynolds number on the fluid dynamics at $Re = O(4)$ for rigid wings.

Experimental and computational flow field results are compared: two versions of Menter's Shear Stress Transport (SST) turbulence closures for two-dimensional RANS computations, and phase-averaged Particle Image Velocimetry (PIV) measurements [119]. The experiments were obtained in two different facilities, one at the Air Vehicle Directory of the Air Force Research Laboratory (AFRL) [131] and the other at Department of Aerospace Engineering of the University of Michigan (UM) [119]. The consistency and inconsistency of the experimental as well as computational endeavors offer significant opportunities for us to probe the modeling and experimental implications, and the interplay between fluid physics and geometry and pitching and plunging motion under different Reynolds numbers. This work had been a collaborative effort under the Research and Technology Organization of the NATO and this chapter highlights the main findings from the computational perspective. Detailed experimental setup, comparisons to the experimental measurements, and more extensive description of the fluid physics can be found in Refs. [131,132,119,58,133]. In this dissertation the transition from laminar to turbulence has not been modeled in the numerical computations.

4.2 Case Setup

Two different airfoils are considered: the SD7003 airfoil and a flat plate with 2.3 % thickness ratio, see Figure 4-1, to discuss the airfoil shape effects by comparing the aerodynamic loading and flow field. The thickness of the airfoil and the airfoil leading edge shape characterizes the radius of curvature at the leading edge. Sane [18] used the Polhamus' leading edge suction analogy [134] to explain the lift characteristics of thinner airfoils compared to blunter airfoils. The flow around blunt airfoils moves sharply around the airfoil nose creating a leading edge suction force parallel to the airfoil chord tilting the resulting aerodynamic force normal to the incoming flow. On the other hand, flow over an airfoil with sharp leading edge separates at the leading edge, forming a LEV. The suction force due to the LEV acts normal to the airfoil, enhancing the lift and the drag.

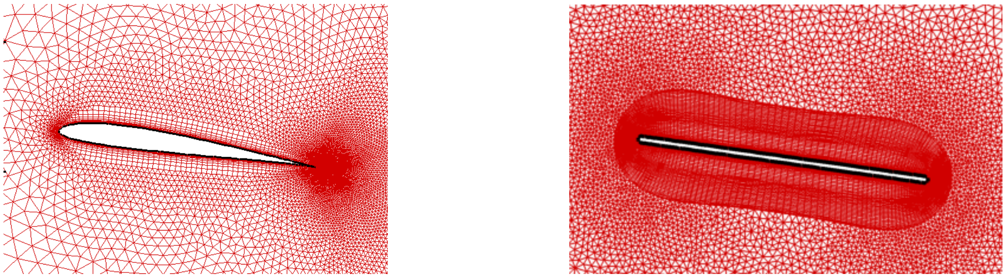

(a) SD7003 (b) flat plate

Figure 4-1 Airfoil shapes and the mesh used.

The two different sets of kinematics are given by Eq. (4) and Eq. (5), which are repeated as

$$h(t^*) = St\frac{\pi}{k}\cos(2\pi t^*),$$
$$\alpha(t^*) = \alpha_0 + \alpha_a\cos(2\pi t^* + \phi) \tag{39}$$

that represent a weak dynamic stall (under combined pitching-plunging, St = 0.04; k = 0.25; α_0 = 8 deg; α_{a} = 8.43 deg; ϕ = 90 deg) and a stronger dynamic stall (under pure plunging: St = 0.04; k = 0.25; α_0 = 8 deg; α_{a} = 0 deg; ϕ = 90 deg), respectively. The effective angle of attack, α_{e}, is

$$\alpha_{\mathrm{e}} = \alpha + \arctan\{2\pi\, St \sin(2\pi t^*)\} \tag{40}$$

and the time history of both kinematics are summarized in Figure 4-2, where α_{e}, approaches the static stall value for the SD7003 airfoil of approximately 11° [135] for the pitching and plunging case, while the maximum effective angle of attack exceeds well beyond the static stall angle, which leads to large vertical structures in the flow field. The grid and time step sensitivity studies are shown in Appendix A.1 for the SD7003 airfoil and Appendix A.2 for the flat plate.

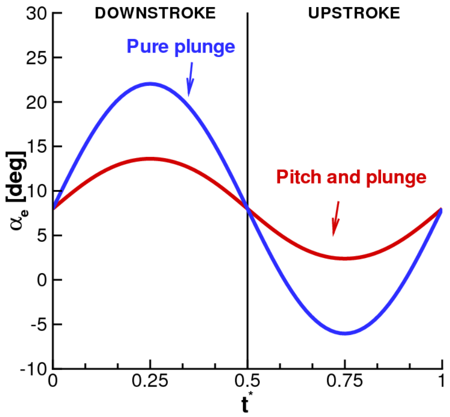

Figure 4-2 Time history of effective angle of attack α_{e} for the pitching and plunging kinematics (red line) and the pure plunging kinematics (blue line).

4.3 Flow over 2D SD7003 Airfoil at *Re* = 6×10^4

Figure 4-3 shows the normalized mean streamwise velocity, u_1^*, contours along with planar streamlines from the numerical and the experimental results from the UM and AFRL at t^* = 0.00, 0.25, 0.50, and 0.75, respectively for a combined pitching and plunging SD7003 airfoil at $= 6\times10^4$. The agreement with the two experimental measurements is excellent, both in streamwise velocity contours as well as in streamlines. The flow exhibits separation between the center of the downstroke and the bottom of the downstroke, corresponding to the maximum instantaneous effective angle of attack of 13.6°. Note that this value for the effective angle of attack is well beyond the static stall angle of 11°.

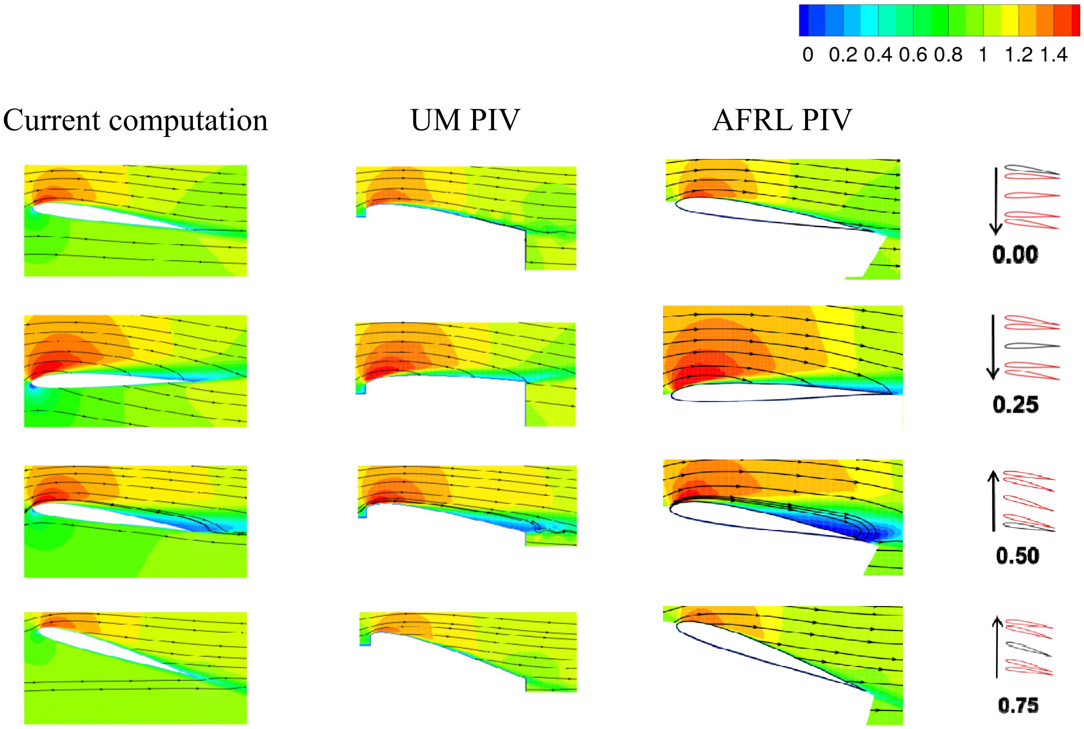

Figure 4-3 contours and the instantaneous streamlines over pitching and plunging SD7003 airfoil at $= 0.25$, $=0.08$, and at $= 6\times10^4$ from numerical, and experimental (UM, AFRL) results.

For the deep stall kinematics, the time evolution of the flow field changes significantly. Figure 4-4 shows the contour plots and the instantaneous streamlines from the numerical computation and the experimental measurements from the UM and AFRL water tunnels for the pure plunging SD7003 airfoil at $= 0.00, 0.25, 0.50$, and 0.75. Unlike the pitching and plunging case where the flow showed only a thin open separation, the pure plunging case generates large vortical structures at the leading edge between motion phases of 0.25 and 0.33. Subsequently, this leading edge vortex (LEV) broadens, weakens, and convects downstream, eventually enveloping the entire airfoil suction side. At the bottom of the downstroke, reattachment is evinced at the leading edge, and sweeps downstream as the airfoil proceeds on the upstroke. The LEV and its subsequent development enhance suction, and thus also lift. The agreement between the computational and the experimental approaches is favorable when the flow is largely attached. When the flow exhibits massive separation, for example at = 0.50, the experimental and computational results show noticeable differences in phase as well as the size of flow separation. The details of the vortical structures differ in all results; however, it is interesting to observe that the original SST model matched the PIV results from the UM better, while the modified SST model produced result more consistent with that from the AFRL facility. The consistent/inconsistent results appeared at = 0.50 where a smaller vortical structure is evinced on the suction side of the airfoil in the UM facility, while in AFRL data such a vortical structure is hardly present.

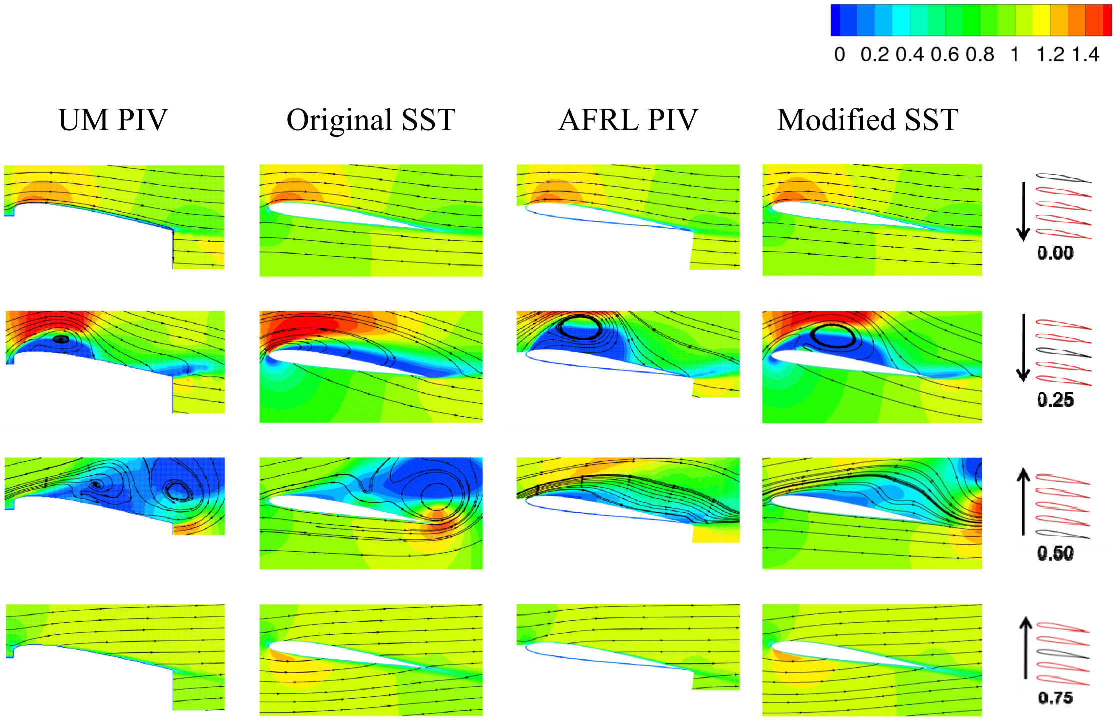

Figure 4-4 contours and the instantaneous streamlines over purely plunging SD7003 airfoil at = 0.25, =0.08, and at = 6×10^4 from numerical (original SST, modified SST), and experimental (UM, AFRL) results.

The flow tends to separate more substantially under the modified SST model than under the original SST model due to different eddy viscosity levels predicted. The overprediction of separation when using the modified SST model could be explained by the use of a limiter for the production term in the TKE equation, Eq. (9). The build-up of turbulence near stagnation flow region is prevented, reducing the eddy viscosity in the RANS model. The limiter of the production in the TKE equation enforced in the modified SST model results in substantially lower eddy viscosity, and hence higher local Reynolds number defined as $\rho_f U_\infty c_\mathrm{m}/(\mu + \mu_t)$. Hence the flow tends to separate near the leading edge which is observed at t^* = 0.50 in Figure 4-4.

4.4 Shape Effect: Pitching and Plunging 2D Flat Plate at Re = 6×10^4

Polhamus' leading edge suction analogy [134] predicts that the curvature of the leading edge of the airfoil is important to the overall flow structure over the airfoil. Figure 4-5 shows the normalized mean streamwise velocity, u_1^*, contours along with planar streamlines from the numerical and the experimental results from the UM and AFRL at t^* = 0.00, 0.25, 0.50, and 0.75, respectively for a combined pitching and plunging flat plate at Re = 6×10^4. The flow is characterized by separation from the leading edge over the majority of the motion cycle. The evolution of the qualitative flow features is observed as follows. At top of the downstroke, t^* = 0.00, the boundary layer undergoes separation at the leading edge but reattaches before the half chord. After the reattachment a thin shear layer forms that covers suction side of the flat plate. As the flat plate plunges downwards the effective angle of attack increases, reaching its maximum at t^* = 0.25 (see Figure 4-2) and the flow separates at the leading edge due to the small curvature, which is directly related to the thickness of the flat plate, at the leading edge. Vorticity is fed from the leading edge into a coherent vortex structure. This large scale vortical flow feature is evinced during the most of the downstroke, convecting downstream, until it eventually detaches from the flat plate at the bottom of the downstroke, t^* = 0.50. A TEV rolls up in the second half of the downstroke due to the interaction with closed separated region and sharp trailing edge: The direction of the vorticity shed from the leading-edge is the opposite of that of TEV, as well as the change of sign of the angular rotation of the flat plate at = 0.25, promote the TEV generation: the geometric angle of attack starts to increase at = 0.25 such that the roll-up of TEV is favorable. In the upstroke the boundary layer reattaches.

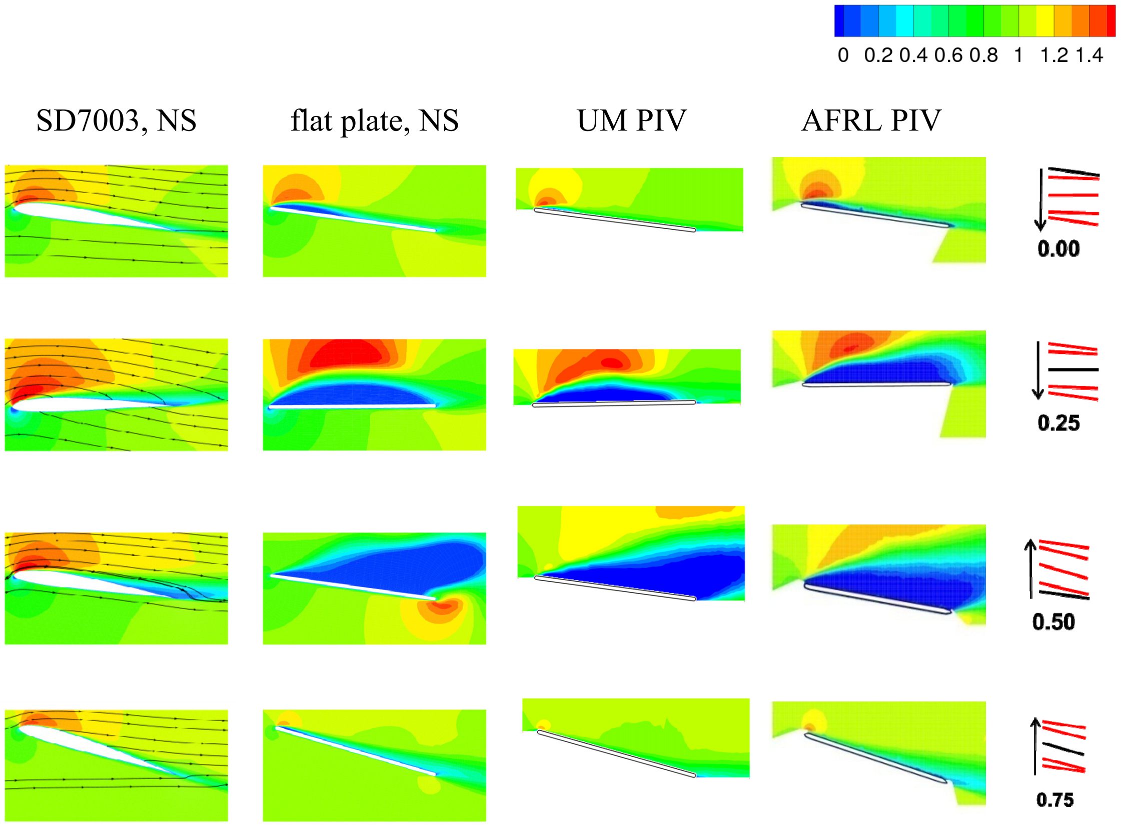

Figure 4-5 contours and the instantaneous streamlines over pitching plunging flat plate airfoil at = 0.25, =0.08, and at = 6×10^4 from numerical and experimental (UM, AFRL) results. As a reference the numerical computation of the flow field over the SD7003 airfoil is shown in the first column.

Qualitatively all contours agree well. In the experiment the leading edge separation and the vortical structure generated as the effective angle of attack increases, has phase delay compared to the numerical results as shown by the location of the maximal accelerated flow region at = 0.25, and 0.50. Furthermore, the leading edge effect overwhelms the difference between turbulence models: The differences using the original and the modified SST turbulence model are small [119]. It is shown in Ref. [119] that similar eddy viscosity effects as the flow over SD7003 are observed that the eddy viscosity level in the result using the modified SST model is lower at the leading edge compared to the computation using the original version of SST. However, in the critical regions above the plate, the two models produce comparable eddy viscosity distributions due to the leading edge effect. Consequently, the resulting flow structures from the two models are similar as well.

In order to investigate the effects of airfoil shapes in the case of pure plunging, and pitching and plunging motion on the time histories of lift coefficient, the comparisons are shown in Figure 4-6 for Re = 1×10^4, 6×10^4. Note that the lift coefficients are obtained using the original SST turbulence model shown in Figure 4-6 .

It is clear that the results of the flat plate (blue lines in Figure 4-6) show larger lift peaks than those of the SD7003 airfoil (red lines in Figure 4-6) within the range of Reynolds number and airfoil kinematics considered in this dissertation. Moreover, it is found that there is phase delay of peak in the case of pure plunging at Re = 6×10^4 [133]. This is because the flow separates earlier over the flat plate during downstroke due to the sharp leading edge of the flat plate, see Figure 4-3 and Figure 4-5.

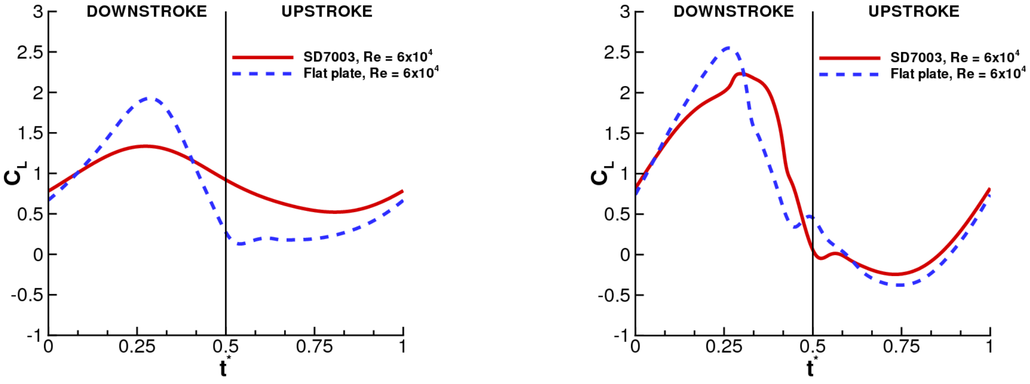

(a) pitching and plunging, Re = 6×10^4 (b) pure plunging, Re = 6×10^4

Figure 4-6 Time histories of pitching and plunging, and pure plunging two-dimensional flat plate (blue line), and SD7003 airfoil (red line) at k = 0.25, and St = 0.04 at Re = 6×10^4.

4.5 Reynolds Number Effect: Re = 6×10^4 to 1×10^4 for a Pitching and Plunging 2D Flat Plate

To assess the effects of Reynolds number on the flow field and the resulting aerodynamic loading on a pitching and plunging flat plate both experimental and numerical results have been obtained for Re = 1×10^4, 3×10^4, and 6×10^4. In the range of Reynolds number considered in the present study, the Reynolds number sensitivity to the qualitative flow structures is small. This is in contrast to the flows at lower Reynolds number regimes, e.g. $O(10^2)$ [3,6,136,35,39], where the viscosity plays a more important role than at the current Reynolds number, or for the airfoil geometries with larger radius of curvature at the leading edge as discussed in Section 4.3. At t^* = 0.00 when the flow is attached the viscosity plays a role in shaping u_1^* profile as shown in Figure 4-7, which plots the streamwise velocity profiles at three Reynolds numbers, Re = 1×10^4, 3×10^4, and 6×10^4 from the numerical and experimental results. At x_1^* = 0.25 the u_1^* profiles from the experiments at Re = 6×10^4 show attached flow, and at Re = 1×10^4 separated flow. On the other hand, when the flow is largely separated as at t^*= 0.50, see Figure 4-8, the influence from the Reynolds number is negligible, and the numerical computation agrees well with the experiment.

Figure 4-9 shows the vorticity distributions at the bottom of the downstroke, t^* = 0.50, at Re = 3×10^4 and 1×10^4. Compared to the Re = 6×10^4 case, the large scale flow features such as the vorticity concentration and the secondary vortex only observed in the numerical computation above the flat plate as well as the trailing edge vortices remain similar, but these are made up by smaller regions of concentrated vorticities. The experimental results show a focus type vortex without closed streamlines, while the numerical computation shows a center type vortex with closed streamlines, which can be ascribed to the mass conservation that the experimental result is inherently three-dimensional, while the numerical computation is done in two-dimensional space.

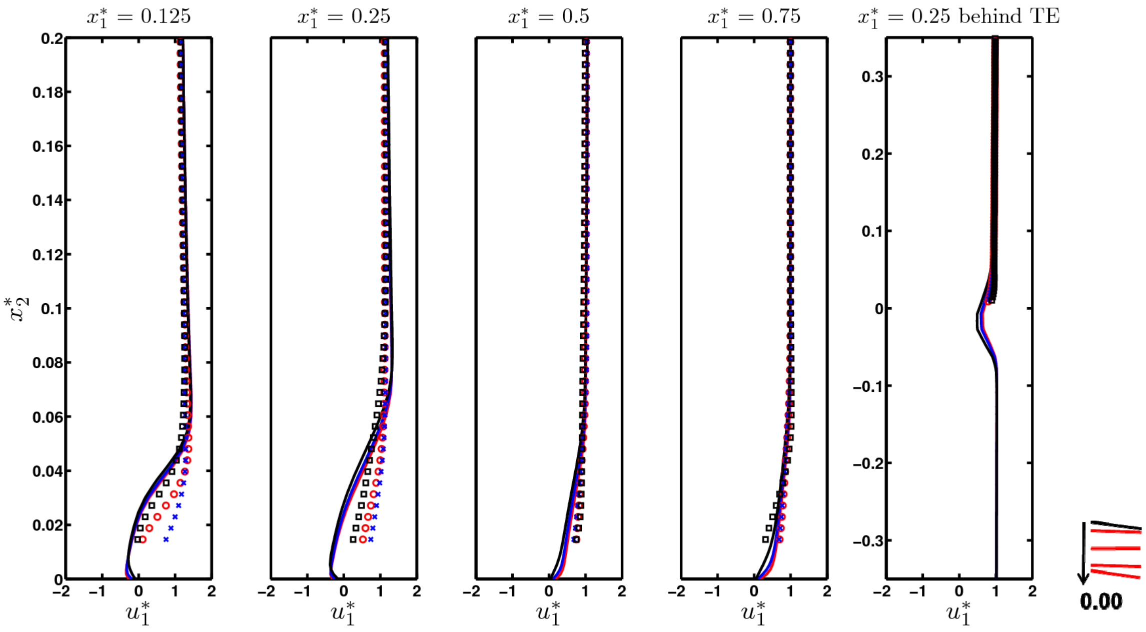

Figure 4-7 profiles from the numerical and experimental results at constant = 0.125, 0.25, 0.50, 0.75, and 0.25 behind the trailing edge at = 0.00 at = 1×10^4, 3×10^4, and 6×10^4, = 0.25, = 0.04 for the pitching and plunging flat plate. Experimental measurements ×: *Re* = 6×10^4; ○: *Re* = 3×10^4; □: *Re* = 1×10^4; Numerical computations —: *Re* = 6×10^4; —: *Re* = 3×10^4; —: *Re* = 1×10^4; The experimental data are from [133].

At these moderately high Reynolds numbers forces due to pressure, which arise from large scale inertial effects, such as LEVs, dominate over viscous forces. The small Reynolds number dependence on the profiles shown in Figure 4-7 and Figure 4-8 and the qualitative similarity in the large scale flow features (= 0.500 in Figure 4-5 and Figure 4-9) suggest that the resulting aerodynamic forces are only partially sensitive to the change of the Reynolds numbers. Figure 4-10 shows the time histories of lift coefficient and drag coefficient from the numerical computations. Both coefficients are on top of each other for = 3×10^4, and 6×10^4 indicating that the Reynolds number effect is minimal for these kinematics. At = 1×10^4 the maximum of lift coefficient around = 0.25 occurs slightly earlier and is smaller in magnitude: = 2.50, than for = 6×10^4 (= 2.55), and 3×10^4 (=2.55). Similarly the time histories of drag coefficient for = 3×10^4, and 6×10^4 coincide whereas for = 1×10^4 the drag is slightly larger between = 0.25 to 1.0. Figure 4-11 shows the lift coefficient as function of effective angle of attack compared to the classical steady-state approximation, [64], and the lift predicted by Theodorsen Eq. (38). The lift coefficient between the middle of the upstroke to the middle of the downstroke (= 0.750 to = 0.250) is closest to the steady-state indicating that the unsteady effects such as LEV development leads to a departure from the steady-state. Note that the lift predicted by Theodorsen has smaller amplitude and a lag compared to the steady-state approximation due to the Theodorsen's function with the reduced frequency being = 0.25.

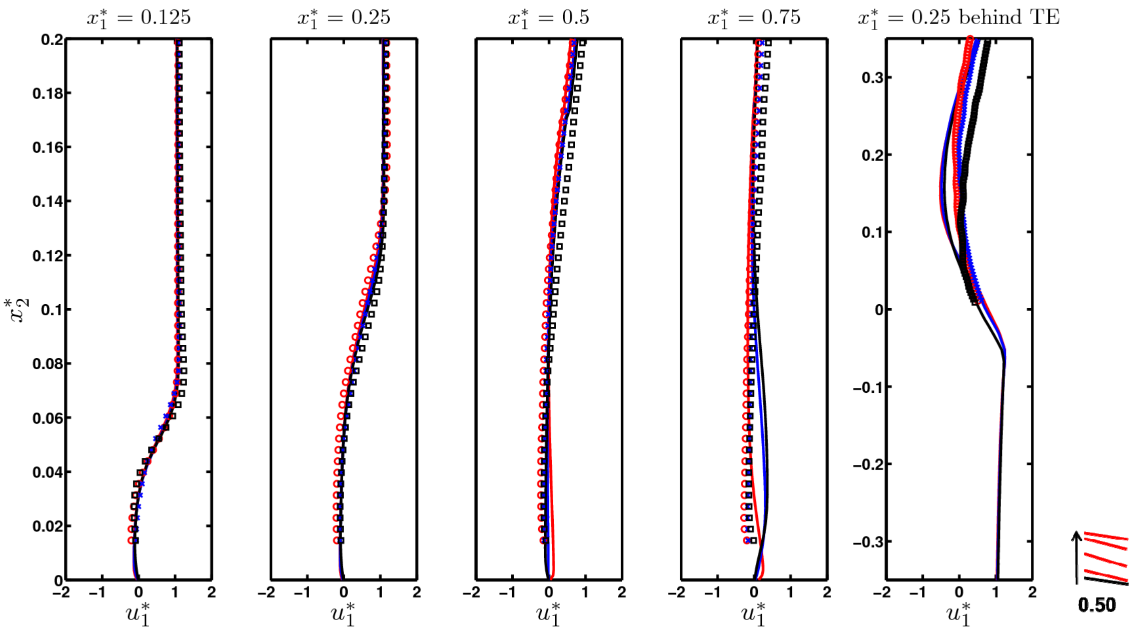

Figure 4-8 profiles from the numerical and experimental results at constant = 0.125, 0.25, 0.50, 0.75, and 0.25 behind the trailing edge at = 0.50 at = 1×10^4, 3×10^4, and 6×10^4, = 0.25, = 0.04 for the pitching and plunging flat plate. Experimental measurements ×: *Re* = 6×10^4; ○: *Re* = 3×10^4; □: *Re* = 1×10^4; Numerical computations —: *Re* = 6×10^4; —: *Re* = 3×10^4; —: *Re* = 1×10^4; The experimental data are from [133].

Mean and maximum force coefficients are summarized as function of Reynolds number in Table 4-1 and in Figure 4-12. The maximum lift is obtained by the flat plate for both kinematics. Furthermore, the force coefficients of the flat plate are insensitive to the Reynolds number. It is also interesting to note that the mean drag coefficient is lower for the SD7003 airfoil, and the mean lift coefficient is larger for the SD7003 airfoil for = 3×10^4, and 6×10^4. In forward flight the direction of propulsion is in the drag or thrust and the work done by the fluid on the wing is given by the lift. Although the current kinematics is not thrust generating, it may be worth to mention that the selection of the flat and thin insect wings may be related to the observation made regarding the lower generation of time-averaged lift for flat plates.

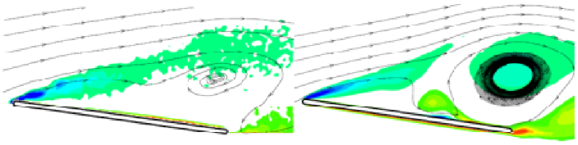

(a) = 6×10^4

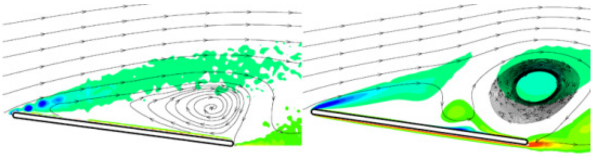

(b) = 3×10^4

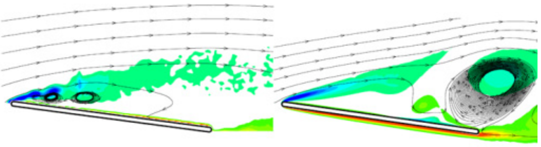

Experiment Computations

(c) = 1×10^4

Figure 4-9 Vorticity contours from the numerical and experimental results at = 0.500 for = 6×10^4, 3×10^4 and 1×10^4, = 0.25, = 0.04 for the pitching and plunging flat plate. The experimental data are from [133].

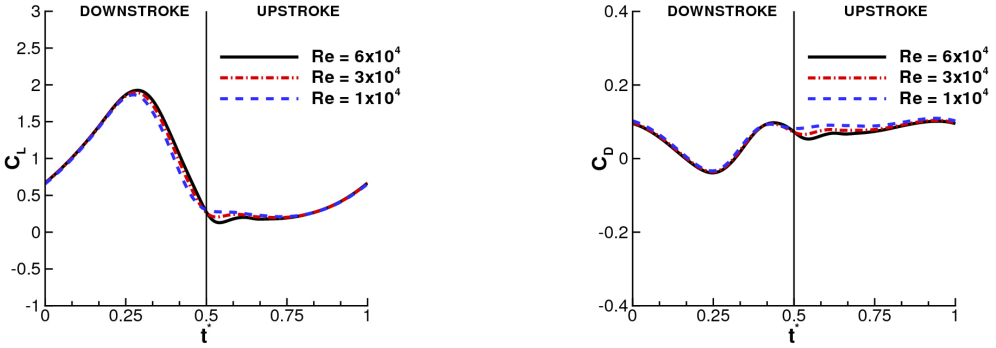

(a) lift coefficient (b) drag coefficient

Figure 4-10 Time histories of (a) lift coefficient and (b) drag coefficient for a pitching and plunging flat plate at = 0.25, = 0.04 for = 1×10^4, 3×10^4, and 6×10^4.

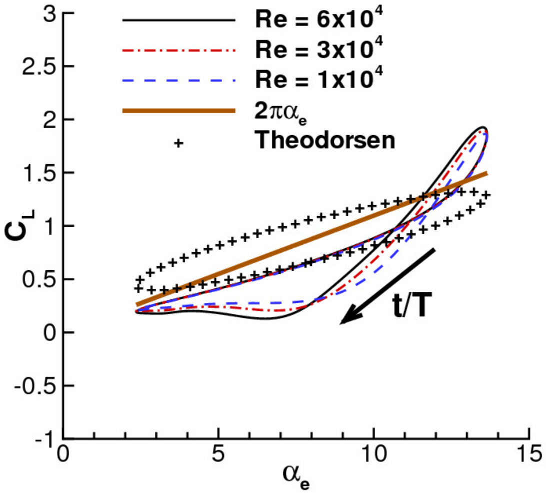

Figure 4-11 Lift coefficient as function of effective angle of attack for a pitching and plunging flat plate at k = 0.25, St =0.04 and Re = 1×10^4, 3×10^4, and 6×10^4.

Table 4-1 Mean and maximum lift and drag coefficients for the investigated Reynolds numbers for the SD7003 airfoil and the flat plate for the pitching and plunging, and the pure plunging at k = 0.25 using the original SST turbulence closure.

Airfoil	Kinematics	Re	$C_{L,\text{ mean}}$	$C_{L,\text{ max}}$	$C_{D,\text{ mean}}$	$C_{D,\text{ max}}$
SD7003	Pitching and Plunging	1×10^4	0.70	1.23	0.032	0.11
SD7003	Pitching and Plunging	3×10^4	0.84	1.30	0.011	0.14
SD7003	Pitching and Plunging	6×10^4	0.89	1.34	0.0039	0.15
SD7003	Pure Plunging	1×10^4	0.69	2.16	0.089	0.30
SD7003	Pure Plunging	3×10^4	0.76	2.15	0.074	0.31
SD7003	Pure Plunging	6×10^4	0.79	2.23	0.063	0.32
Flat plate	Pitching and Plunging	1×10^4	0.75	1.86	0.068	0.11
Flat plate	Pitching and Plunging	3×10^4	0.77	1.90	0.061	0.10
Flat plate	Pitching and Plunging	6×10^4	0.77	1.92	0.057	0.10
Flat plate	Pure Plunging	1×10^4	0.70	2.50	0.12	0.34
Flat plate	Pure Plunging	3×10^4	0.71	2.53	0.12	0.33
Flat plate	Pure Plunging	6×10^4	0.73	2.55	0.12	0.33

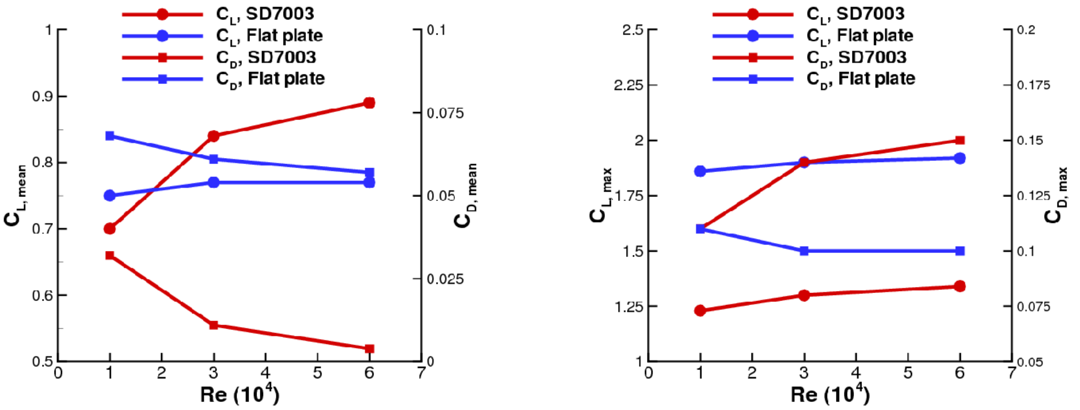

(a) pitching and plunging, mean

(b) pitching and plunging, max

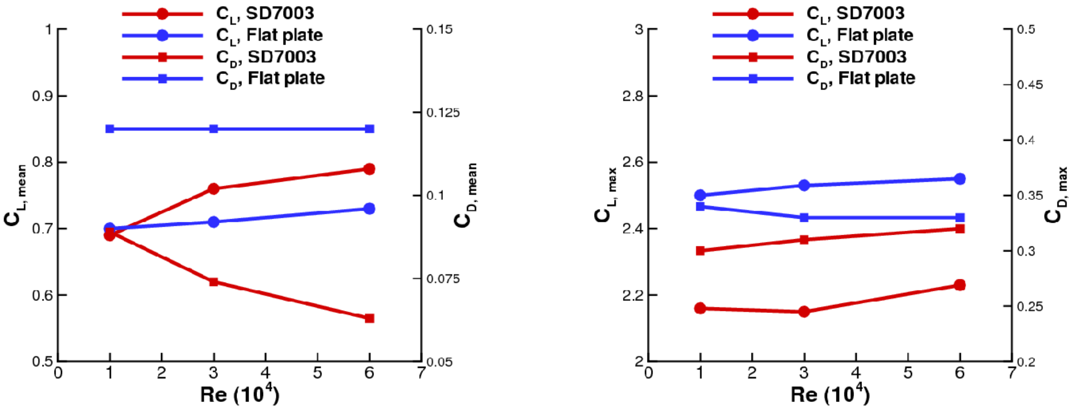

(c) Pure plunging, mean

(d) Pure plunging, max

Figure 4-12 Mean and maximum lift and drag coefficients as function of Reynolds number for the SD7003 airfoil and the flat plate for the pitching and plunging, and the pure plunging at = 0.25.

4.6 Dimensionality Effect: Pitching and Plunging 2D and 3D Flat Plate

Shyy et al. [29] and Trizila et al. [128] demonstrated that for a plunging flat plate with = 4 at *Re* = 64, based on the mean tip velocity, the TiVs could either enhance or degrade the aerodynamics. For a delayed rotation kinematics, the TiV anchored the vortex shed from the leading edge increasing the lift compared to a two-dimensional computation under the same kinematics. On the other hand, under different kinematics with small angle of attack and synchronized rotation, the generation of TiVs was small and the aerodynamic loading was captured by the analogous 2D computation. To investigate the role of 3D effects for the case investigate in the chapter, the pitching and plunging flat plate shown in Section 4.4 and Section 4.5 has been repeated for a flat plate with of 2 at .= 4×10^4.

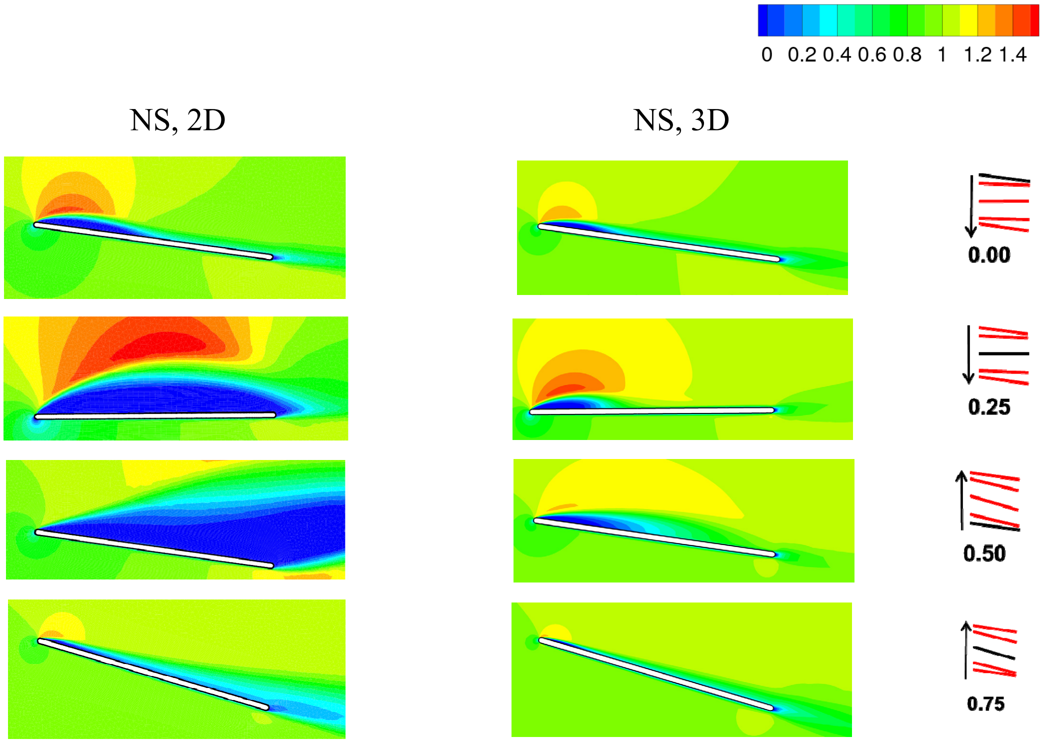

Figure 4-13 contours and the instantaneous streamlines over pitching and plunging 2D and 3D (= 2, 75% span) flat plates at = 0.25, =0.04, and at = 4×10^4 from the computations.

Figure 4-13 illustrates the contours from the 2D and the 3D computations for pitching and plunging kinematics. Whereas the flow field was dominated by large leading-edge separation due to the geometric effects in the downstroke as discussed in Section 4.4 in 2D, in 3D the separation is mitigated and the flow reattaches before the mid-chord. The velocity field at the center of the downstroke, = 0.25 is further depicted in Figure 4-14 from the 3D computation and experimental measurements at 75% span location. The agreement from both methods is good. At the leading edge the boundary layer separates, but the flow reattaches around = 0.25.

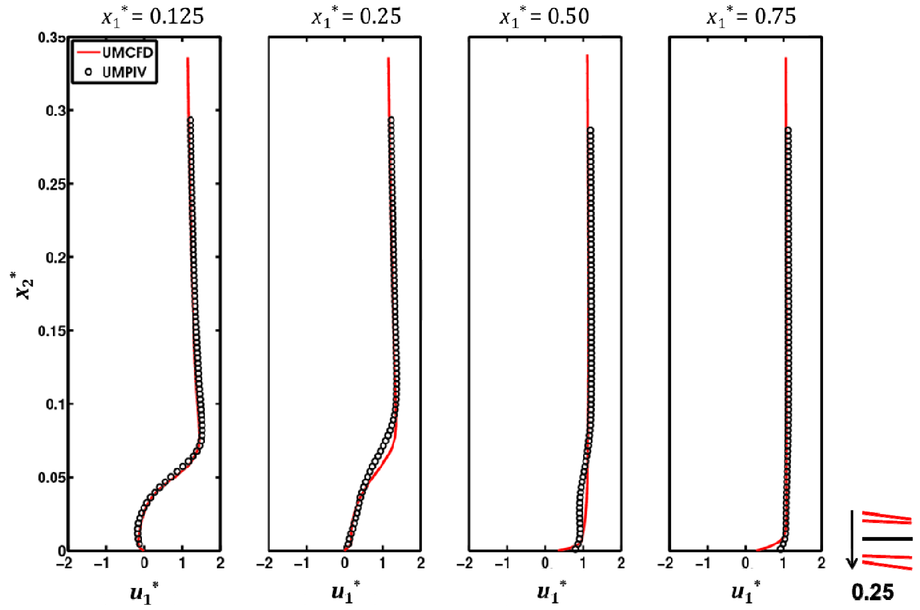

Figure 4-14 profiles from the numerical and experimental results at constant = 0.125, 0.25, 0.50, and 0.75 at = 0.20 at = 4×10^4, = 0.25, = 0.04 for the pitching and plunging 3D flat plate with = 2 at 75% span.

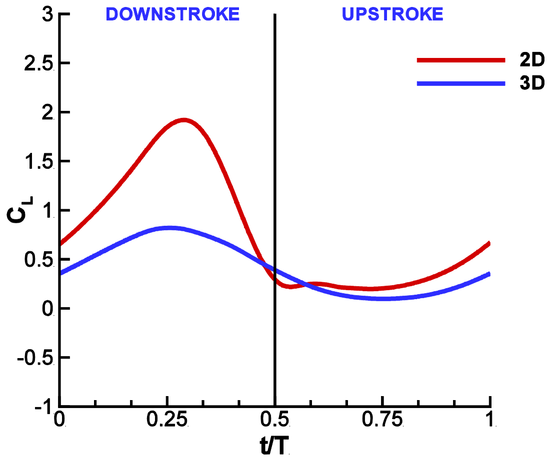

Figure 4-15 Lift coefficient as function of non-dimensional time for pitching and plunging 2D and 3D (= 2) flat plates at = 0.25, =0.04 and = 4×10^4.

The absence of the strong leading edge separation for the low aspect ratio flat plate with = 2 manifests itself in the aerodynamic force felt on the wing. The time history of the lift coefficient for both 2D and 3D pitching and plunging flat plates are plotted in Figure 4-15. In the upstroke where both flat plates evince attached boundary layer, the lift coefficient shows comparable magnitudes. However, during the downstroke the lift generated on the 2D flat plate is 2.3 times greater than its 3D counterpart.

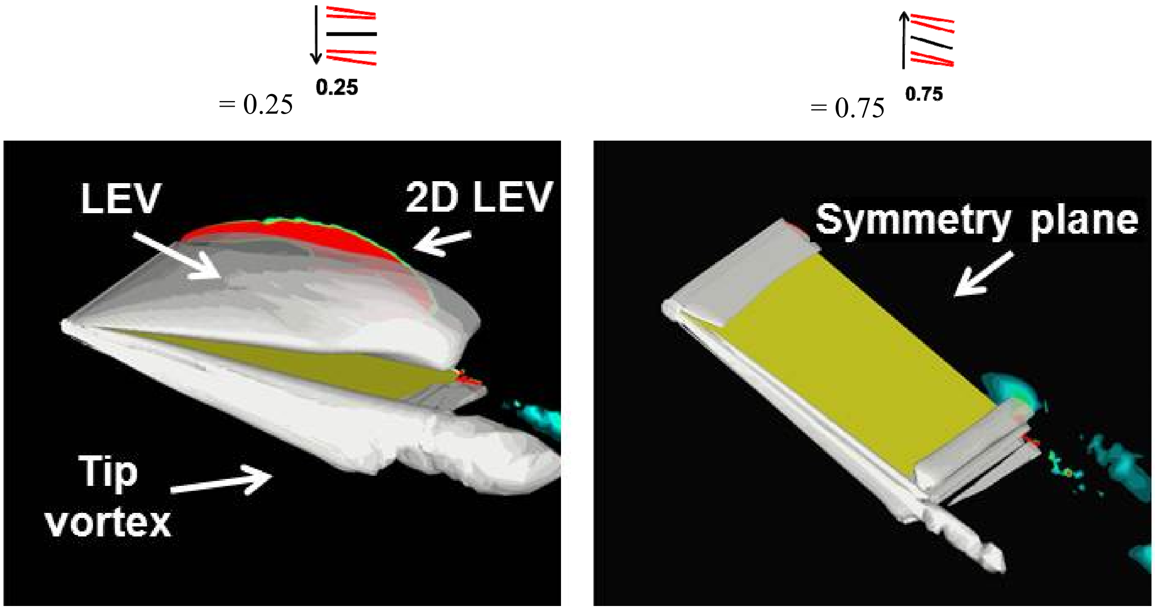

(a) iso-Q-surface at = 4 (white) and Q contours from the 2D computations on the symmetry plane.

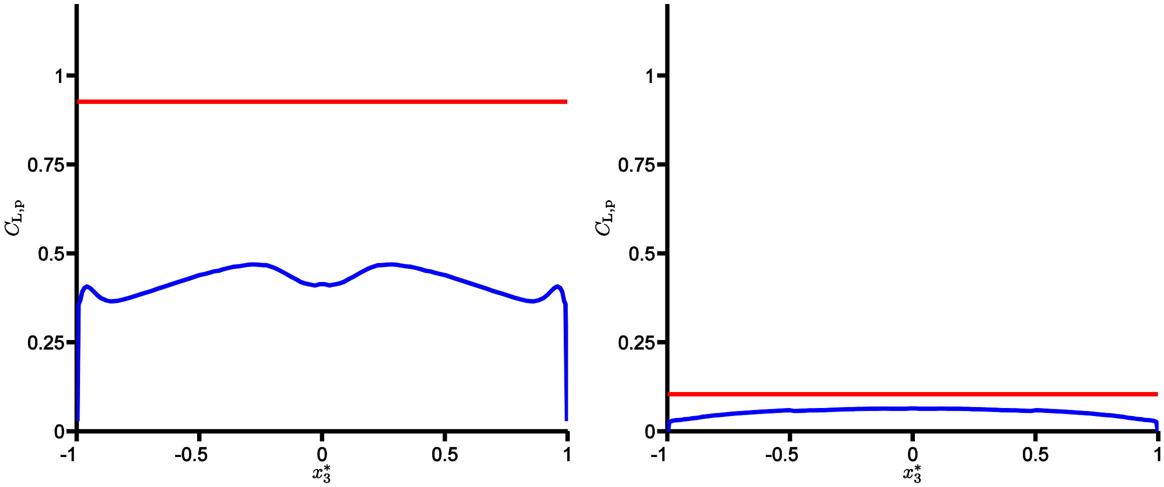

(b) spanwise lift distribution due to pressure. Red: 2D; Blue: 3D.

Figure 4-16 Q surfaces (a) and spanwise lift distribution (b) to illustrate the difference in the flow structures at the center of the downstroke (= 0.25) and the center of upstroke (= 0.25).

At the center of the downstroke, = 0.25, the effective angle of attack is at maximum, see Figure 4-2, and the development of the TiV is also significant as illustrated in Figure 4-16(a). This TiV interacts with the LEV developed at the leading edge of that flat plate. Because of the downwash induced from the presence of TiV, the effective angle of attack at the leading edge is smaller than in 2D, which results in weaker LEV. This has the consequence that the spanwise lift distribution in 3D is smaller than in 2D as shown in Figure 4-16(b). On the other hand, at the center of downstroke the effective angle of attack is at minimum and the flow field has negligible 3D effects.

4.7 Summary

For high Reynolds number and low reduced frequency flow the interplay between the imposed kinematics, the airfoil shape, the Reynolds number, and dimensionality is examined for two airfoils: a SD7003 airfoil, and a two-dimensional flat plate with 2.3% thickness undergoing two sets of wing kinematics (i.e., pitching and plunging, and pure plunging) at Re range from 1×10^4 to 6×10^4, k of 0.25 and St of 0.04. The airfoil shape plays an important role in determining the flow features generated by the pitching and plunging, and pure plunging kinematics. Due to the larger leading edge radius of the SD7003 airfoil, the effects of Reynolds number are obviously observed. For pitching and plunging case, more attached flow feature are present at higher Re, whereas flow separations from the leading edge were observed at lower Re. For pure plunging case a leading edge separation is seen at all Reynolds numbers. In 3D the presence of TiV mitigates the LEV generation resulting in smaller lift magnitude during the downstroke of a pitching and plunging flat plate at $Re = 6\times10^4$. During the upstroke where the TiV is small, the flow field and the force felt on the wing were comparable to its 2D counterpart. Furthermore, it is found that two-dimensional RANS computations with the Menter's original and modified SST turbulence models provided qualitatively, and quantitatively - depending on the flow conditions - good predictions in terms of velocity fields compared to two-dimensional phase-averaged PIV data in the water channel from two different facilities.

Chapter 5.

Effects of Flexibility on the Fluid Dynamic Performance of Wings

5.1 Introduction

In this chapter the effects of flexibility on the fluid dynamic performances, i.e. propulsive force generation and the propulsive efficiency, are considered. The findings reported in the literature can be summarized by the following two observations, see also Section 1.2.5:

(i) Maximum propulsive force is generated when the wing motion frequency is near the natural frequency of the wing [45,82,68,69,72,83].

(ii) Optimal propulsive efficiency is obtained at a motion frequency that is only a fraction of the natural frequency [86,82,68,69].

To probe and to elucidate the mechanisms related to these observations, first three canonical cases with sinusoidal kinematics will be considered to assess the role of the chordwise flexibility, spanwise flexibility, and isotropic wings on the resulting fluid dynamic forces: i) thrust generation of a purely plunging chordwise flexible airfoils in water in forward flight at $Re = 9.0 \times 10^3$, studied experimentally by Heathcote and Gursul [73] and numerically for one particular motion frequency by Shyy *et al*. [6]. The airfoil consists of rigid teardrop leading edge with elastic flat plate as tail. In this study five flat plate thicknesses will be considered for various motion frequencies with resulting thrust; ii) thrust generation of a purely plunging spanwise flexible wing with NACA0012 airfoil in water in forward flight at $Re = 3.0 \times 10^4$ considered by Heathcote, Wang, and Gursul [76], Chimakurthi *et al*. [77], and Shyy *et al*. [6]. Two different wing materials will be used to evaluate the wing flexibility effects on the resulting thrust for a range of motion parameters; iii) lift generation of flapping isotropic Zimmerman wing hovering in air at $Re = 1.5 \times 10^3$ and $k = 0.56$ where the Young's modulus and the mass of the wing are varied to assess the effects of the structural properties on the resulting lift. Altough a wing with the same geometry is preferred to study the effects of the chordwise and the spanwise flexibilities independently, the first two cases studied in this dissertation are chosen, because of the experimental results [73] [76] are well documented for validation purposes. The design space of the third case is based on several choices of the wing material and fluids that are used in wind/water tunnel experiments as well as Micro Air Vehicle (MAV) applications. Based on these canonical cases, the underlying physical mechanism will be identified and a scaling parameter for the force generation and the propulsive efficiency of flexible oscillating wings will be proposed that depends on the *a priori* known non-dimensional parameters. Identifying this scaling parameter leads to an order of magnitude estimation of the flexilibity enhanced fluid dynamic performance. Furthermore, the scaling parameter will be extrapolated to the case of insects by assuming that the weight of the insects are sustained by the lift and it will be shown that the lift generated also follows the same scaling. Finally, scaling for the propulsive efficiency will be presented that sheds light on the two observations mentioned at the beginning of this section.

5.2 Propulsive Force Generation of Oscillating Flexible Wings

5.2.1 Purely Plunging Chordwise Flexible Airfoils in Forward Flight in Water

To explore the thrust enhancement induced by chordwise flexibility, the thrust of a purely plunging chordwise flexible airfoil is computed for different thickness ratios (h_s^* = 4.23×10^{-3}, 1.41×10^{-3}, 1.13×10^{-3}, 0.85×10^{-3}, and 0.56×10^{-3}) and motion frequencies that produce Strouhal numbers between St = 0.085 and 0.3 with 0.025 increment with the plunge amplitude kept fixed to $h_\mathrm{a}/c_\mathrm{m}$ = 0.194. The reduced frequency k varies then between 1.4 and 4.86. As shown in Table 2-1 variation in the thickness changes Π_1, whereas the motion frequency affects both the reduced frequency and the Strouhal number. The airfoil consists of a rigid teardrop leading edge and an elastic plate that plunges sinusoidally in freestream. Detailed experimental setup and discussion of fluid physics is in Ref. [73], and Shyy *et al.* [6] obtained a numerical solution for St = 0.17 for different thickness ratios. An Euler-Bernoulli beam solver is used to solve Eq. (2) for the deformation of the elastic flat plate, while the rigid teardrop moves with the imposed kinematics. Furthermore, the Reynolds number Re = 9.0×10^3 and the density ratio ρ^* = 7.8 are held constant in all cases. The grid and time step sensitivity studies are shown in Appendix A.3.

To validate the current computation to the experimental measurements [73] the trailing edge motion is plotted as function of t/T for the moderate thick h_s^* = 1.41×10^{-3} and the thinnest h_s^* = 0.56×10^{-3} cases at St = 0.17 in Figure 5-1. For the thinnest airfoil the displacement peak in the downstroke near t/T = 0.25 is slightly overpredicted, however the overall trend matches well. At St = 0.17 the thinnest airfoil deformes considerably more than the airfoil with h_s^* = 1.41×10^{-3} with larger phase lag.

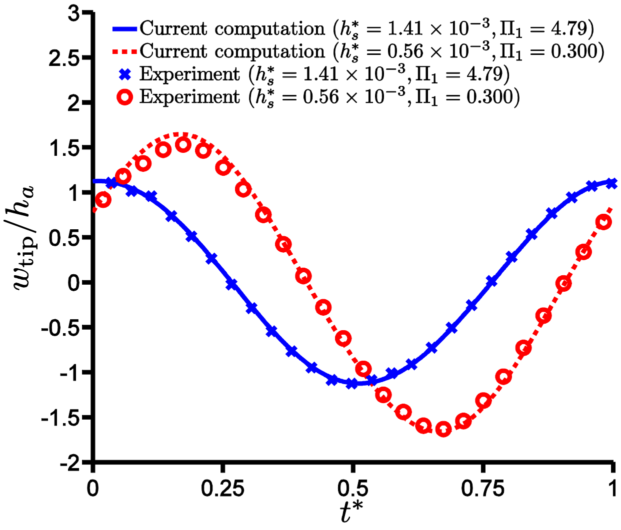

Figure 5-1 Trailing edge displacement as function of non-dimensional time for the purely plunging chordwise flexible airfoils in water in freestream at Re = 9.0×10^3 with h_s^* = 1.41×10^{-3} and 0.56×10^{-3} at St = 0.17. The experimental measurements are from [73].

For St = 0.17 the thrust coefficient as a function of normalized time (with respect to the period of plunge) for the *Rigid* (h_s^* = 4.23×10^{-3}) *Flexible* (h_s^* = 1.41×10^{-3}), and *Very Flexible* (h_s^* = 0.56×10^{-3}) thickness ratios is shown in Figure 5-2. In order to estimate the individual contribution of the teardrop and the flexible plate to force generation, the time histories of thrust coefficient are shown in Figure 5-2 separately for each element. It is seen that the thrust response with variation in flexibility is different in each of the two cases: with increasing chordwise flexibility of the plate the instantaneous thrust contributed by the flexible plate increases. One of the mechanisms found in Ref. [6] is that the chordwise deformation of the rear flexible plate in both *Flexible* and *Very Flexible* cases result in an effective projected area for the thrust forces to develop.

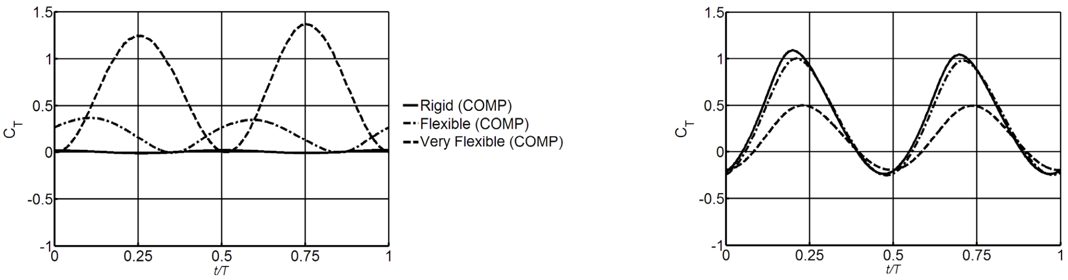

(a) C_T generated by the rigid teardrop (b) C_T generated by the flexible flat plate

Figure 5-2 Time histories of thrust coefficient contribution due to the teardrop and the flexible plate separately at St = 0.17: (a) response of the teardrop; (b) response of the flexible plate. Extracted from [6].

The interplay between the motion frequency indicated with Strouhal number and the resulting thrust and wing tip displacement is further illustrated in Figure 5-3. For the Flexible airfoil the resulting thrust generation increases with the increased motion frequency (Strouhal number and reduced frequency) and the maximum wing tip displacement also shows monotonic increase with the motion frequency. A striking observation is that the vorticity field looks similar for all Strouhal numbers shown, however the pressure contours and also the resulting thrust time histories differ in values. This could be related to the scaling proposed in Chapter 3 that the force acting on a moving body is largely dominated by the motion of the airfoil and less with the vorticity in the flow field at high reduced frequencies. Similar trend is shown for the *Very Flexible* airfoil with the thickness ratio about 2.5 times smaller than for the *Flexible* airfoil cases. The thrust increases with higher St and k, however the maximum tip amplitude saturates for St = 0.15, 0.25, and 0.4. Instead of resulting in a larger tip amplitude motion, higher motion frequency leads to larger phase lag of the wing tip relative to the wing root.

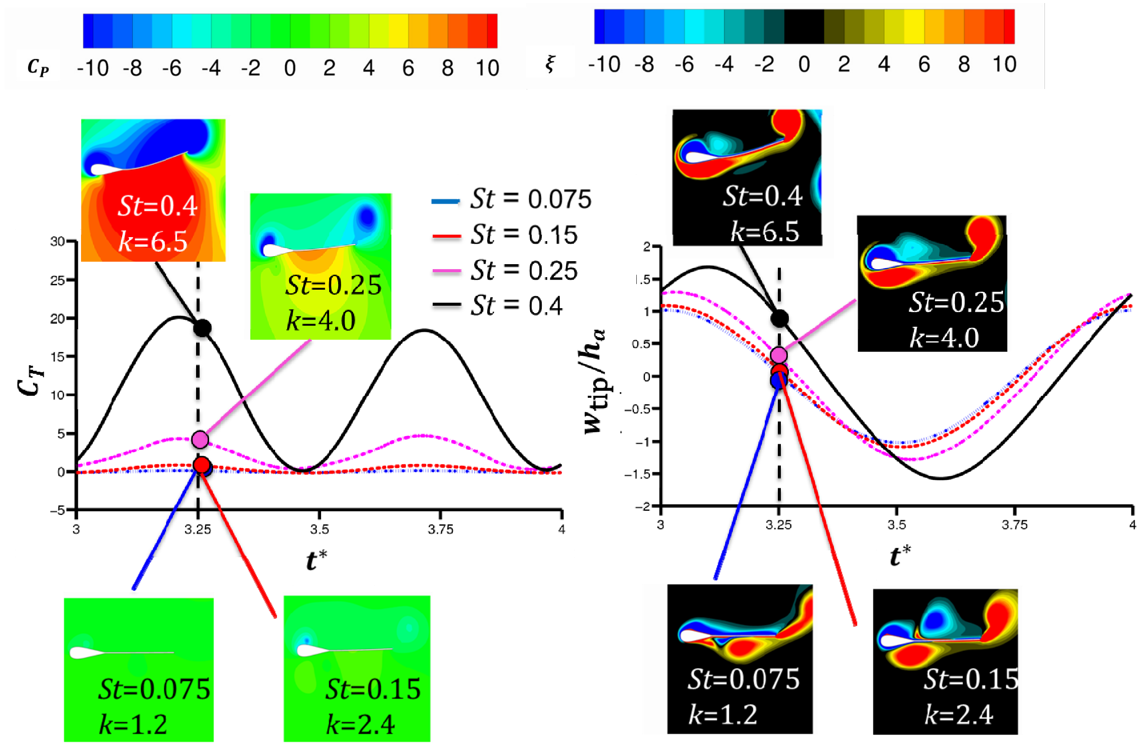

(a) Flexible (= 1.41×10^{-3})

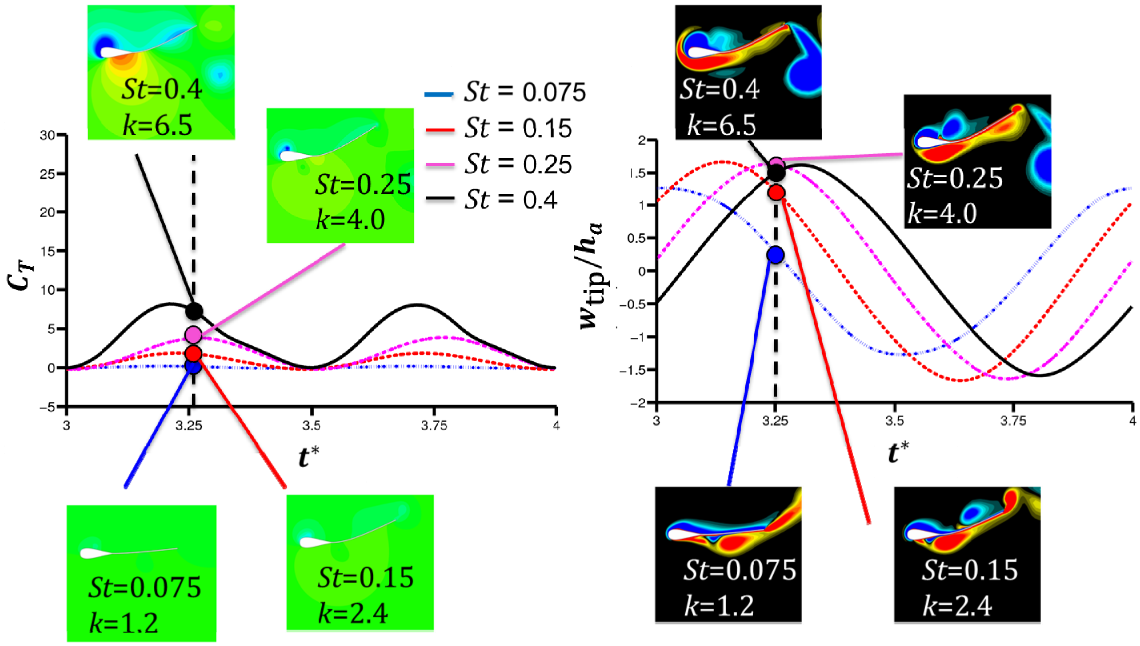

(b) Very Flexible (= 0.56×10^{-3})

Figure 5-3 Time histories of thrust and wing tip displacement normalized by the plunge amplitude as function of non-dimensional time. Pressure coefficient and vorticity contours at = 0.25 for each Strouhal number are shown as well.

Increasing motion frequency leads to higher acceleration of the wing, and hence greater force generation. However, eventually the fluid dynamics time scale and response become limiting factors, as it will be discussed in Sections 5.2.4 and 5.3.

Figure 5-4 shows the time-averaged thrust coefficient for a range of motion frequencies from the current numerical computation and the experimental measurements [73]. For the thickest flat plate (h_s^* = 4.23×10^{-3}) the computed thrust compares well with the experimental measurements. At the higher motion frequencies, St = 0.28 and 0.3, the computed thrust starts to deviate. Similar trend is observed for the other thicknesses: at h_s^* = 0.85×10^{-3} the correlation between the numerical result and the experimental measurement is good until St = 0.23 and at h_s^* = 0.56×10^{-3} only at the lowest frequencies. Modeling uncertainties, such as laminar-to-turbulent transitions, nonlinearities in the structural modeling at large or nonnegligible twist or spanwise bending in the experimental setup, which are not accounted for in the numerical computations may be attributed to the observed differences.

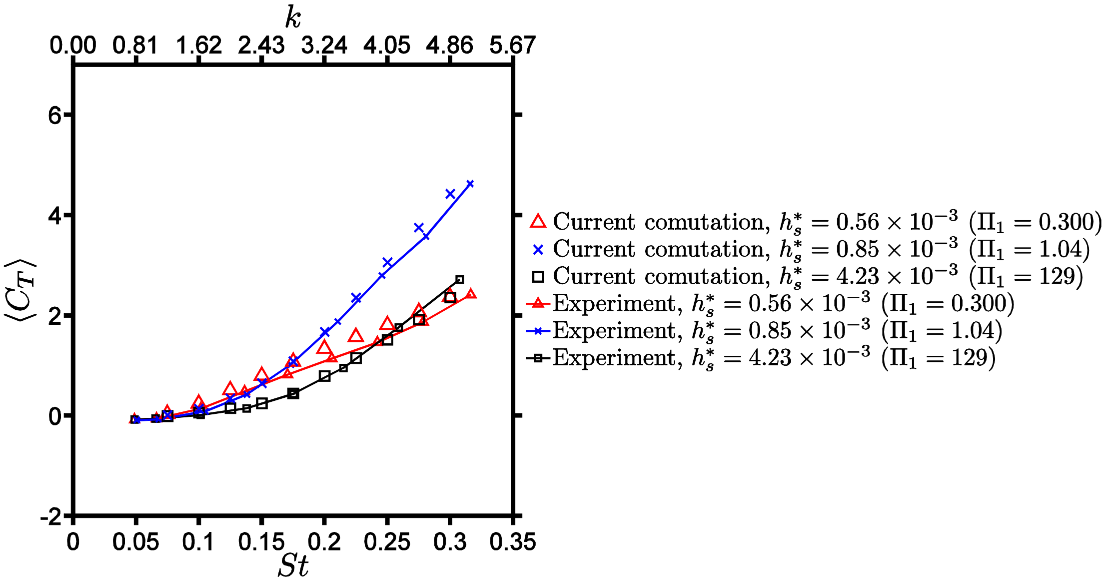

Figure 5-4 Time-averaged thrust coefficient for a plunging chordwise flexible airfoil at Re = 9.0×10^3 and ρ^* =7.8 for different flat plate thickness and motion frequencies. The experimental data are extracted from [73]. The symbols on the line indicate the discrete dataset from the experimental measurements.

The thrust for the thickest airfoil (h_s^* = 4.23×10^{-3}) can be enhanced by increasing the motion frequency that results to higher St and k. Increased St leads to greater fluid dynamic force, but also greater acceleration-reaction force. Furthermore, as the acceleration-reaction force depends on the acceleration and the chord of the wing, see Eq. (36), higher k will increase the acceleration-reaction force further. Figure 5-4 also shows that the thrust generation depends on the thickness of the wing: At St = 0.125, $\langle C_T \rangle$ for h_s^* = 0.56×10^{-3} is the maximum; however, for higher Strouhal numbers the thrust generated by the thinnest airfoil is the lowest: at St = 0.3, h_s^* = 0.85×10^{-3} generates the highest thrust, while the thinnest wing, h_s^* = 0.56×10^{-3}, deteriorate in thrust.

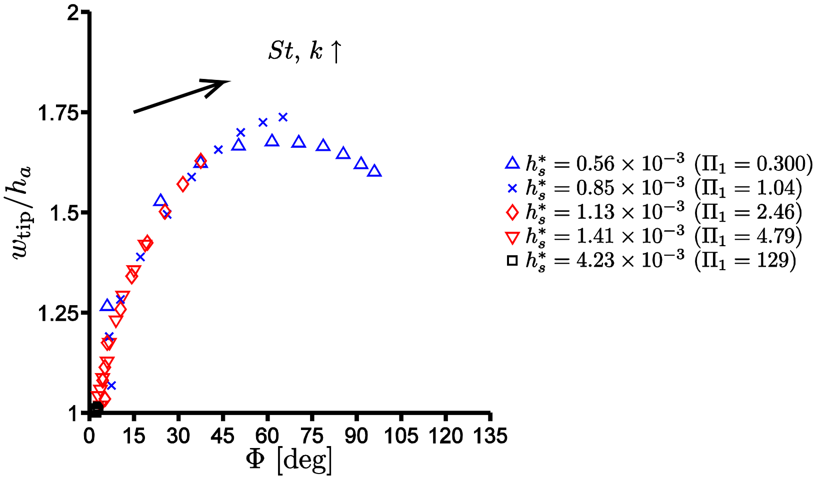

(a) Tip displacement

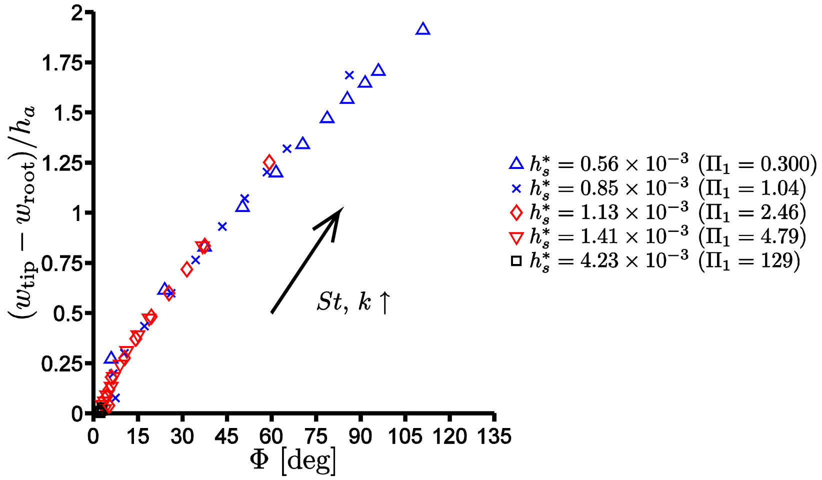

(b) Relative tip deformation

Figure 5-5 Tip deformations of a plunging chordwise flexible airfoil at Re = 9.0×103 and ρ^* =7.8 for different flat plate thickness and motion frequencies.

To characterize the structural response, the tip displacement normalized to the plunge amplitude, w_{tip}/h_a, is plotted in Figure 5-5 as function of the phase lag relative to the leading edge for the thicknesses and frequencies considered. The phase lag Φ is calculated by determining the time instant at which the trailing edge displacement is a maximum. For the thickest airfoil, $h_s^* = 4.23\times10^{-3}$, both the deformations and the phase lag are small. As we decrease the the airfoil thickness, both w_{tip}/h_a and Φ increase with increasing frequency, see figure 2. Eventually, w_{tip}/h_a saturates when Φ approaches 90 deg: when $\Phi > 90$ deg the motion of the deformed trailing edge is out of phase with the imposed leading edge. Relative to the leading edge displacement, $(w_{\mathrm{tip}} - w_{\mathrm{root}})/h_a$ shows that by decreasing the stiffness and increasing the motion frequency not only the tip deformation increases monotonically, but also the phase lag, so that the resulting wing tip displacement reduces in magnitude when the motion is out of phase (Figure 5-5). In Section 5.2.4 a relationship between the mean thrust and the structural response will be established.

5.2.2 Purely Plunging Spanwise Flexible Wings in Forward Flight in Water

The effects of spanwise flexibility on thrust generation of a three-dimensional rectangular wing oscillating in pure plunge in forward flight have been investigated with water tunnel experiments [76] and numerical simulations [77] [6] [95]. The wing models of $R = 0.3$ m semi-span and $c_{\mathrm{m}} = 0.1$ m chord length with several spanwise flexibilities were considered. More detailed information of experimental case setup can be obtained in Ref. [76]. In this dissertation, two combinations of density ratio and effective stiffnesses and several motion frequencies at $Re = 3.0\times10^4$ are considered to compare the results with available experimental and computational results, to highlight the thrust enhancement mechanism associated with spanwise flexible plunging wings in forward flight. The grid and time step sensitivity studies are shown in Appendix A.4.

The vertical displacements of the wing tip from the computations and the experiments for the *Flexible* and *Very Flexible* wings are shown in Figure 5-6. The displacement is normalized with respect to the amplitude of prescribed wing root movement. For the *Flexible* wing, in comparison to the tip response presented in previous studies (experiment: [76]; implicit Large Eddy Simulation (LES) computation [95]), the tip response of current computation shows good correlation. For the *Very Flexible* wing, however, the tip response of the current computation exhibits slight larger amplitude and phase advance compared to the measurements [76].

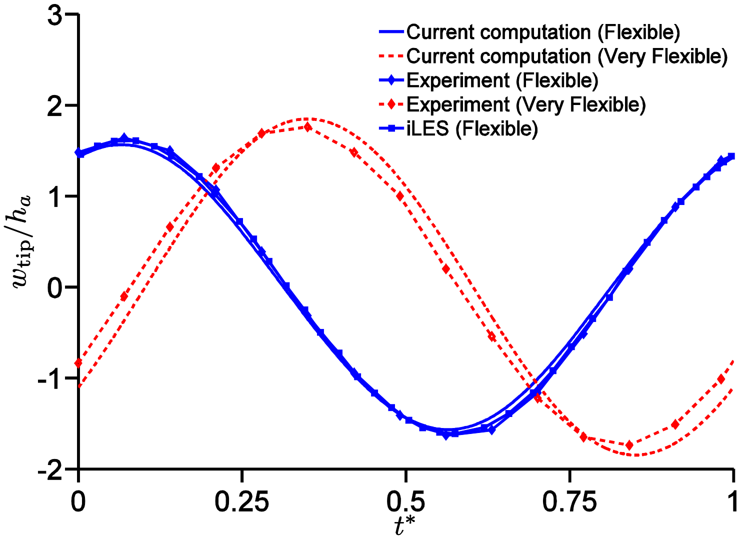

Figure 5-6 Time history of tip displacements of a plunging spanwise flexible wing at *Re* = 3.0×10^4 for different wing stiffness, wing density, and motion frequencies. The experimental data are extracted from Ref. [76] and the implicit LES from [95].

Time histories of thrust coefficient for the *Flexible* and *Very Flexible* wings are shown in Figure 5-7. For the *Flexible* wing the thrust in the current computation is underpredicted and has some phase advance compared to the measurements [76]. However, the agreement in terms of the magnitude and the timing of thrust peaks compares well with the thrust prediction using the iLES [95] coupled with a geometrically nonlinear beam solver. Furthermore, the measured thrust is assymetric in the donwstroke and upstroke while in both computations the thrust has symmetric behaviour. For the *Very Flexible* wing, the computed thrust history is in a reasonable agreement with the experimental measurements in terms of the amplitude and the trend of thrust. It is worth to point out that the measurements include higher frequency components, while the waveforms of the computed thrust are smooth for all cases. As shown in Figure 5-6, there is no evidence of high frequency behaviour in the tip response. The experimental flow field measurements [76] also do not indicate flow features that may be attributed to these high frequency contents. Therefore this difference may have risen from uncertainties in the experimental setup or in the computational modelling. To further quantify these uncertainties comparisons of instantaneous three-dimensional wing shapes and flowfields near the leading-edge are recommended between the experiments and computations. Furthermore, more detailed documentation of the torsion and the natural frequencies measurements of the wing would be helpful for computational modeling.

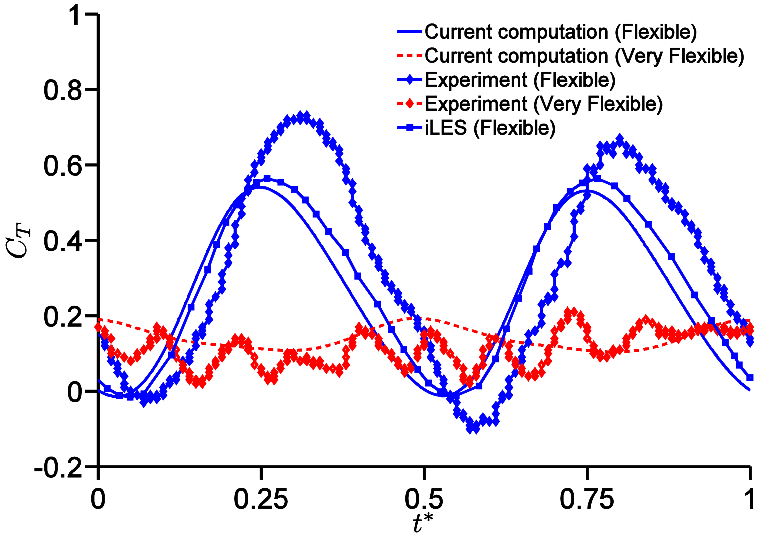

Figure 5-7 Time history of thrust coefficient of a plunging spanwise flexible wing at $Re = 3.0\times10^4$ for different wing stiffness, wing density, and motion frequencies. The experimental data are extracted from Ref. [76] and the implicit LES from [95].

Vorticity and pressure contours for the *Flexible* and the *Very Flexible* configurations at the mid-span section at time instant $t^* = 0.25$, when the wing is at the center of downstroke, are shown in Figure 5-8. The dominance of leading edge suction in the *Flexible* case and the reduction of it in the *Very Flexible* case are visible in that figure. The phase lag between the prescribed motion and the deformation of the wing is could be used to explain the thrust generation in flexible flapping wings [6]. For the Very Flexible case the cross sectional motion is in the opposite direction of the imposed kinematics at the wing root. The phase lag at the wing tip with respect to the prescribed motion for the *Flexible* and *Very Flexible* cases are, -26 deg, and -126 deg, respectively. As a result of the substantial phase lag in the *Very Flexible* case, the wing tip and root move in opposite directions during most of the stroke resulting in lower effective angles of attack and consequently lesser aerodynamic force generation, see also the direction of the arrow in the contour plots that denotes the direction of the wing motion.

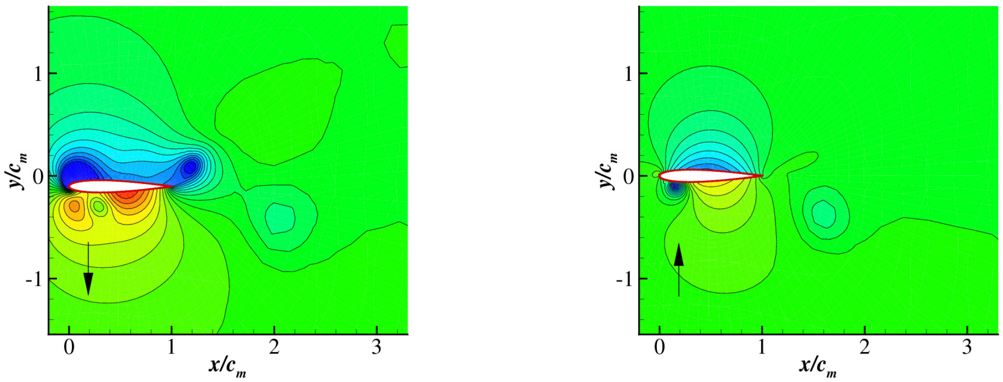

(a) pressure coefficient contour levels: 2; range: -2.5 to 2.5

h_s^* = 0.01, St = 0.1, k = 1.82, t^* = 2.25

(left) Π_1 = 212, ρ^* = 7.8; (right) Π_1 = 38, ρ^* = 2.7

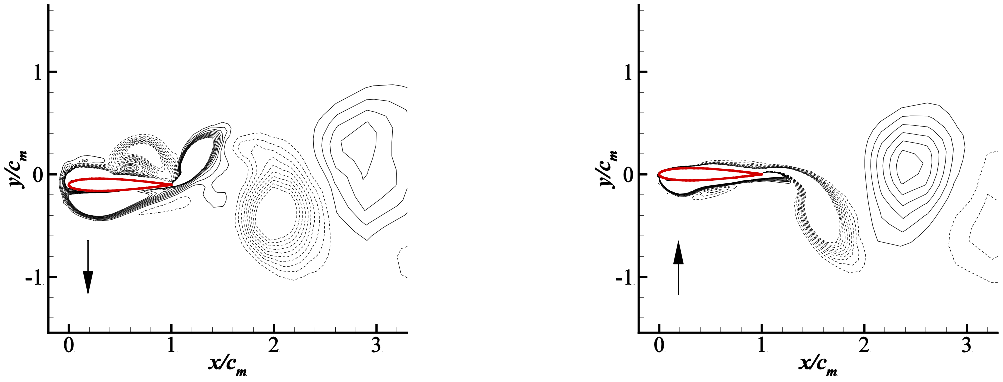

(b) vorticity contour levels: 20; range: -3 to 3

h_s^* = 0.01, St = 0.1, k = 1.82, t^* = 2.25

(left) Π_1 = 212, ρ^* = 7.8; (right) Π_1 = 38, ρ^* = 2.7

Figure 5-8 Pressure coefficient $(p - p_\infty)/(\frac{1}{2}\rho_f U_{\mathrm{ref}}^2)$ and vorticity contours at 75% span location for *Flexible* and *Very Flexible* configurations. The arrow indicates the direction of the airfoil motion.

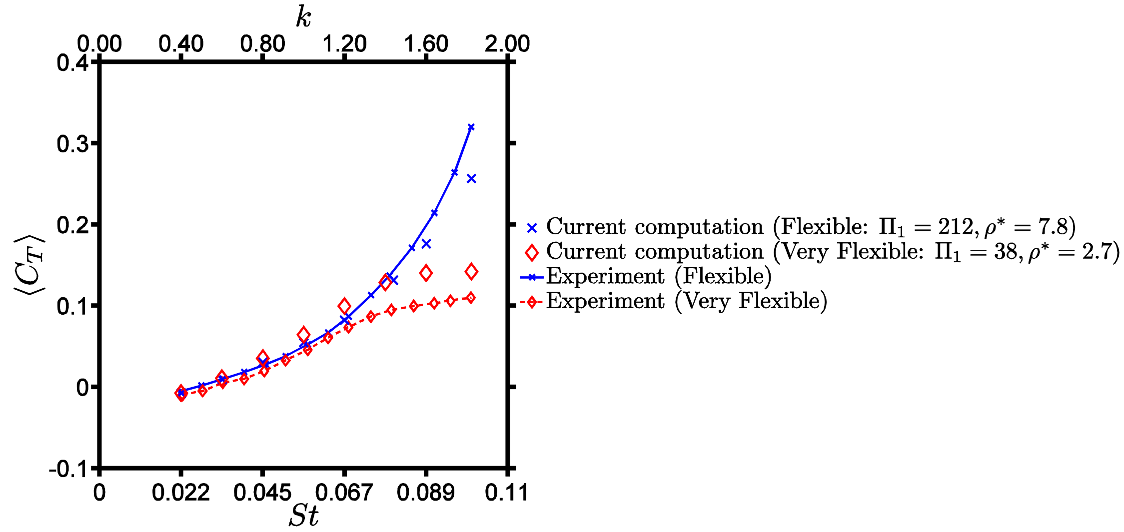

Figure 5-9 Time-averaged thrust coefficient of a plunging spanwise flexible wing at $Re = 3.0\times10^4$ for different wing stiffness, wing density, and motion frequencies. The experimental data are extracted from Ref. [76]. The symbols on the line indicate the discrete dataset from the experimental measurements.

The structural response is depicted in Figure 5-10. For the *Flexible* wing, the phase lag between the prescribed motion and the tip response for $k > 1.4$ is from 17.6 deg to 23.8 deg, whereas for the *Very Flexible* wing, Φ varies from 108.8 deg to 125.9 deg, see Figure 5-9. The wing tip of the *Very Flexible* wing moves in opposite direction as the root for the most of the stroke for higher motion frequencies, while for the *Flexible* wing, the wing root and the tip are in phase. This is confirmed in Figure 5-10 where all *Flexible* wing cases show a phase lag of the wing tip relative to the wing root, Φ, less than 90 deg, while for k = 1.6 and k = 1.82 Φ > 90 deg for the *Very Flexible* wing. Again, the correlations of the dynamics from the root to tip play a key role for the tip displacement as shown in Figure 5-10, where the relative tip displacement is shown to be monotonic to Φ. Moreover, the relationship between the time-averaged thrust and the relative tip displacement is discussed in Section 5.2.4.

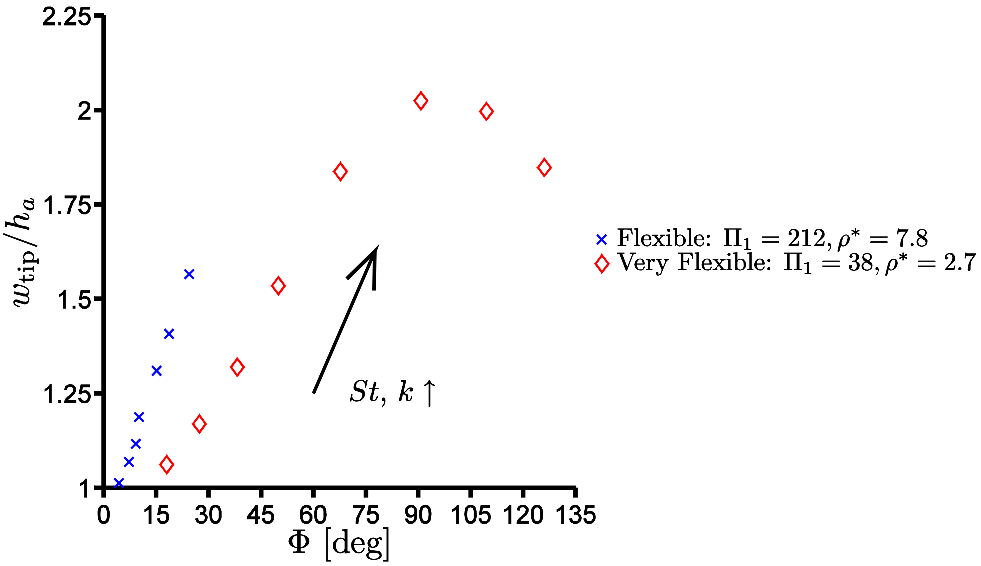

(a) Tip displacement

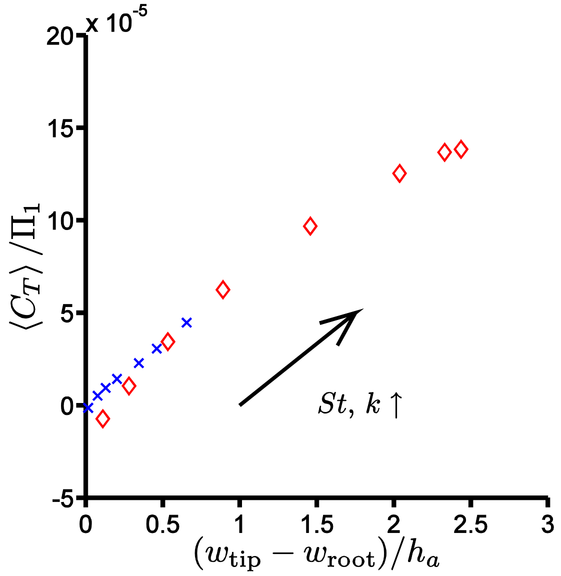

(b) Relative tip deformation

Figure 5-10 Tip deformations of a plunging spanwise flexible wing at *Re* = 9.0×10^3 for different wing stiffness, wing density, and motion frequencies.

5.2.3 Lift Generation of a Hovering Isotropic Flapping Zimmerman Wing in Air

The previous two cases were proposed by Heathcote and Gursul [73] and Heathcote *et al.* [76] to assess the effects of chordwise and spanwise flexibilities, respectively, on the thrust generation of plunging wing in forward flight at low density ratio. Motivated by the experimental studies on the three-dimensional Zimmerman wing planform [71], a three-dimensional hovering flapping isotropic wing in air is considered. The wing is a flat plate wing of c_{m} = 0.0196 m and R = 3.825 with a thickness ratio of h_s^* = 2.0×10^{-2} having a Zimmerman planform, see Figure 5-11, hovering in air at Re = 1.5×10^3. A sinusoidal flapping motion is introduced at the rigid triangle at the leading edge at the wing root following, Eq. (3) with St = 0.25 and k = 0.56. The flapping axis is parallel to the wing root. Note that in the axes definition by Wu *et al*. [6] the wing flaps up-and-down to generate thrust due to wing flexibility, however in the current study the flapping wing axis has been rotated so that the flapping axis is parallel to the lift direction, such that the any flexibility in the wing leads to lift generation. The triangular rigid region near the root at the leading edge undergoes prescribed motion and is constrained in all degrees of freedom in the structural solver, since the flapping mechanism in the experiment [137] is actuated at this region on the wing. The grid and time step sensitivity studies are shown in Appendix A.5.

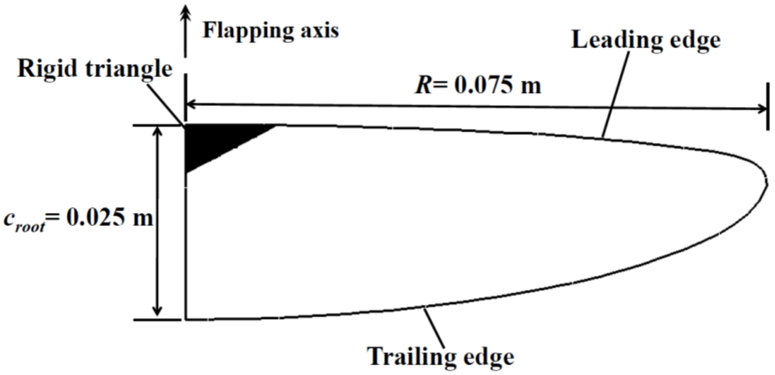

Figure 5-11 Geometry of the Zimmerman planform.

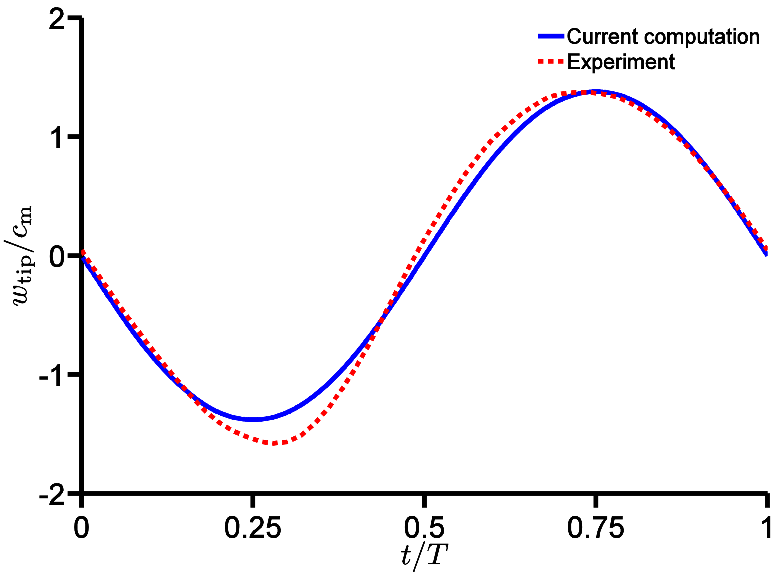

Figure 5-12 Time histories of horizontal displacement at the wing tip of an isotropic flapping Zimmerman wing hovering at Re = 1.5×10^3, k = 0.56, and St = 0.25, made of aluminum.

To validate the numerical computation the Zimmerman wing made of aluminum is compared to the available experimental data [137] in terms of the wing tip displacement in horizontal direction in Figure 5-12. The predicted tip response shows reasonable agreement with the measured displacement and captures the main qualitative trends of the response of wing tip. The current computation exhibits a more symmetric response between the downstroke and the upstroke in comparison to the experimental measurements. The reason for the asymmetry in the measurements might be due to uncertainties in the experimental setup related to the driving system of the flapping device, or cycle-to-cycle variations in the measurements.

To assess the effects of different wing properties: the effective stiffness Π_1 and the density ratio ρ^*, on the resulting lift and wing deformations, surrogate models are constructed to qualitatively explore their implications. Surrogate models offer methods to efficiently organize the data measured as objective functions and give global and reliable qualitative trend as function of design variables [128]. The range for these variables in the design space is chosen to cover wide range of applications as shown in Table 5-1. To effectively assess the order of magnitude of the design variables a logarithmic scaled design space will be populated.

Table 5-1. Range of the design variables $\boldsymbol{\Pi_1}$ and $\boldsymbol{\rho^*}$ with representative examples.

Parameter	Minimum	Maximum
Π_1	1.0×10^2 (HDPE, polyethylene in air)	1.0×10^5 (steel, aluminum in air)
ρ^*	1.0×10^1 (water to steel, aluminum)	1.0×10^4 (air to steel, aluminum)

The objective functions are (a) the lift coefficient averaged over one motion cycle between the second and the third cycle, i.e. $m = 2.5$ in Eq. (7), (b) the twist angle θ given as

$$\theta = \max\{\mathrm{acos}(\boldsymbol{c}_3 \cdot \boldsymbol{e}_1)\}. \tag{41}$$

where $\boldsymbol{c}_3$ is the unit vector in the direction from the leading edge to the trailing edge at the section 3 of the wing (see Section A.5) and $\boldsymbol{e}_1$ is the unit vector in the lift direction. So θ gives the degree of the lift favorable projectional area of the wing due to deformation, and (c) the bending angle ψ that is defined as

$$\psi = \max\left\{\mathrm{atan}\left(\frac{w}{R}\right) - \phi\right\}. \tag{42}$$

to measure the wing deformation in spanwise direction x as the maximum tip displacement angle relative to the imposed flap angle ϕ. For simplicity lift will be referred as the time-averaged lift coefficient from now on.

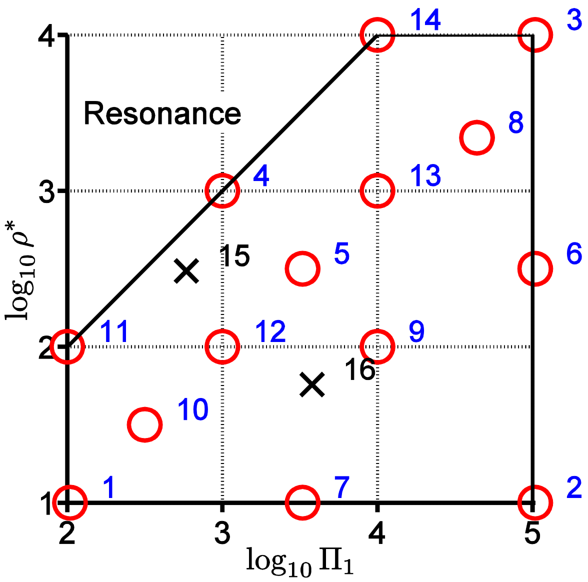

Figure 5-13 Design of experiment in logarithmic scale for the design variables Π_1 and ρ^*. The training points are indicated by cicles and the training points by crosses.

The design of experiments use a face centered cubic design (FCCD) and then the remainder of the design space is filled evenly in the design space with the cases 8 and 10 together with the testing points are generated by the Latin Hypercube Algorithm. In total 14 training points are selected. A tabulation of the training points are found in Table B-1. The design space with logarithmic bias towards the softer Π_1 and lighter ρ^* structures are shown in Figure 5-13. The region where $\log_{10}\rho^* > \log_{10}\Pi_1 + 2$ is out of the scope of the current study as this region showed largely unstable behaviour of the wing motion because the imposed frequency of 10 Hz is close to the natural frequencies, see Appendix C.

The resulting surrogate models are shown in Figure 5-14 for the lift, twist, and bending angle. Notice that the time-averaged lift for the rigid wing would be zero due to the symmetry in the hovering kinematics without pitching motion. The lift, twist, and bending are at the maximum at the case 4 and these three objective functions have qualitatively similar trend in the design space suggesting that there exists a correlation between the resulting time-averaged lift force and the maximum deformations. Furthermore, it is not only the effective stiffness Π_1, or the density ratio ρ^*, but the balance between these two parameters that determine the resulting deformation and the lift generation. The region of increased objective functions between $\log_{10}\Pi_1$ = 4 and 5 and $\log_{10}\rho^*$ = 1 to 2 is caused by the error in surrogate model due to high gradient near the resonance region, yet wide region of almost zero values at more stiffer and lighter portion of the design space.

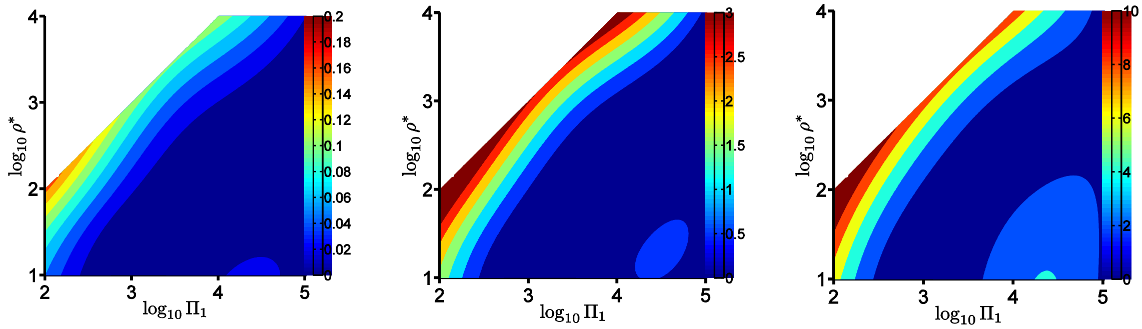

(a) $\langle C_L \rangle$ (a) θ (a) ψ

Figure 5-14 Surrogate model responses for (a) lift, (b) twist, and (c) bending angles for a flapping isotropic Zimmerman wing at $Re = 1.5\times10^3$ and k = 0.56.

As the sinusoidal rigid-body motion is imposed at the triangular rigid part near the wing root (see Figure 5-11), the wing inertia and the resulting aerodynamic load are balanced out by the elastic force. Since the wing is made of isotropic material the structure will respond in both spanwise bending as well as twisting.

For the chordwise flexible airfoil in Section 5.2.1 and spanwise flexible wing in Section 5.2.2 the thrust generation in forward flight was shown to be dominantly dependent on the resulting tip motion relative to the imposed kinematics at the wing root. For the flapping Zimmerman wing in hover in air, maximum horizontal tip displacement w normalized by the prescribed amplitude $h_a = R\sin\phi_a$ is plotted against the phase lag with respect to the top of the stroke of the rigid body motion in Figure 5-15. The higher tip amplitude corresponds with larger phase lag compared to the imposed kinematics, while the tip motion is in phase. The cases with the highest Π_1/ρ^* ratio have larger deformation consistent with the surrogate model responses shown in Figure 5-14.

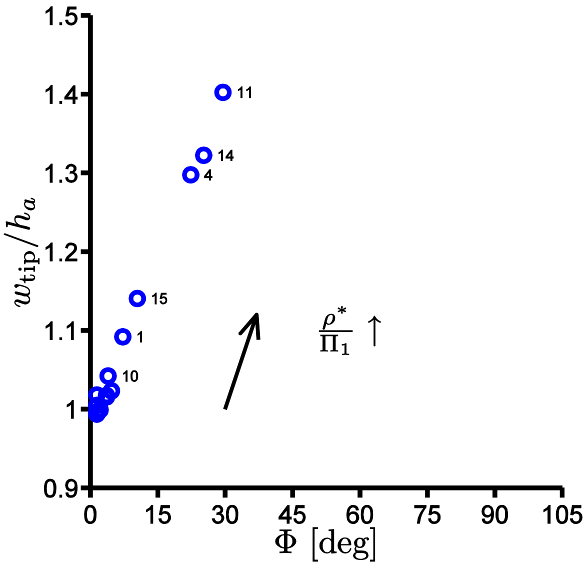

Figure 5-15 Tip deformations of a hovering isotropic Zimmerman wing in air at Re = 1.5×10^3 and k = 0.56 for different ρ^* and Π_1. The numbers shown next to the markers indicate their case numbers.

5.2.4 Scaling Parameterfor the Force Generation

From the results presented in Section 5.1 for the three different cases we have observed the followings: i) time-averaged force increased with increasing motion frequency; ii) the effects of change in structural properties, such as the thickness ratio, Young's modulus, or wing density, led to non-monotonic response in the force generation; iii) for the hovering isotropic Zimmerman wing the ratio between the density ratio and the effective stiffness was monotonic with the time-averaged lift generation. To explain the observed trends we will mainly analyze the physics based on Eq. (2) with simplifying approximations for the fluid dynamic force, f_f^* (see also Section 3.1), based on scaling arguments. The flow field and the structural displacement field should simultaneously satisfy Eq. (1) and Eq. (2) and among these two Eq. (2) will be considered, which has the advantage that this equation is linear except for the fluid dynamic force term as opposed to the Navier-Stokes equation which is nonlinear in the convection term. Subsequently, we will establish a relation between the time-averaged force and the maximum relative tip displacement by considering the energy balance.

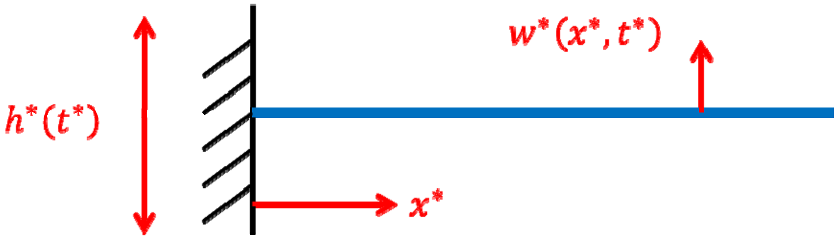

Figure 5-16 Schematic of the wing approximated as beam and the definitions of the wing deformation , prescribed motion at the root , and the spatial coordinate .

To capture the essence of the mechanism involved in the force enhancement due to flexibility, the interplay between the imposed kinematics, the structural response of the wing, and the fluid force acting on the wing are analyzed. The derivation leading to the relation between the time-averaged force acting perpendicular to the wing motion, and the maximum relative tip deformation , where is the displacement of the wing is relative to the imposed kinematics motion, see Figure 5-16, is lengthy and many of the steps are similar to those discussed in classical textbooks (e.g. [138]), however to account for the approximations involved full derivation is presented. Such treatment involving simplifying approximation is helpful, enabling the analysis, but mainly serves to elucidate the scaling analysis, not meant to offer complete solutions. Consider Eq. (2) in one-dimension in space with and time for the vertical displacement with the wing approximated as a linear beam, i.e.

— —— — —— (43)

where is the fluid force on the wing. A plunge motion Eq. (4) is imposed at the leading edge at = 0. At the trailing edge at = 1 is considered as a free end, i.e. with the boundary conditions

– (44)

$$\frac{\partial w^*(0,t^*)}{\partial x^*} = \frac{\partial^2 w^*(1,t^*)}{\partial x^*} = \frac{\partial^3 w^*(1,t^*)}{\partial x^*} = 0$$

and the initial conditions

$$w^*(x^*,0) = St\,\frac{\pi}{k}, \qquad \frac{\partial w^*(x^*,0)}{\partial t^*} = 0, \tag{45}$$

where the factors involving L/c_{m} become unity for the chordwise flexible case. For the spanwise flexible wing and the isotropic Zimmerman wing cases which are discussed in Section 5.2.2 and Section 5.2.3, respectively, Π_0 and Π_1 need to be corrected as $L/c_{\mathrm{m}} = AR$. Following the procedure described in Mindlin and Goodman [139], a PDE with homogeneous boundary conditions can be found by superimposing the plunge motion on the displacement $v(x^*,t^*) = w(x^*,t^*) - h(t^*)$, which gives

$$\Pi_0 \frac{\partial^2 v^*}{\partial t^{*2}} + \Pi_1 \frac{\partial^4 v^*}{\partial x^{*4}} = f_f^* - \Pi_0 \frac{d^2 h(t^*)}{dt^2} \tag{46}$$

for the PDE and

$$v^*(0,t^*) = \frac{\partial v^*(0,t^*)}{\partial x^*} = \frac{\partial^2 v^*(1,t^*)}{\partial x^{*2}} = \frac{\partial^3 v^*(1,t^*)}{\partial x^{*3}} = 0, \tag{47}$$

and the initial conditions

$$v^*(x^*,0) = \frac{\partial v^*(x^*,0)}{\partial t^*} = 0. \tag{48}$$

The consequence of having a sinusoidal displacement at the root is that the vibrational response of the wing is equivalent to a sinusoidal excitation force, which is the inertial force. The dynamic motion given by Eq. (46) is coupled to the fluid motion via the fluid force term f_f^* which cannot be solved in a closed form due to its nonlinearities. For high density ratio FSI systems, Daniel and Combes [80] and Combes and Daniel [81] have shown that the inertial force arising from the wing motion is larger than the fluid dynamic forces. In this dissertation to cover wider range of density ratios the fluid dynamic forces are included by considering the acceleration-reaction effects. The motivation stems from the scaling discussed in Section 3.1 that for high k the acceleration-reaction terms due to an accelerating body (see also [140]) contribute more on the wing than the fluid dynamic forces from the hydrodynamic impulse, see Table 5-2 for a summary of the non-dimensional numbers considered in this study. Hence, the wing dynamics is modeled with added mass for a flat plate, depending on the imposed wing acceleration as

$$f_f^*(t^*) = 2\pi^2 St\, k\cos(2\pi t^*), \tag{49}$$

hence the external force on the structural dynamics does not have spatial distribution explicitly accounted for and the external force is being simplified in temporal form. Combined with the inertial force the total external force $g^*(t^*)$ becomes

$$g^*(t^*) = f_f^*(t^*) - \Pi_0\frac{d^2h(t^*)}{dt^{*2}} = 2\pi^2\left(1+\frac{4}{\pi}\rho^* h_s^*\right) St\, k\cos(2\pi t^*). \tag{50}$$

Table 5-2 Range of the non-dimensional parameters considered in this study. The aspect ratio of the two-dimensional chordwise flexible airfoil is set to 1 for the reasons discussed in Section 2.2. The representative Section numbers are shown in the parentheses.

Case	Chordwise (5.2.1)	Spanwise (5.2.2)	Isotropic (5.2.3)
Re [10^3]	9.0	30	1.5
AR	1	3.0	3.8
h_s^* [10^{-3}]	0.56 ~ 4.23	10	20
ρ^*	7.8	7.8 ~ 2.7	10^1 ~ 10^4
Π_1/AR^3	0.3 ~ 129	7.9, 1.4	1.794 ~ 1794
k	1.2 ~ 6.5	0.4 ~ 1.82	0.56
St [10^{-2}]	7.5 ~ 40	2.0 ~ 10	25

Equation (46) can be solved using the method of separation, i.e. $v(x,t) =$

$X(x)T(t)$, resulting in

$$\frac{d^4X}{dx^{*4}} - k_n^4 X = 0, \tag{51}$$

$$\frac{d^2T}{dt^{*2}} + \omega_n^2 T = Q_n g^*(t^*), \tag{52}$$

where $Q_n(t^*)$ is a Fourier coefficient of a unit function in the spatial modes X_n satisfying,

$$\begin{gathered} \sum_{n=1}^{\infty} Q_n X_n = 1, \\ Q_n = \frac{\int_0^1 X_n dx^*}{\int_0^1 X_n^2 dx^*}, \end{gathered} \tag{53}$$

where we have normalized X_n, i.e.

$$\int_0^1 X_n^2 dx^* = 1. \tag{54}$$

The equation and the boundary conditions for $X(x^*)$ is the same as for a free vibrating cantilever beam, of which the solution is given numerous textbooks, e.g. [138]. The natural frequency is given by

$$\omega_n^2 = \left(\frac{k_n\ 1}{1}\right)^4 \frac{\Pi_1}{\Pi_0} = \left(\frac{2\pi f_n}{f}\right)^2, \tag{55}$$

where f_n is the natural frequency of the beam, i.e.,

$$(2\pi f_n)^2 = \left(\frac{k_n\ 1}{1}\right)^4 \frac{E\ I}{\rho_s A}, \tag{56}$$

where I is the moment of inertia, A is the cross sectional area of the wing represented as a beam, and k_n is the eigenvalue belonging to the spatial mode X_n that satisfies the transcendental equation

$$\cos(k_n L)\cosh(k_n L) = -1, \tag{57}$$

and can be approximated by the formula [138]

$$k_n L \approx \left(n - \frac{1}{2}\right)\pi. \tag{58}$$

where $k_1 L \approx 1.875$ and finally the spatial modes are given by

$$\begin{aligned} X(x^*) = -\frac{1}{2}\Bigg[&\{\cos(k_n x^*) - \cosh(k_n x^*)\} \\ &- \frac{\cos(k_n) + \cosh(k_n)}{\sin(k_n) + \sinh(k_n)}\{\sin(k_n x^*) - \sinh(k_n x^*)\}\Bigg]. \end{aligned} \tag{59}$$

The initial position of the beam is consistent with the imposed boundary condition. The solution for the temporal equation in $T(t^*)$ is

$$T_n(t^*) = \frac{2\pi\left(1 + \frac{4}{\pi}\rho^* h_s^*\right)\cdot St \cdot k \cdot Q_n}{\Pi_0(f_n^2/f^2 - 1)}\{\cos(2\pi t^*) - \cos(\omega_n t^*)\}, \tag{60}$$

which means that there is an amplification factor of $1/(f_n^2/f^2 - 1)$ depending on the ratio between the natural frequency f_n of the beam and the excitation frequency f. The full solution is $w^*(x^*, t^*) = h(t^*) + \sum_{n=1}^{\infty} X_n(x^*) T_n(t^*)$. The amplitude of the tip deformation, γ, for the first mode ($n = 1$) is given as

$$\gamma = \frac{\left(1 + \frac{4}{\pi}\rho^* h_s^*\right)\cdot St \cdot k}{\Pi_0(f_1^2/f^2 - 1)}, \tag{61}$$

relative to the imposed rigid body motion normalized by the chord. The parameter γ can be rewritten as

$$\frac{\gamma}{h_a/c_m} = \left(\frac{\rho_f c_m}{\rho_s h_s}\frac{\pi}{4} + 1\right)\frac{4}{\left(\frac{f_1}{f}\right)^2 - 1} \sim \frac{A+1}{\left(\frac{f_1}{f}\right)^2 - 1}, \tag{62}$$

where $f_1/f = \omega_1/(2\pi)$ is the frequency ratio and $A = \pi\rho_f c_m/(4\rho_s h_s)$ is the ratio between the acceleration-reaction force (added mass) and the wing inertia. Depending on the order of this ratio either the acceleration-reaction force term or the wing inertia force can be neglected. Equation (62) gives the relative wing tip deformation normalized by the plunge amplitude, which can be related to the Strouhal number based on the deformed tip displacement. Note that when A is sufficiently large, the inertia force term can be neglected and γ is then proportional to $Ah_a^* = \rho_f h_a/(\rho_s h_s)$ which is also used in Thiria and Godoy-Diana [68].

The proposed scaling parameter to estimate the resulting force on the flapping wing follows the observation that there exists a correlation between the dynamic deformation of the wing at the tip, γ, given by Eq. (61), and the static tip deflection which is $\langle C_F \rangle/\Pi_1$. To consider the non-dimensional energy equation, first multiply Eq. (46) with the relative wing velocity $\partial v^*/\partial t^*$ yielding,

$$\frac{\partial v^*}{\partial t^*}\Pi_0\frac{\partial^2 v^*}{\partial t^{*2}} + \frac{\partial v^*}{\partial t^*}\Pi_1\frac{\partial^4 v^*}{\partial x^{*4}} = \frac{\partial v^*}{\partial t^*}F(t^*) \tag{63}$$

where for simplicity the external force acting on the wing is abbreviated with $F(t^*)$. Substituting the separation variables, $v(x^*, t^*) = X(x^*)T(t^*)$, considering only the first mode, in Eq. (63) gives

$$\Pi_0\dot{T}\ddot{T}X^2 + \Pi_1\dot{T}TXX'''' = F(t)\dot{T}X, \tag{64}$$

where $(\dot{\ })$ denotes the time derivative and $(\ )'$ the spatial derivative. Integrating Eq. (64) in x from the wing root to the tip results in

$$\Pi_0 \dot{T}\ddot{T} \int_0^1 X^2 \, dx^* + \Pi_1 \dot{T} T \int_0^1 X X'''' \, dx^* = F(t^*) \dot{T} \int_0^1 X \, dx^*. \tag{65}$$

The second integral can be partially integrated using the boundary conditions to

$$\int_0^1 X X'''' \, dx^* = k_1^4 \int_0^1 X^2 \, dx^* \ = k_1^4 = \frac{\Pi_0}{\Pi_1} \, \omega_1^2 \tag{66}$$

where the normalization proporty of X, Eq. (54), is used. Inserting Eq. (66) into Eq. (65) yields,

$$\Pi_0 \dot{T}\ddot{T} + \Pi_1 \dot{T} T k_1^4 = F(t) \dot{T} Q_1, \tag{67}$$

where $Q_1 = \int_0^1 X \, dx^*$ as before, see Eq. (53). Now, Eq. (67) can be integrated as

$$\Pi_0 \dot{T} \mathrm{d}\dot{T} + \Pi_1 k_1^4 \, T \, \mathrm{d}T = X_1 F \, \mathrm{d}T, \tag{68}$$

or,

$$\mathrm{d}\left(\frac{1}{2} \Pi_0 \dot{T}^2 + \frac{1}{2} k_1^4 \Pi_1 T^2\right) = \mathrm{d}(Q_1 \, \langle C_F \rangle \, a \, T \ \ ), \tag{69}$$

where we have assumed that there exists a time-averaged value $\langle C_F \rangle$ with corresponding proportinality value a, such that

$$F \, \mathrm{d}T \approx a \, \langle C_F \rangle \, \mathrm{d}T = \mathrm{d}(a \, \langle C_F \rangle \, T). \tag{70}$$

The value a is approximated as a constant in this study, however in general a depends on time. Integration of Eq. (69) gives the energy balance

$$\frac{1}{2}\Pi_0\dot{T}^2+\frac{1}{2}k_1^4\Pi_1T^2-Q_1a\,\langle C_F\rangle\,T=C, \tag{71}$$

where C is an integration constant that will be determined. The first term in Eq. (71) is the kinetic energy, the second the strain energy, and the third term the work done by the external force on the wing. From kinematic relations when $\dot{T}=0$, the relative tip displacement is at maximum position, i.e. $T=T_{\max}$, corresponding to $v_{\text{tip,max}}$. On the other hand, if the displacement is at the neutral position, we have the maximum velocity in free-vibration $\dot{T}_{\max}$ with

$$\frac{1}{2}\Pi_0\dot{T}_{\max}^2=C. \tag{72}$$

Hence the energy balance Eq. (71) can be rewritten as

$$\frac{1}{2}\Pi_1k_1^4T_{\max}^2-Q_1a\,\langle C_F\rangle\,T_{\max}=\frac{1}{2}\Pi_0\dot{T}_{\max}^2. \tag{73}$$

Using the previously determined solution Eq. (60) the maximum relative tip displacement and the velocity can be approximated as

$$T_{\max}\approx\ b_1\gamma\,Q_1 \tag{74}$$

with b_1 again approximated as being some constant and

$$\dot{T}_{\max}=\begin{cases}\gamma\cdot 2\pi Q_1 & \text{if } 2\pi\gg\omega_1,\ \text{ i.e. } f_1\ll f\\ \gamma\cdot\omega_n Q_1 & \text{if } 2\pi\ll\omega_1,\ \text{ i.e. } f_1\gg f.\end{cases} \tag{75}$$

In the most situations the motion frequency ω is lower than the natural frequency of the wing ω_1, hence with some other constant b_2 not necessarily equal to b_1, we can approximate the maximum velocity as

$$\dot{T}_{\max} \approx b_2 \omega_1 \gamma Q_1 \tag{76}$$

Inserting the approximations Eq. (74) and Eq. (76) into the energy balance Eq. (71) gives

$$\frac{1}{2}\Pi_1 k_1^4 b_1^2 \gamma^2 - a\,\langle C_F\rangle\, b_1\gamma = \frac{1}{2}\Pi_0 b_2^2 \omega_1^2 \gamma^2, \tag{77}$$

which can be rewritten as

$$a\,\langle C_T\rangle\, b_1 = \frac{\Pi_1 k_1^4}{2}\,(b_1^2 - b_2^2)\gamma. \tag{78}$$

Finally, by factoring all constants in Eq. (78) into some constant c, the resulting relation between the time-averaged force $\langle C_F\rangle$ and the maximum relative tip displacement represented with the scaling factor γ is

$$\frac{< C_F >}{\Pi_1} = c\,\gamma. \tag{79}$$

The resulting scaling, Eq. (79) for the three canonical cases are shown in Figure 5-17. The nonlinearity exhibited in Figure 5-17(a) is due to the approximations made for the constant c which may be a function of γ or time. For the chordwise flexible airfoils both γ and the normalized force are significantly greater than other cases. When plotted in the log-scale, see Figure 5-17(b), the scaling for all cases considered becomes more evident. A linear fit on the data set with the coefficient of determination of R^2 = 0.98 indicates that the relation between the normalized force and γ is a power law with the exponent of 1.19. The relation originating from the dimensional analysis, Eq. (6), then simplifies to

$$\langle C_F\rangle = \Pi_1 \Psi(\gamma) \tag{80}$$

with $\Psi(\gamma) = 10^{0.98}\,\gamma^{1.19}$. The elastoninertial number, $\mathcal{N}_{\mathrm{ei}}$ that Thiria and Godoy-Diana

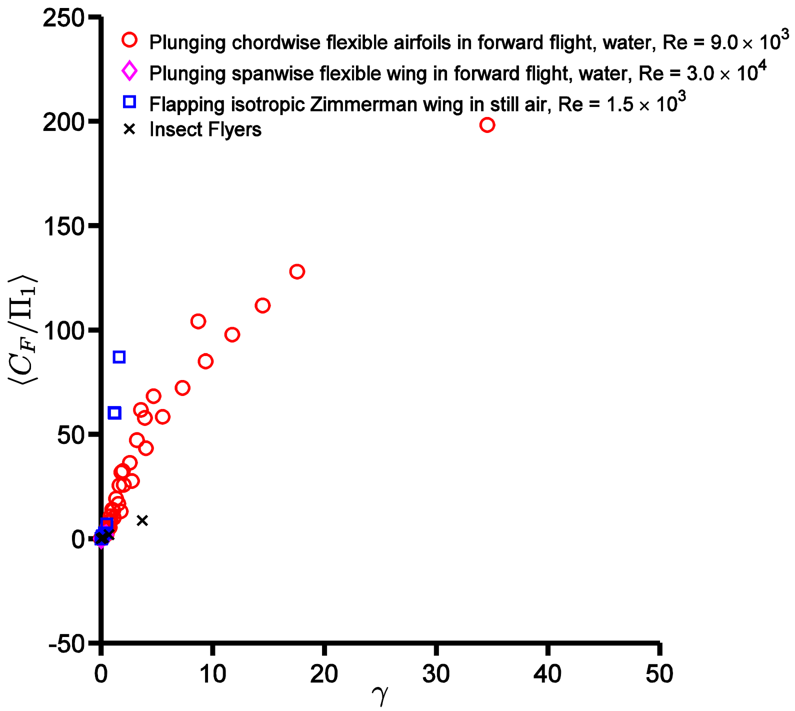

[68] proposed as the thrust scaling parameter in air is a special case of γ, i.e.

$$\gamma \xrightarrow{\rho h_s \gg 1 \text{ and } f/f_1 \gg 1} \mathcal{N}_{\text{ei}} \,. \tag{81}$$

For the spanwise flexible wing, although the Reynolds number and the thrust direction relative to the wing flexibility is different compared to the chordwise flexible airfoil, similar analysis could be made by approximating the three-dimensional wing as a beam with the correction factors $L/c_m = AR$ for Π_0 and Π_1 as discussed in Section 2.2. The force coefficient is scaled with the same parameters as for the chordwise flexible airfoils for the same reasons, i.e. $\langle C_F \rangle = \langle C_T \rangle/(St/k)$. The time-averaged thrust coefficient from the numerical computation of the two flexibilities for different motion frequencies fall on top of the previous scaling obtained for the chordwise flexible airfoils.

(a) linear scale

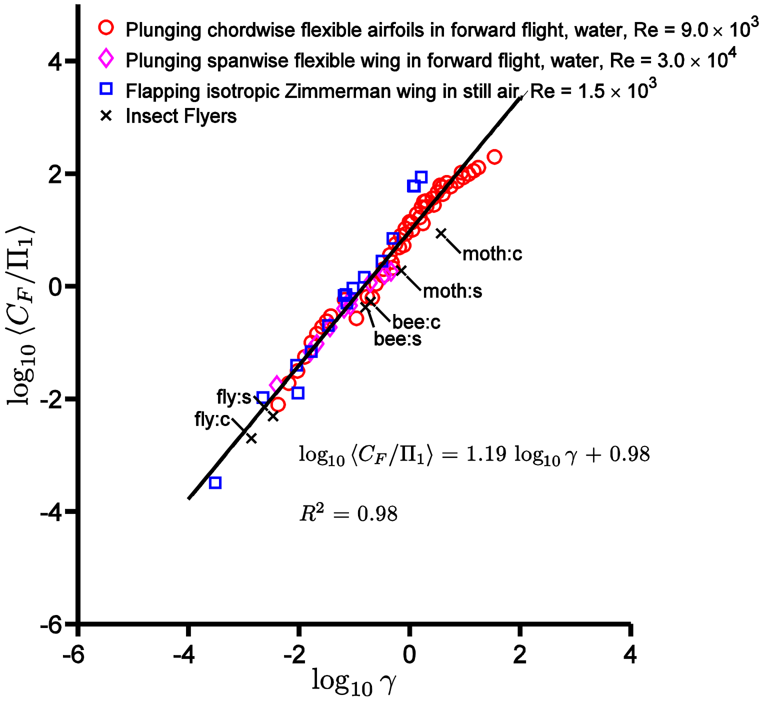

(b) log-scale

Figure 5-17 Normalized time-averaged force coefficients as function of γ. For the insect flyers the letter c and s correspond to chordwise and spanwise flexibility directions, respectively

Because the wing is hovering in air for the case of flapping Zimmerman wing, the density ratio is higher than in water. Hence, the inertial force dominates over the acceleration-reaction force as previously found [80,81]. The horizontal force $\langle C_F\rangle$ is found by normalizing $\langle C_L\rangle$ by h_s^* because the vertical force and the horizontal force are proportional to the thickness ratio, if we assume that the pressure differentials are of the order of $O(1)$. Although this is a simplification, for the sixteen training points the thickness ratio scaling is confirmed by taking the ratio between the maximum C_L and the maximum C_T within different motion cycles for all cases as shown in Figure 5-18, which indeed show that the pressure differentials are of the order of $O(1)$. Furthermore, the computed lift from the numerical framework represents only the fluid dynamic force without the inertial force of the wing. The inertial force that acts on the wing is estimated by multiplying the factor $\rho^* h_s^*/(St/k)$, which is the ratio between the inertial force

($\sim \rho^* h_s^* k^2$) and the fluid force ($\sim St\, k$) to $\langle C_L \rangle$. The resulting normalization for the vertical axis is then $\langle C_F \rangle = \langle C_L \rangle\ \rho^*/(St/k)$.

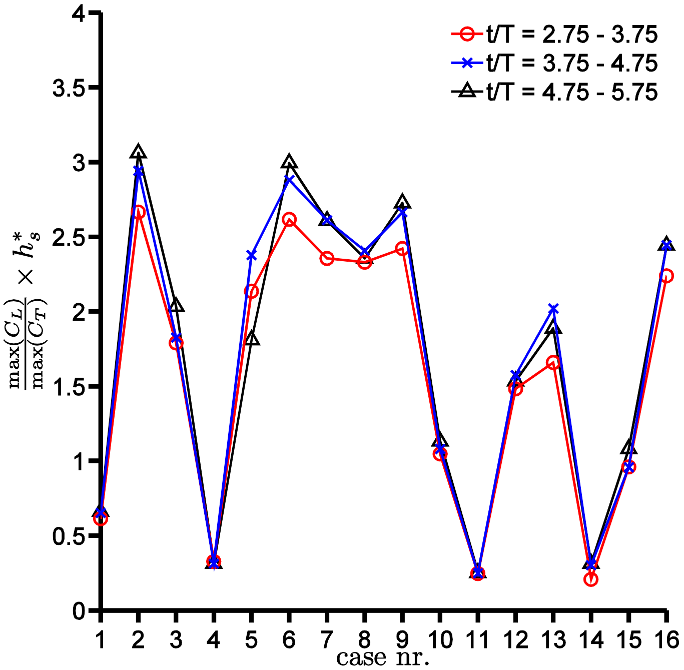

Figure 5-18 Ratio between max(C_L) and max(C_T) multiplied by h_s^* showing the order of magnitudes of the pressure differentials acting on the flapping Zimmerman wing hovering in air.

Even though the current case has different kinematics (plunging vs. flapping; forward flight vs. hover), different density ratio (low vs. high), and structural flexibilities (unidirectional vs. isotropic), the previous trend reemerges, suggesting the generality of this scaling parameter γ. The trends for the isotropic Zimmerman wing is slightly offset in the vertical direction suggesting that the resulting lift is lower. An important aspect is that the presence of the rigid triangle (see Figure 5-11) constraints the tip deformation, such that the resulting tip deformation is less than the setup where the imposed kinematics is actuated at the root of the wing without the rigid triangle.

Table 5-3 Kinematic, geometric, fluid, and structural parameters for the hawkmoth, bumble bee, and fruit fly obtained from the literature [141,142,143,144,145,70].

Insect	Hawkmoth	Bumble bee	Fruit fly
c_m [mm]	18.2	3.22	0.96
R [mm]	47.3	10.9	3.0
$\frac{\omega}{2\pi}$ [Hz]	26.1	181	240
ϕ_a [deg]	57.2	72	75
Re [10^3]	6.2	2.2	0.25
k	0.30	0.18	0.19
St	0.25	0.25	0.25
h_s^* [10^{-3}]	2.0	1.0	0.6
ρ^* [10^3]	2.0	2.1	1.1
$\Pi_{1,\mathrm{s}}$ [10^2]	0.43	1.4	26
$\Pi_{1,\mathrm{c}}$	0.53	2.8	211

For the isotropic Zimmerman wing case in hover, we could correlate the lift generation to γ. This result suggests extrapolation of the current scaling analysis for the lift generation of hovering insect flyers. The lift, in hover, for several insects is approximated as the experimentally measured weights of hawkmoth [141,142], bumble bee [143], and fruit fly [144,145]**.** To calculate the parameters listed in Table 5-3 flapping rectangular planform with constant thickness has been assumed with constant thickness and density. To compute the effective stiffnesses in the spanwise and the chordwise directions, i.e. $\Pi_{1,\mathrm{s}}$ and $\Pi_{1,\mathrm{c}}$, respectively, the flexural stiffness data presented by [70] along with their wing lengths have been used. The result is included in Figure 5-17 with the scaling

$$\frac{W}{\frac{1}{2}\rho_f U_{\mathrm{ref}}^2 c_m^2} = \Pi_1 \frac{St/k}{\rho^* h_s^*}\Psi(\gamma) \sim \Pi_1 \frac{\rho_f h_a}{\rho_s h_s}\Psi(\gamma)\,. \tag{82}$$

Again, the lift approximated with the weights of the insects scales with γ.

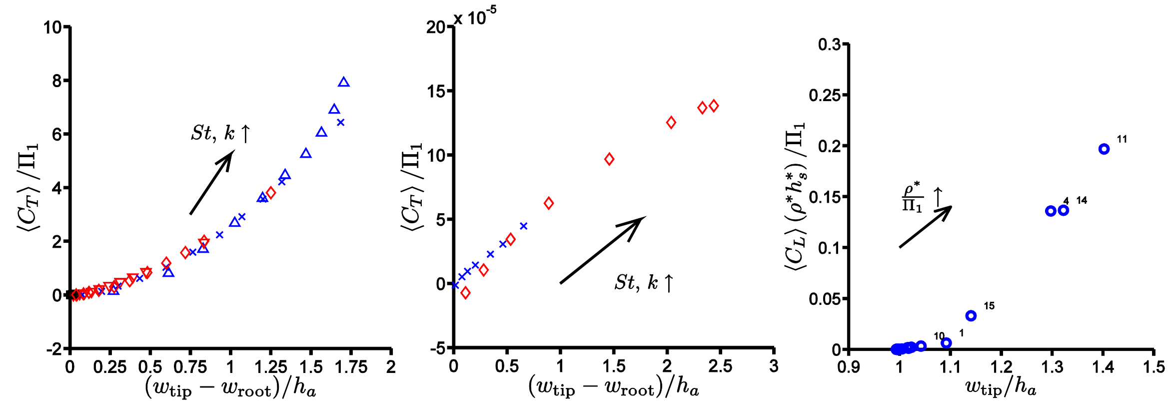

(a) Chordwise flexible:

$\Delta\ h_s^* = 0.56 \times 10^{-3}$

$\times\ h_s^* = 0.85 \times 10^{-3}$

$\diamond\ h_s^* = 1.13 \times 10^{-3}$

$\nabla\ h_s^* = 1.41 \times 10^{-3}$

$\square\ h_s^* = 4.23 \times 10^{-3}$

(b) Spanwise flexible:

$\times\ \Pi_1 = 121, \rho^* = 7.8$

$\diamond\ \Pi_1 = 38, \rho^* = 2.7$

(c) Isotropic Zimmerman

Figure 5-19 Time-averaged force (thrust or lift) coefficient normalized by the effective stiffness plotted against the maximum relative tip deformations for the current computations. The numbers shown in (c) next to the markers indicate their case numbers

The current analysis shows that the time-averaged force, such as the thrust or lift, can be related to the maximum relative tip displacement by normalizing the force by the effective stiffness, Π_1, resulting in a measure equivalent to the static tip displacement. Figure 5-19 illustrates the static displacement, $\langle C_T \rangle / \Pi_1$, as function of the relative tip displacement for all thicknesses and motion frequencies considered. The results for the five different thickness ratios collapse to a single curve with higher motion frequency leading to greater thrust. Note that the relation is not linear, indicating that c in Eq. (79) is actually not a constant. For the spanwise flexible wing case, although the *Very Flexible* wing has larger relative deformation, the effective stiffness is 5.6 times smaller than that of the *Flexible* wing. Hence even if the static tip displacement is larger for the *Very Flexible* wing at the highest motion frequency, the force corresponding to this deformation is smaller (see Figure 5-9 due to smaller effective stiffness, see Figure 5-19.

Furthermore, again, plotting the $\langle C_T \rangle / \Pi_1$ against the maximum relative tip deformation collapses both curves on top of each other. It is shown in Eq. (50) that for $\rho^* h_s^* \gg 1$ the inertial force will have greater influence on the wing deformation than the force due to acceleration-reaction force. In air, ρ^* is high, so that in addition to the normalization by the effective stiffness, the time-averaged force needs to be multiplied with $\rho^* h_s^*$ to account for the inertial force. Figure 5-19 again shows that the time-averaged force, in this case the lift of the hovering isotropic Zimmerman wing, can be scaled with the maximum relative tip displacement by properly normalizing the force.

5.3 Propulsive Efficiency of Oscillating Flexible Wings

The propulsive efficiency defined as

$$\eta = \frac{\langle C_T \rangle}{\langle C_P \rangle} \tag{83}$$

where $\langle C_P \rangle$ is the time-averaged power input for a purely plunging wing computed as

$$\langle C_P \rangle = \langle C_L \, \dot{h} \rangle \, . \tag{84}$$

Note that the time-averaged power due to inertia vanishes for sinusoidal motions [73] since

$$\langle C_{P,\text{inertia}} \rangle \sim \langle \ddot{h} \, \dot{h} \rangle = \int_0^1 \ddot{h} \, \dot{h} \, dt^* \sim \int_0^1 \cos(2\pi t^*) \, \sin(2\pi t^*) \, dt^* = 0. \tag{85}$$

The propulsive efficiency for the chordwise flexible airfoils described in Section 5.2.1 and the spanwise flexible wings in Section 5.2.2 are plotted against the St in Figure 5-20. For comparison purposes the experimental measurements [73,76] for both cases are included. For the chordwise flexible airfoils the efficiency increases with decreasing h_s^*. Furthermore, the efficiency first increases with increasing motion frequency, i.e. St since the plunge amplitude is kept constant, however then plateaus reaching some optimal efficiency. The thinnest airfoil generates the highest η. The experimental measurements illustrated in Figure 5-20(b) show a similar trend, however there is an offset compared to the computed values. Again, uncertainties involved in the computational modeling or experimental setup may play a role. Moreover, as it will be shown below, the magnitude of $\langle C_P \rangle$ is an order of magnitude smaller than $\langle C_T \rangle$, hence even a small uncertainty in the power input measurement will lead to large difference in the resulting η. For the spanwise flexible wings (Figure 5-20(c,d)), similar trends are found.

Before discussing the scaling of the power input and the propulsive efficiency, the scaling for the thrust generation for the chordwise flexible airfoils and the spanwise flexible wings are summarized in Figure 5-21 and is $\langle C_T \rangle / \beta_1 \sim \gamma^{1.18}$ with $\beta_1 = \Pi_1 / (k/St)$. The power of γ has changed slightly compared to the previously determined value of 1.19 (Figure 5-17) because the data points from the isotropic Zimmerman wing cases and the insects are excluded. Although the value is different, the qualitative trend of the propulsive efficiency that will be discussed later will remain the same.

An interesting discussion on the power input arises from the fact that the fluid dynamic force has been modeled as added mass term, which is proportional to the acceleration of the wing motion. If the wing were rigid, then, similar to the power input due to the inertial force,

$$\langle C_{P,\,\text{added mass, rigid}} \rangle \sim \langle \ddot{h}\,\dot{h} \rangle = 0,$$

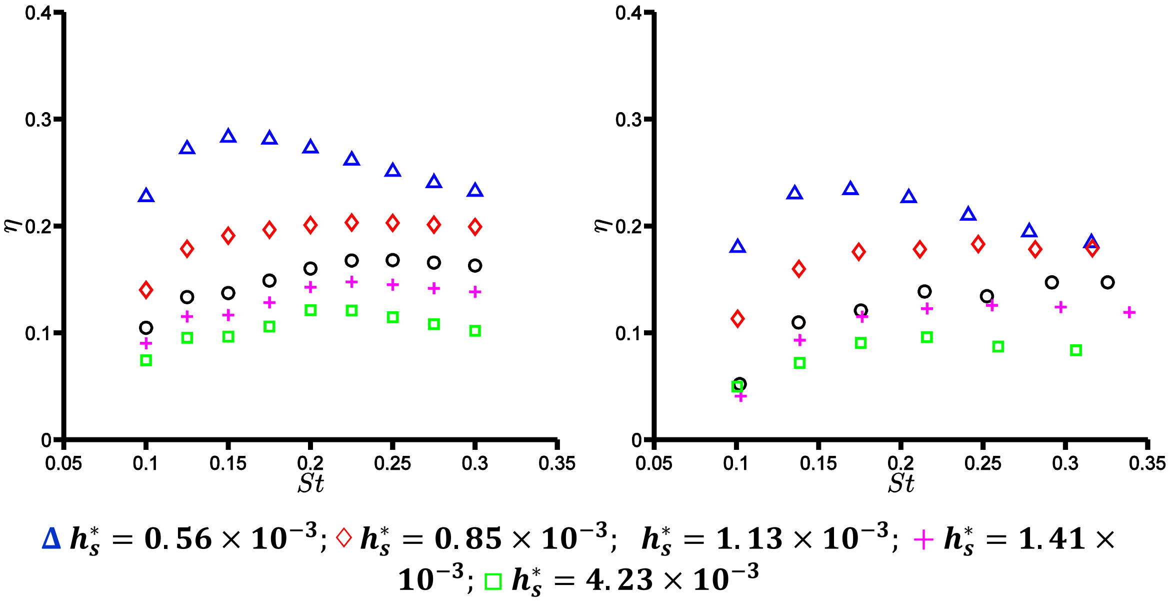

(a) chordwise flexible airfoil, computation

(b) chordwise flexible airfoil, experimental measurement extracted from [73]

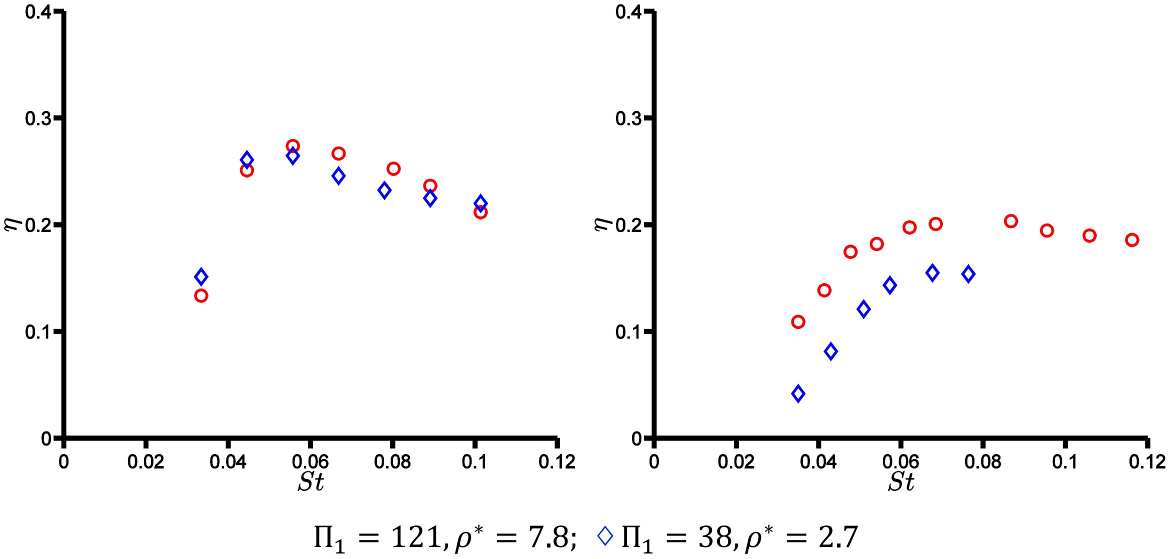

(c) spanwise flexible wing, computation

(d) spanwise flexible wing, experimental measurement extracted from [76]

Figure 5-20 Propulsive efficiency plotted against the Strouhal number for the chordwise flexible airfoil cases (a) – (b) and the spanwise flexible wing cases (c) – (d).

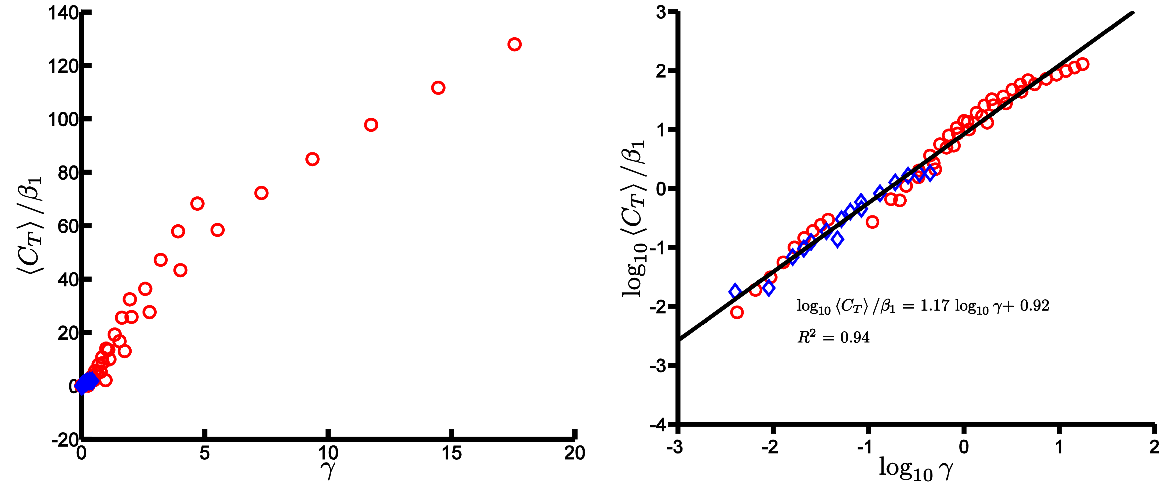

(a) linear scale

(b) log-scale

Figure 5-21 Time-average thrust scaling plotted against γ. : chordwise flexible airfoils; ◇: spanwise flexible wings.

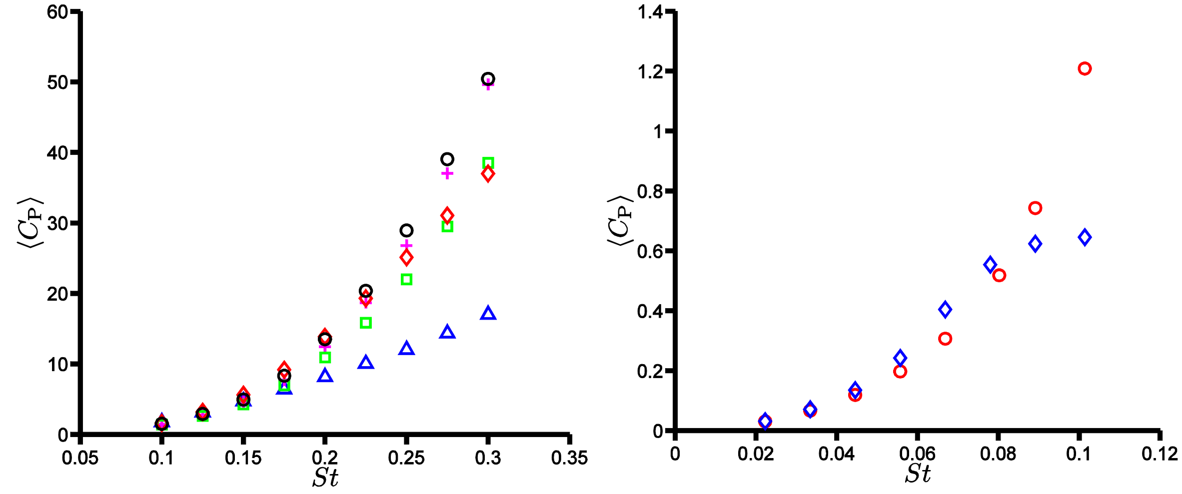

(a) chordwise flexible airfoil:

△ $h_s^* = 0.56 \times 10^{-3}$;

◇ $h_s^* = 0.85 \times 10^{-3}$;

$h_s^* = 1.13 \times 10^{-3}$

+ $h_s^* = 1.41 \times 10^{-3}$

□ $h_s^* = 4.23 \times 10^{-3}$

(b) spanwise flexible wing

$\Pi_1 = 121, \rho^* = 7.8$

◇ $\Pi_1 = 38,\ \rho^* = 2.7$

Figure 5-22 Time-average power input plotted against the Strouhal number

which is clearly not the case, see Figure 5-22. For small St the power input scales as St^2, however as the St increases either the thickness ratio for the chordwise flexible airfoils, or the different structural properties for the spanwise flexible wings affect the resulting power. That the power required is non-zero, means that the resulting instantaneous lift on the wing should have a phase lag relative to the imposed motion. A major source for the phase lag is due to the wing deformation. By acknowledging for the wing deformation given in Eq. (60), the time-averaged power input coefficient due to added mass can be approximated as in the first mode

$$\begin{aligned}\langle C_{P,\,\text{added mass}}\rangle &= \int_0^1 \Pi_0\left(\ddot{T}+\ddot{h}\right)\dot{h}\,dt^* = \int_0^1 \Pi_0 \ddot{T}\,\dot{h}\,dt^* \\ &= \Pi_0 \int_0^1 \frac{d^2(2\pi\gamma Q_1\{\cos(2\pi t^*)-\cos(\omega_1 t^*)\})}{dt^{*2}}\,\dot{h}\,dt^* \\ &= -4\pi^2\gamma Q_1 \Pi_0 \frac{St\,\pi}{k}\omega_1^2 \int_0^1 \cos(\omega_1 t^*)\,\sin(2\pi t^*)\,dt^* \\ &= \pi^2\,\frac{Q_1\,\gamma^2 k_1^8\,\Pi_1^2}{k^2\left(1+\frac{4}{\pi}\rho^* h_s^*\right)} \sim \frac{\Pi_1^2}{k^2\left(1+\frac{4}{\pi}\rho^* h_s^*\right)}\gamma^2 = \beta_2\gamma^2\end{aligned} \tag{86}$$

where the integral is approximated as

$$\begin{aligned}\int_0^1 \cos(\omega_1 t^*)\,\sin(2\pi t^*)\,dt^* &= \frac{2\pi(1+\cos\omega_1)}{\omega_1^2-4\pi^2} \approx -\frac{\pi\omega_1^2}{\omega_1^2-4\pi^2} = -\frac{1}{4\pi}\frac{\omega_1^2}{\left(\frac{\omega_1}{2\pi}\right)^2-1} \\ &= -\frac{\Pi_1}{4\pi}\frac{\gamma}{St\,k\left(1+\frac{4}{\pi}\rho^* h_s^*\right)}.\end{aligned} \tag{87}$$

For $\Pi_1 \gg \Pi_0$ the scaling for $\langle C_P\rangle$ reduces to $St^2(1+4\rho^* h_s^*/\pi)$, hence in water, such as in the experimental setup considered in this case [73,76] or for fixed density ratios and thickness ratios of the wing the $\langle C_P\rangle \sim St^2$, consistent with the previous literature [76,69] and Figure 5-22.

Figure 5-23(a) shows the time-averaged power input normalized by β_2 given in Eq. (86) against γ^2 for both chordwise flexible airfoil and spanwise flexible wing cases. As the scales of $\langle C_P \rangle$ vary enormously, $\langle C_P \rangle / \beta_2$ is plotted against γ in log-scale. A linear fit with $R^2 = 0.98$ indicates that the power input scales with $\gamma^{2.13}$.

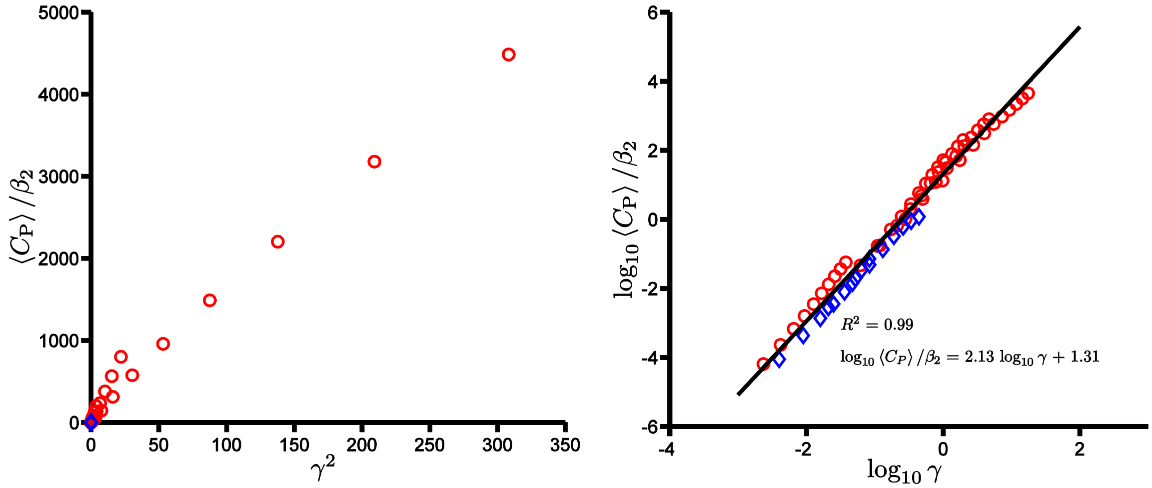

(a) linear scale: γ^2

(b) log-scale: γ

Figure 5-23 Time-average power input normalized by $\beta_1$plotted against γ^2. : chordwise flexible airfoils; ◇: spanwise flexible wings.

The scaling for the propulsive efficiency now follows from the scaling for the thrust, i.e. $\langle C_T \rangle / \beta_1 \sim \gamma^{1.17}$ with $\beta_1 = \Pi_1 / (k/St)$ and $\langle C_P \rangle / \beta_2 \sim \gamma^2$ with $\beta_2 = \frac{\Pi_1^2}{k^2\left(1+\frac{4}{\pi}\rho^* h_S^*\right)}$ as

$$\eta = \frac{\langle C_T \rangle}{\langle C_P \rangle} \sim \frac{\beta_1\, \gamma^{1.17}}{\beta_2\, \gamma^2} \rightarrow \frac{\eta}{\beta_3} \sim \gamma^{1.17}, \tag{88}$$

where $\beta_3 = \frac{St\, k}{\Pi_1} \frac{\left(1+\frac{4}{\pi}\rho_S^* h_S^*\right)}{\gamma^2}$. The resulting scaling is shown in Figure 5-24.

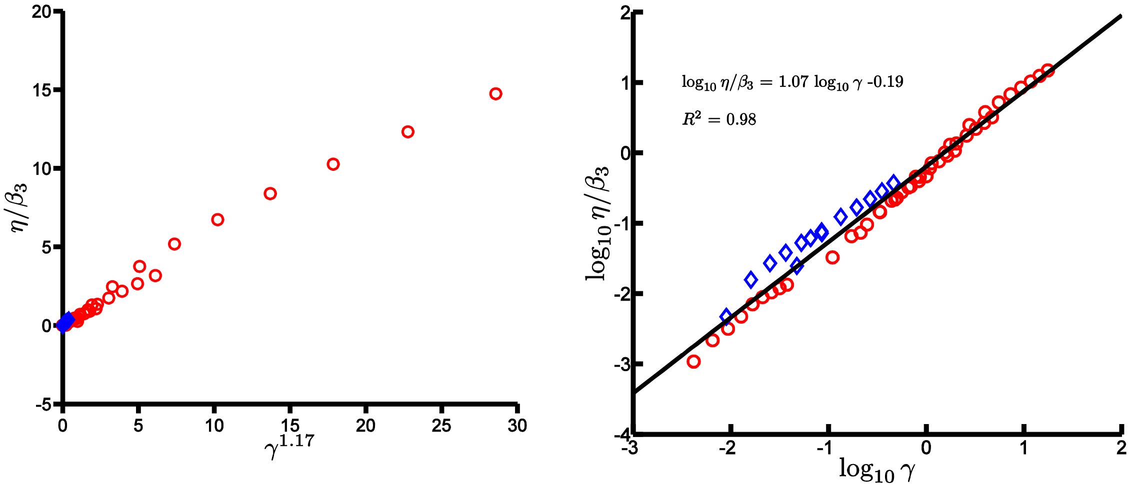

(a) linear scale: $\gamma^{1.17}$

(b) log-scale: γ

Figure 5-24 Propulsive efficiency normalized by $\boldsymbol{\beta_1}$plotted against $\boldsymbol{\gamma}$.
: chordwise flexible airfoils; ◇: spanwise flexible wings.

5.4 Implications of the Scaling Parameters on the Fluid Dynamic Performance of Oscillating Flexible Wings

The time-averaged force $\langle C_F \rangle$ and the propulsive efficiency η could be related to the resultant force on the wing depending on the situation, such as fluid/inertial force, with/without freestream, or thrust/lift/weight. The current result enables us to estimate the order of magnitude of the time-averaged force generation and and its efficiency for a flexible flapping wing using *a priori* known parameters.

Furthermore, the scaling can guide design of flapping wing micro air vehilces. For example, to support a given weight W_{body} of a vehicle body in air, the scaling Eq. (82) reduces to

$$W_{\text{body}} \sim \frac{\rho_s^1 R^{3.19} f^{2.38} \phi_a^{2.19} c_{\text{m}}^{1.57}}{h_s^{0.38} E^{0.19}} \rightarrow f \sim \frac{m^{0.42} g^{0.42} h_s^{0.16} E^{0.080}}{\rho_s^{0.42} R^{1.34} \phi_a^{0.92} c_m^{0.66}} \tag{89}$$

where m is the mass of the body, g is the acceleration of gravity, assuming $\Pi_1 \gg \Pi_0$. The condition $\Pi_1 \gg \Pi_0$ is satisfied when $f_1 \gg f$ and simplifies the algebra, however it poses constraints on the range of the structural properties, such that the natural frequency of the wing is higher than the motion frequency. Relation Eq. (89) shows that either increasing the wing area, motion frequency, or the flapping amplitude helps to generate sufficient lift to sustain hover flight. On the other hand, by making the wing softer, i.e. reducing the Young's modulus or wing thickness, wing deformations will increase leading to higher lift generation. However, softening the wing further will violate the frequency ratio assumption: $f_1/f \gg 1$. The relation given for the flapping frequency has similar correlation as the one identified by Pennycuick [146]. Note that the wing weight is assumed to be negligible compared to the body weight in this discussion.

An another implication of the scaling is the interesting behaviour of the role of h_s^* for the chordwise flexible airfoil cases shown in Section 5.2.1. It was observed that the $\langle C_T \rangle$ increased first and then decreased with decreasing h_s^*, see Figure 5-4. Using the current scaling, which is repeated as

$$\langle C_T \rangle \sim \Pi_1 \frac{St}{k} \gamma^{1.17} = \Pi_1 \frac{h_a}{c_m} \left\{ \frac{St\, k}{\Pi_0 \left(\frac{k_1^4}{4\pi^2} \frac{\Pi_1}{\Pi_0} - 1 \right)} \right\}^{1.17} \tag{90}$$

consider first the situation that h_s^* is large, i.e. $\Pi_1 \gg \Pi_0$. Then the denominator in γ can be approximates as $\Pi_0 \left\{ \frac{k_1^4}{4\pi^2} \frac{\Pi_1}{\Pi_0} - 1 \right\} \approx \Pi_1$ yielding

$$\langle C_T \rangle \sim St^2 \left(\frac{St\, k}{\Pi_1} \right)^{0.17} \tag{91}$$

hence by reducing the thickness ratio, $\Pi_1 \sim h_s^{*3}$ will decrease, leading to the observed enhanced $\langle C_T \rangle$. However, decreasing h_s^* further, the frequency ratio f_1/f will be eventually of the same order of magnitude, resulting in a different physical behaviour. If, say $f_1/f = O(1)$, but not in resonance region, then the denominator in γ will scale as $\Pi_0 \left\{ \frac{k_1^4}{4\pi^2} \frac{\Pi_1}{\Pi_0} - 1 \right\} \approx \Pi_0$. Then, the resulting scaling will be

$$\langle C_T \rangle \sim St^2 \left(\frac{St\,k}{\Pi_0}\right)^{0.17} \frac{\Pi_1}{\Pi_0} \tag{92}$$

Since $\Pi_1 \sim h_s^{*3}$ and $\Pi_0 \sim h_s^*$, we have $\langle C_T \rangle \sim h_s^{*1.82}$. This is consistent with the trend shown in Figure 5-4 that reducing the thickness ratio further, the thrust deterioates.

The thrust scaling for oscillating flexible wings in water in forward motion, Eq. (90) can be rewritten as

$$\langle C_T \rangle \sim St^2 \left(\frac{\rho_f h_a}{\rho_s h_s}\right)^{0.17} \left(\frac{f_1}{f}\right)^2 \left\{\frac{1}{\left(\frac{f_1}{f}\right)^2 - 1}\right\}^{1.17}, \tag{93}$$

and since $St \sim \omega$, $k \sim \omega$, and $\Pi_0 \sim k^2 \sim \omega^2$ the thrust has a maximum at the resonance frequency. In reality, there is damping in the system, either structural or aerodynamic [69]. Although the effects of damping is not considered in this dissertation, applying the effects of damping for linear oscillators (e.g. [138]) yields the resonance frequency slightly below the natural frequency of the wing with finite value for the maximum relative wing tip deformation, hence the thrust, see Figure 5-25(a,b). In Figure 5-25(b) the effects of damping has been incorporated by approximating the denominator term as

$$\sqrt{\left\{1 - \left(\frac{f}{f_1}\right)^2\right\}^2 + \left(d\frac{f}{f_1}\right)^2} \tag{94}$$

where d is some small damping coefficient. This finding is consistent with the previous findings that the optimal propulsive performance is found near the natural frequency of the wing, but slightly below [45,82,68,69].

The propulsive efficiency scaling Eq. (88) can be rewritten in terms of frequency ratio f/f_1 as

$$\eta \sim \left\{1 - \left(\frac{f}{f_1}\right)^2\right\}^{0.83} \left(\frac{f}{f_1}\right)^{0.34} \tag{95}$$

which has a local maximum at $f = 0.41f_1$. Depending on the scaling of the force, the optimal frequency can be found as

$$\frac{\partial\eta}{\partial f} = 0 \rightarrow \frac{f}{f_1}\bigg|_{\mathrm{opt}} = \sqrt{\beta - 1}, \tag{96}$$

where β is the exponent of γ in the force scaling, i.e. 1.18 in Eq. (88), or 1.19 in Eq. (79) which yields the optimal frequency of 0.5 of the natural frequency. This indicates that the optimal efficiency is not achieved at the resonance, however the optimal frequency is some fraction of the natural frequency of the wing, which is also consistent with the previous findings in the literature [85,86,147,68,69], see Table 5-4. Figure 5-25(c) which plots Eq. (95) as function of the frequency ratio shows that the efficiency increases with the increasing frequency ratio until the optimal efficiency and then drops to zero at the resonance frequency. Since the undamped linear oscillator is unable to represent the resonance behavior correctly, an arbitrary damping has to be included in the system as before. Figure 5-25(b) shows the effects of including damping, where d is taken as 0.0, 0.2, and 0.4: the optimal frequency ratio increases with increasing d as well as the efficiency at the resonance frequency. Note also the similarity between Figure 5-25(b) with the computed propulsive efficiency curves shown in Figure 5-20. Finally, a qualitative comparison is shown in Figure 5-26 where the propulsive force and efficiency as function of the frequency ratio is plotted based on the current scaling and the measurements reported in Ramananarivo et al. [69]. Although the precise detail is different, the overall qualitative trend is similar.

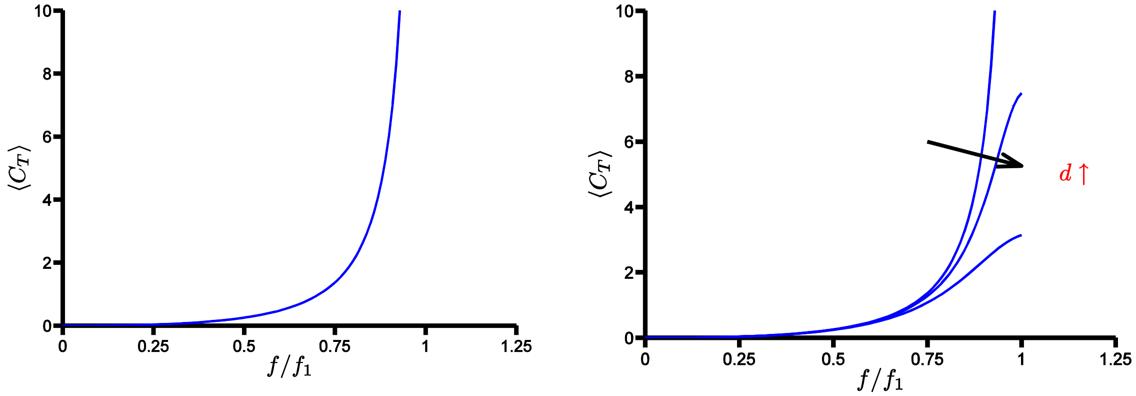

(a) undamped force (b) force with damping

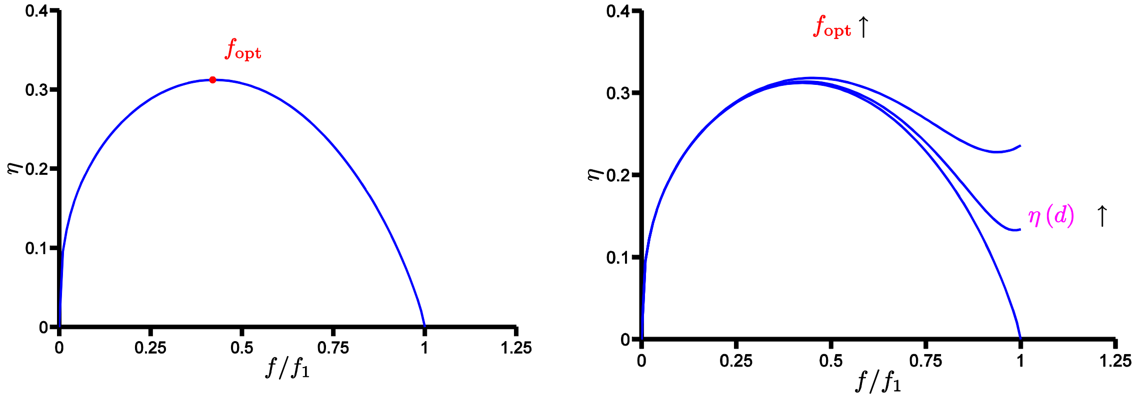

(c) undamped efficiency (d) efficiency with damping

Figure 5-25 Force and propulsive efficiency plotted against the frequency ratio $\boldsymbol{\omega/\omega_1}$.

Table 5-4 Comparison of the optimal frequency ratios from the values reported in the literature and the current study.

Literature	$\boldsymbol{f/f_1}$	Description
Vallena et al. [86]	0.3	Hover, 2D airfoil, torsion spring model
Yin & Luo [147]	0.4-0.5	Hover, 2D airfoil, membrane model
Ramananarivo et al. [69]	0.5-0.6	Self-propelled flapper experiment
Current study	**0.41**	**Scaling analysis**

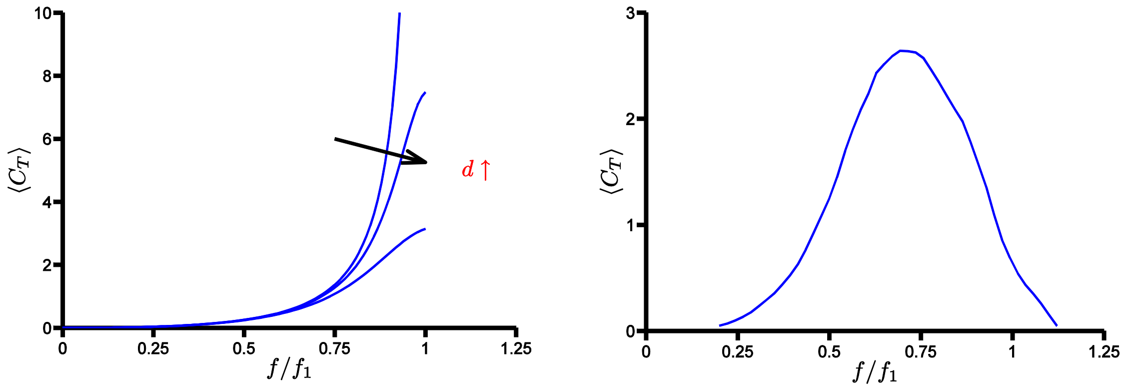

(a) propulsive force, current study

(b) propulsive force, data extracted from Ramananarivo et al. [69] for the thrust power p_T

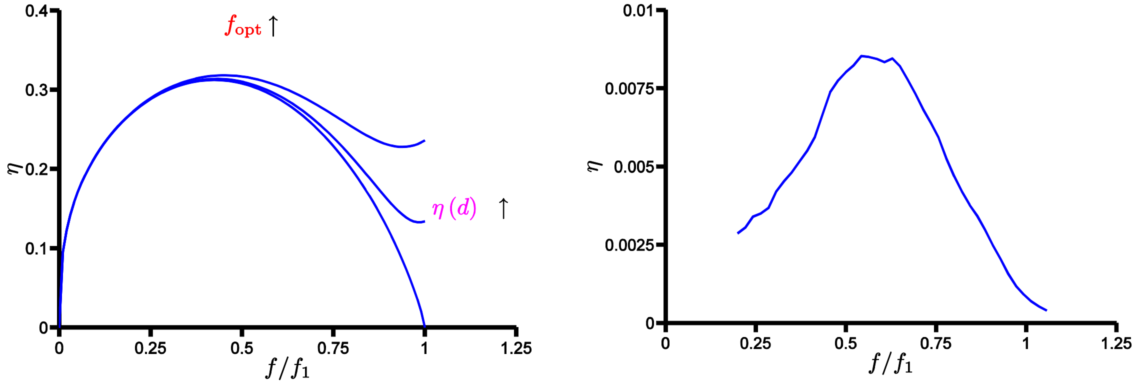

(c) propulsive efficiency, current study

(d) efficiency interpolated from the thrust power p_T and input power p_i extracted from Ramananarivo et al. [69]

Figure 5-26 Comparison of the propulsive force and efficiency from the current study and from the measurements obtained by Ramananarivo et al. [69].

Finally, the scaling parameters for diverse flow and kinematics conditions are summarized in Table 5-5. For the forward flight in water the effective stiffness Π_1, the normalized plunge amplitude h_a^*, the mass ratio $\mu_s = \rho_f h_a/(\rho_s h_s)$, and the frequency ratio f_1/f dictate the propulsive force and the efficiency. For hover in air, for the studied kinematics, the role of the mass ratio is taken over by the factor $\rho^* h_a^* = \mu_s/h_s^*$. The efficiency for the hover motion in air is left as future work in this dissertation and the resulting scaling is only predicted by following the same argument as for the propulsive efficiency in forward flight in air.

For an example of a 2% thickness wing with rectangular platform made of aluminum hovering in air, the optimal frequency of the flapping motion is 5.4 Hz when the wing has a chord length of 20 cm and span of 50 cm with a flapping amplitude of 30 deg. Scaling down the geometry of the wing ten times to the chord length of 2 cm and span of 5 cm, keeping the aspect ratio the same, the optimal flapping frequency increases to 54 Hz. The resulting propulsive force coefficient and the propulsive efficiency remain the same for both cases. However, the dimensional propulsive force and the power required will be 100 times smaller for the smaller sized wing, proportional to the square of the chord. On the other hand, for the same aspect ratio and the thickness ratio, the volume of the wing is proportional to cubic power of the chord. Consequently, for the same material, the mass of the smaller wing is 1000 times smaller. The current scaling shows, consistent with Shyy et al. [3] that smaller flyers need to flap faster from the efficiency point of view, but the relative payload capacity increases because its weight reduces at a much faster rate compared to a larger flyers.

Table 5-5 Summary of the scaling proposed. Note $\boldsymbol{\beta_1}$ is $\frac{\Pi_1 St}{k}$ for forward flight in water and $\frac{\Pi_1 St}{\rho^* k}$ for hovering flight in air, and $\boldsymbol{\beta_3}$ is $\frac{St\,k}{\Pi_1}\frac{\left(1+\frac{4}{\pi}\rho^* h_s^*\right)}{\gamma^2}$.

		Forward flight, water	Hover, air
Force	$\beta_1 \gamma^{1.19}$	$\Pi_1 h_a^* \left(\frac{\rho_f h_a}{\rho_s h_s}\right)^{1.19} \left\{\frac{1}{\left(\frac{f_1}{f}\right)^2 - 1}\right\}^{1.19}$	$\Pi_1 h_a^{*\,1.19} \left(\frac{\rho_f h_a}{\rho_s c_m}\right) \left\{\frac{1}{\left(\frac{f_1}{f}\right)^2 - 1}\right\}^{1.19}$
Efficiency	$\beta_3 \gamma^{1.17}$	$\left(\frac{\rho_f h_a}{\rho_s h_s}\right)^{0.17} \left(\frac{f}{f_1}\right)^{0.34} \left\{1 - \left(\frac{f}{f_1}\right)^2\right\}^{0.83}$	

Notice that the factor $\rho^* h_a^* = \rho_f h_a/(\rho_s c_m)$ is much smaller than $\mu_s = \rho_f h_a/(\rho_s h_s)$ hence resulting in a much lower propulsion for the hovering symmetric flap/plunge motion in air, since the thickness ratio is usually only of the order of 0.01. This order estimation is consistent with the values shown in Ref. [69]. For the hovering Zimmerman wing the ratio between the propulsive force C_L and the force required for input power, C_T, was of the order of h_s^*, see Figure 5-18.

This scaling suggests that the insects may require different mechanisms, such as active or passive pitching motion with reinforced leading edge, which is commonly observed in many insect wings. Furthermore, non-symmetric motions, such as figure-8 motion where the wing experiences forward motion may yield higher efficiency. Finally, anisotropic wing structures with different orders of flexibility may be essential to evince the propulsive efficiency mechanism of insects.

5.5 Summary

For flexible wings oscillating in water or air, the force generation and the propulsive efficiency of the wings were considered. Although the previous studies (e.g. [80,81,68,69]) showed that the fluid dynamic force on the wings is negligible compared to the inertial force, to account for the low density ratio effects, the fluid force due to acceleration-reaction force is additionally considered. Scaling analysis for the force showed that if $\rho^* h_s^* \gg 1$ the inertial force is dominant, otherwise the fluid dynamic force when $\rho^* h_s^* \ll 1$. Moreover, for high Reynolds number and reduced frequency flows the acceleration-reaction force would be the dominant component of the fluid dynamic force acting on the wing.

By modeling the wing as a beam scaling for the propulsive generation, the work done, and the propulsive efficiency were estabilished. The propulsive generation was related to the maximum relative tip displacement, the work done the phase lag between the wing tip and the root, and the propulsive efficiency the ratio between the former and the latter.

Although the scaling analysis considers only the time-averaged propulsion and simplifies still yet to be understood detailed mechanisms, such as the relation between the thrust and lift, or the parameteric dependence of the instantaneous force generation, current method enables the analytic expressions, so that the underlying mechanisms can be highlighted.

The scaling for the propulsive efficiency shows that the maximum force is generated when the motion frequency is near the natural frequency of the wing. Moreover, the optimal efficiency is obtained when the frequency is about 0.41 of the natural frequency. This finding suggests that a MAV could adjust its flapping frequency to produce maximum propulsion or sustain energy efficiency motion depending on the mission. It should be noted that the current scaling is strictly only applicable for high Reynolds number and high reduced frequency systems, where the acceleration-reaction force would dominate the fluid dynamic force acting on the wing. Applicability of the current scaling for different parameter regime, such as low Reynolds number, e.g. $Re = 100$, hovering or low reduced frequency motion systems, will be assess in the future.

Chapter 6.

Concluding Remarks

6.1 Summary and Conclusions

This dissertation addresses modeling aspects of the fluid physics and fluid dynamic performances associated with flapping wings. Consistent dimensional analysis and non-dimensionalization of the governing equations for the fluid and the wing structure led to a system of non-dimensional parameters: Reynolds number (Re), reduced frequency (k), Strouhal number (St), aspect ratio (AR), effective stiffness (Π_1), effective angle of attack (α_e), thickness ratio (h_s^*), and the density ratio (ρ^*). Based on a control volume analysis scaling arguments were used to identify different regimes in the parameter space. For the two sources of forces, i.e. hydrodynamic impulse term and acceleration-reaction force term, the following scaling was found

(i) Strouhal number is proportional to total fluid dynamic force felt on the wing: Increasing Strouhal number will increase both the hydrodynamic impulse and the acceleration-reaction force terms.

(ii) As the Reynolds number and the reduced frequency increase, the fluid dynamic force felt on a moving body, such as a rigid or deforming wing in air or water, will be dominated by the acceleration-reaction force term, which is proportional to the acceleration of the body motion.

At the Reynolds number regime of $O(10^4)$ and reduced frequency of 0.25 flow the interplay between the imposed kinematics, the airfoil shape, and the Reynolds number is probed for two airfoils using RANS computations without laminar-to-turbulence transition model: a SD7003 airfoil, and a two-dimensional flat plate with 2.3% thickness undergoing two sets of wing kinematics (i.e., pitching and plunging, and pure plunging) at Re range from 1×10^4 to 6×10^4, k of 0.25 and St of 0.04. The airfoil shape plays an important role to determine the flow features generated by the pitching and plunging, and pure plunging kinematics. Due to the larger leading edge radius of the SD7003 airfoil, the effects of Reynolds number are obviously observed. For pitching and plunging case, more attached flow feature are present at higher Re, whereas flow separations from the leading edge were observed at lower Re. For pure plunging case a leading edge separation is seen at all Reynolds numbers. Furthermore, it is found that two-dimensional RANS computations with the Menter's original and modified SST turbulence models provided qualitatively, and quantitatively - depending on the flow conditions - good predictions in terms of velocity fields compared to two-dimensional phase-averaged PIV data in the water channel from two different facilities. The conclusions for the fluid dynamics probed in the parameter space of $Re = O(10^6)$, $k = 0.25$, $St = 0.04$ are as follows:

(iii) Regarding the impacts of turbulence models on flow field around the SD7003, when the flow is attached, such as under pitching and plunging motion, the original formulation of SST turbulence closure offers consistently favorable agreement with the experimental results, while the modified SST turbulence model overpredicts flow separation. This can be due to a limiter in the production term of the turbulence kinetic energy equation reducing the build-up of turbulence near stagnation point regions, reducing the eddy viscosity. On the other hand, if the flow exhibits massive separation, the modified SST turbulence model shows better prediction of the experimental results, such as capturing flow reattachment. Finally for the flat plate cases, the leading edge effect that the radius of curvature is small, overwhelms the difference between turbulence models.

(iv) For pitching and plunging case the flow over the SD7003 airfoil is attached in both experimental data, and the numerical data using the original SST turbulence model at $Re = 3\times10^4$, and 6×10^4. At $Re = 1\times10^4$ separation has been evinced from the leading edge both experimental as well as computational approaches.

(v) For pure plunging SD7003 airfoil case, depending on the turbulence characteristics including those caused the motion of the wing, and the implied eddy viscosity level, qualitatively different flow structures are observed experimentally and computationally.

(vi) In case of the flow over the flat plate in all approaches the geometrical effect at the sharp leading edge of the flat plate is dominant, and triggers substantial separation from the leading edge for both kinematics.

(vii) Regarding the comparison between SD7003 airfoil and flat plate, it was found that the mean/max lift coefficient of the flat plate is less sensitive to the variation of Reynolds number than the SD7003 airfoil. Although the maximum lift coefficient of flat plate is larger for all Reynolds numbers considered than that of SD7003 airfoil cases, the mean lift coefficient varies more strongly with the Reynolds number. There is significant difference in instantaneous lift coefficient, and flow structures between both airfoils under the same kinematics and flow conditions.

(viii) In 3D the presence of TiV mitigates the LEV generation resulting in smaller lift magnitude during the downstroke of a pitching and plunging flat plate at Re = 6×10^4. During the upstroke where the TiV is small, the flow field and the force felt on the wing were comparable to its 2D counterpart.

For flexible wings oscillating in water or air, the force generation and the propulsive efficiency of the wings were considered. Although the previous studies (e.g. [80,81,68,69]) showed that the fluid dynamic force on the wings is negligible compared to the inertial force, to account for the low density ratio effects, the fluid force due to acceleration-reaction force, approximated by the force due to added mass of a rigid flat plate, is additionally considered. For the cases considered, where the Reynolds number is in the order of $O(10^3 - 10^4)$ and reduced frequency $O(1)$, the followings were shown.

(ix) The tip deformation is an outcome of the interplay between the imposed kinematics and the response of the wing structure dictated by the wing tip amplitude and the phase lag. The amplitude of the maximum relative wing tip deformation, γ, was obtained from the beam analysis and is only function of the *a priori* known non-dimensional paramters. By considering the energy balance of the wing the time-averaged force normalized by the effective stiffness was related to γ , and a scaling was established as $\langle C_F \rangle = \Pi_1 \Psi(\gamma)$ where $\langle C_F \rangle$ is the force that is responsible for the wing deformation.

(x) The time-averaged force $\langle C_F \rangle$ can be related to the resultant force on the wing depending on the situation, such as fluid/inertial force, with/without freestream, or thrust/lift/weight. The current result enables us to estimate the order of magnitude of the time-averaged force generation for a flexible flapping wing using *a priori* known parameters.

Furthermore, for the propulsive efficiency, defined as the ratio between the time-averaged propulsive force and the power input, similar scaling analysis was performed:

(xi) The power input, which is equivalent to the work done during one motion cycle, could be scaled by accounting for the wing deformations which introduces a phase lag in the resulting fluid dynamic force with respect to the motion.

(xii) The power input scales with St^2 for low frequency ratio (f/f_1) motions. For higher frequency ratio motions the effects of the inertia and the stiffness of the wing will influence the power input.

(xiii) The propulsive efficiency scales with $St^2 \langle C_T \rangle$ at low frequency ratios for forward flight. In this regime increasing propulsion results in higher propulsive efficiency. For higher frequency ratio motions the increase of the power input will overshadow the propulsion, deterioating the efficiency.

(xiv) Optimal frequency ratio for the propulsive efficiency was found to be 0.41 of the natural frequency of the wing.

It should be stressed again that the current analysis on the scaling is strictly valid only in the flow regimes where the force on the wing is proportional to the acceleration of the wing, such as the acceleration-reaction force term or the inertia force. Further study, see also Section 6.3, should reveal the applicability of the current scaling or extension of the current analysis in the parameter space at lower Reynolds numbers, such as at Re = 100 or at lower reduced frequencies, e.g. $k \leq 0.5$. By modeling the wing as a linear beam, a relationship between the time-averaged force normalized by the effective stiffness and the maximum wing tip deformation relative to the imposed kinematics is established by considering the energy balance of the wing. Furthermore, the lift generation of insect flyers, approximated by its weight, largely follows the same scaling relationship. Similar scaling analysis are performed for the power input and propulsive efficiency. The chosen scaling parameters, given as a combination of *a priori* known wing geometry, structural properties, and motion amplitude and frequency, helps to gain more insight in the combined fluid and structural dynamics and is applicable to a wide range of scenarios involving different motion types, Reynolds numbers, and the fluid media regarding the magnitude of the time-averaged force, which has the potential to guide the design of flapping wing micro air vehicles.

6.2 Main Contributions

The main contributions of this dissertation are:

(i) The development of fluid-structure interaction framework that couples parallelized unstructured pressured-based finite volume Navier-Stokes equation solver to structural dynamics solver. This framework is based on a time-domain partitioned solution process in which the nonlinear partial differential equations governing the fluid and the structure are solved independently and spatially coupled through an interface using an implicit algorithm, such that both equations are synchronized.

(ii) Implementation of Radial Basis Function Interpolation methods to remesh the computational fluid dynamics mesh to account for large displacement motion of a wing.

(iii) Systematic dimensional analysis and non-dimensionalization of the governing equations and the kinematics to provide systematic framework to analyze fluid-structure interaction of a flexible flapping wing.

(iv) Scaling of forces acting on a moving body immersed in a fluid by considering control volume analysis of the fluid momentum conservation [125,127]

(v) Investigation of fluid dynamics of pitching and plunging airfoil motion at high Reynolds number of $O(10^4)$, low reduced frequency (0.25), and low Strouhal number (0.04) regime.

(vi) Numerical computations of flexible wing configurations at relative high Reynolds number $O(10^3 - 10^4)$, high reduced frequency $O(1)$, and high Strouhal number $O(1)$ that show good correlation to the experimental results reported in the literature.

(vii) Scaling of the propulsive force generation and the propulsive efficiency at relative high Reynolds number $O(10^3 - 10^4)$, high reduced frequency $O(1)$, and high Strouhal number $O(1)$.

(viii) Determined optimal frequencies for the propulsive force generation and the propulsive efficiency that is consistent with the values report in the literature.

6.3 Future Work

The current scaling considers only the bending motion for purely plunging wings. Further analysis is planned to include twist and active or passive pitching motion, that may enhance the force generation and the efficiency more as observed from the biological flyers. Another aspect of the biological flyers that is not included in this dissertation is the anisotropic wing nature: as discussed by Combes and Daniels [70] the chordwise flexibility is order of magnitude smaller than the spanwise flexibility. Also, the leading edge of the wing is often stiffened. Combination of these two anisotropic aspects requires more advanced description of the system, such as being in two-dimensions in space and coupling between chordwise and spanwise flexibilities to name a few. This is in particular interesting for the hovering motions in air, such as insect flights, for which the efficiency scaling predicts a very low propulsive efficiency, compared to the forward motion in water.

Furthermore, the flight performance under more realistic flight conditions, such as wind gust and insect wing kinematics will be investigated. Another important aspect of the aerodynamic performance for MAV development is the role of the body, which is neglected in many studies including the current dissertation. Including the body-wing interaction is the first step towards the fully coupled dynamics of a flapping MAV flyer and its effect will be modeled and assessed in the future. It will also be interesting to see if the current scaling for force generation of flexible wings can be extrapolated to the FSI systems in lower Reynolds number regimes of $O(2)$, where the interaction between the resulting force and the vortices in the flow field might play a more dominant role.

This dissertation mainly discusses the role of flexibility on the time-averaged measures and simplifications were made to enable analysis regarding detailed time evolution of the force generation, such as the relation between the lift and the thrust. The results obtained for the scaling of power input, that was estimated by considering the deformed motion of the wing, strongly attracts to look at the lift generation by considering the acceleration of the wing under deformation following the proposed scaling of forces in Section 3.2 that the acceleration-reaction force would dominate at high reduced frequency, high Reynolds number regimes. Furthermore, by considering passive pitch motion arising due to the wing tip deformation relative to the wing root, could be incorporated into a quasi-steady model for lift such as Theodorsen's shown in Eq. (38), together with the effects from the effective angle of attack, that may result in a more accurate representation of the combined fluid and structural dynamics. Then, based on this result, instantaneous thrust may be predicted, leading to instantaneous propulsive efficiency model.

Still open question is the relation between the aerodynamics shown by a flexible wing and its rigid counterpart. A wing is assumed to be rigid if the deformation of the wing due to the aerodynamic force or its own inertia force is negligible. Equivalence of this statement for the scaling analysis shown in this dissertation is that the ratio between the effective stiffness and the effective inertia, $\Pi_1/\Pi_0 \sim f_1/f \rightarrow 0$, which is also the same as $\gamma \rightarrow 0$. Will the limit of $\gamma \rightarrow 0$ in the analysis result in the aerodynamics that is evinced by the rigid wings? By answering this question the scaling analysis presented in this dissertation will be more rigorous and our insight in the flexibility wing and rigid wing aerodynamics will be enhanced.

Moreover, from the numerical analysis point of view, a study is planned to investigate the role of flexibility on the FSI-stability and convergence. In the current framework where a NS-solver is coupled to a structural dynamics solver through an interface with the implicit coupling scheme, it is still unclear when a FSI-convergence scheme, such as Aitken's relaxation is needed, or how to accelerate the convergence. This numerial aspect will be more critical for the works planned for future that includes three-dimensional viscous flow computation over a largely deforming composite wing that inheritantly will introduce multi-scale displacements of each point in the wing depending on the local stiffness and inertia, one or couple of extra FSI-subiteration can be very expensive in terms of the computational cost.

Finally, this study also illustrates the need for collaborative work among the experimentalists and computational modelists. By investigating the physics for the equally defined cases the applied methods can be validated independently and the uncertainties related to the experimental setup and measurement techniques as well as computational modeling can be quantified.

Appendix A.

Spatial and Temporal Sensitivity Studies

A.1 Pitching and Plunging SD7003 at $Re = 6\times10^4$, $k = 0.25$, $St = 0.04$.

The numerical solutions are computed in open bounded domain on a unstructured grid with 46281 cells, see Figure A-1. The outer boundaries of the computational domain are 50 chord lengths apart. The boundary conditions are as follows: on the airfoil no-slip conditions are imposed; the outer boundaries are incompressible inlets; and the inlet turbulence intensity is 0.5%. The computations are run assuming fully-turbulent, with no attempt to model transition.

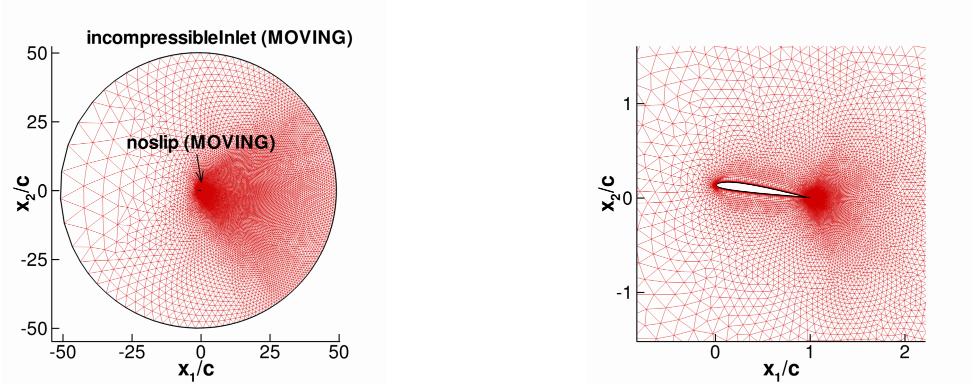

(a) SD7003 airfoil in open bounded domain

(b) Mixed elements near the SD7003 airfoil

Figure A-1. Unstructured grid in open bounded domain (a) and its grid distribution near the airfoil (b) for oscillating SD7003 airfoil

Spatial and temporal sensitivity tests were performed for the pitching and plunging case at $Re = 6\times10^4$, $k = 0.25$, and $St = 0.04$. To assess the grid sensitivity time histories of lift coefficient on the baseline (46281 cells), finer (119951 cells) and the finest (368099 cells) grids are compared in Figure A-1(a) using a time step of $T/dt =$

400. Note that all non-dimensional variables will be written explicitly for clarity in this Chapter. All three solutions coincide and thus all subsequent computations are performed on the baseline grid. To investigate temporal sensitivity, three time steps were used: T/dt = 400, 800, and 1600. Figure A-1(b) shows that the computations using T/dt = 400 on the grid with 46281 cells is sufficient to obtain grid and time step independent solution.

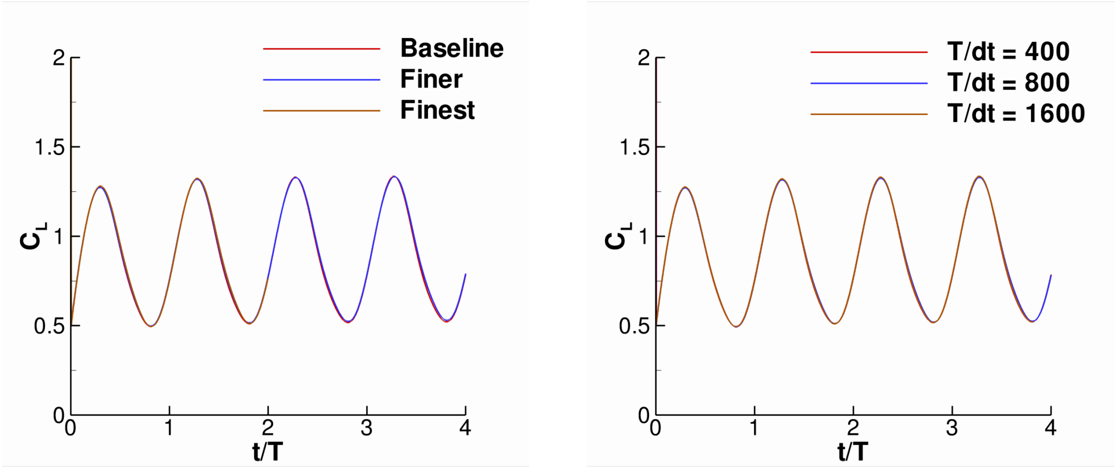

(a) Spatial sensitivity (b) Time step sensitivity

Figure A-2 (a) Time histories of the lift coefficients using the baseline (46281 cells), finer (119951 cells), and the finest (368099 cells) grid using T/dt = 400 over pitching and plunging SD7003 airfoil at Re = 6×10^4, k = 0.25, and St = 0.04. (b)Time history of the lift coefficients using T/dt = 400, 800, and 1600 of a pitching and plunging SD7003 airfoil at Re = 6×10^4, k = 0.25, and St = 0.04 on the baseline grid.

A.2 Pitching and Plunging Flat Plate at $Re = 6\times10^4$, $k = 0.25$, $St = 0.04$.

Spatial and temporal sensitivity tests for the SD7003 airfoil are shown in Section A.1. The solution for the pitching and plunging SD7003 airfoil with 46281 cells using T/dt = 480 is shown to be grid and time independent. In all computations the time step of T/dt = 480 have been used. For the pitching and plunging flat plate the spatial sensitivity test is investigated at Re = 6×10^4, k = 0.25, and St = 0.04. To assess the grid sensitivity for the flat plate time histories of lift coefficient on the baseline (9624 cells), finer (32204 cells) and the finest (65904 cells) grids are compared using a time step of T/dt = 480, see Figure A-4. All three solutions stay within maximum relative error of

2%, with the relative error between the finer and the finest grid smaller than between the baseline and the finer grid. Based on this observation, the finer grid has been chosen for all subsequent computations for the flat plate.

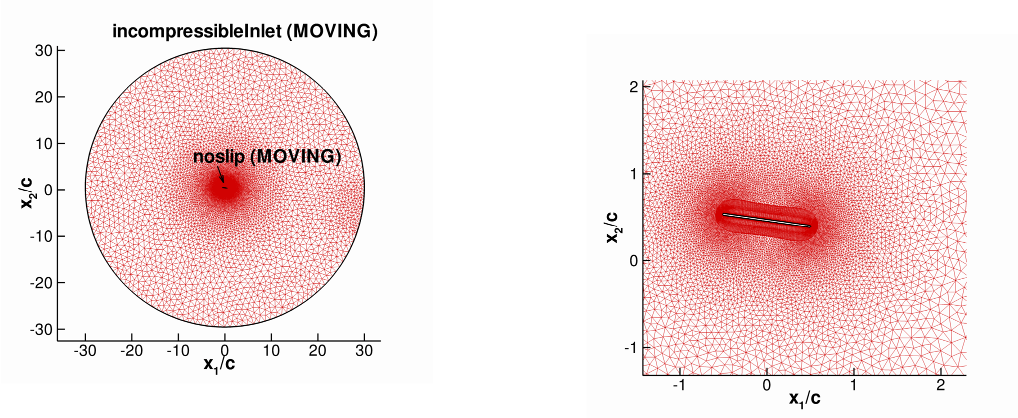

(a) Flat plate in open bounded domain **(b) Mixed elements near the flat plate**

Figure A-3 Computational mesh for the flat plate.

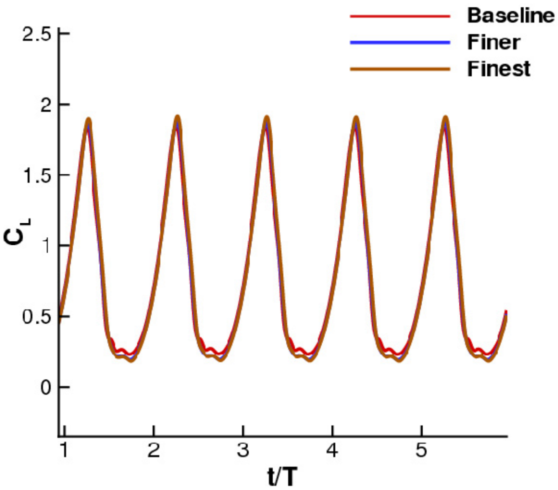

Figure A-4 Time histories of the lift coefficients using the baseline (9624 cells), finer (32204 cells), and the finest (65904 cells) grid using = 480 over pitching and plunging two-dimensional flat plate at = 6×10^4, = 0.25, and = 0.04.

A.3 Plunging Chordwise Flexible Airfoil in Water at $Re = 9\times10^3$

Unstructured grids around an airfoil with a rigid teardrop and a flexible flatplate are utilized to solve for the flow field. In order to identify the suitable number of grid points and the time step, grid and time step sensitivity analyses are performed for the rigid airfoil at St = 0.17. From the results shown in Figure A-5, the *Intermediate* grid (25×10^3) and T/dt = 480 are chosen. As to the prescribed wing motion, the rigid teardrop is actuated by a sinusoidal plunge displacement with the normalized amplitude of 0.194. The fluid dynamics computation is assumed to be fully turbulent and the Menter's SST turbulence model is used. The y^+ of the first grid spacing is set to be of the order of $O(1)$. For the outer boundary conditions, located at 25 chords away from the airfoil, the freestream velocity, density, and turbulence quantities are assigned. On the airfoil surface the noslip condition is imposed. In order to compute the wing deformations, a finite element Euler-Bernoulli beam model with 51 nodes is utilized.

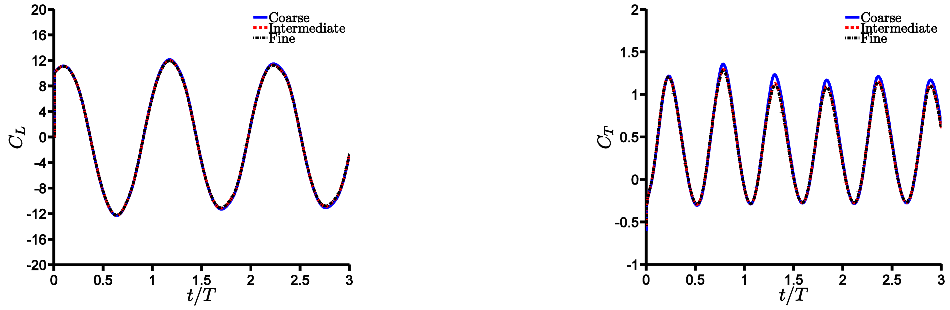

(a) lift coefficient (b) thrust coefficient

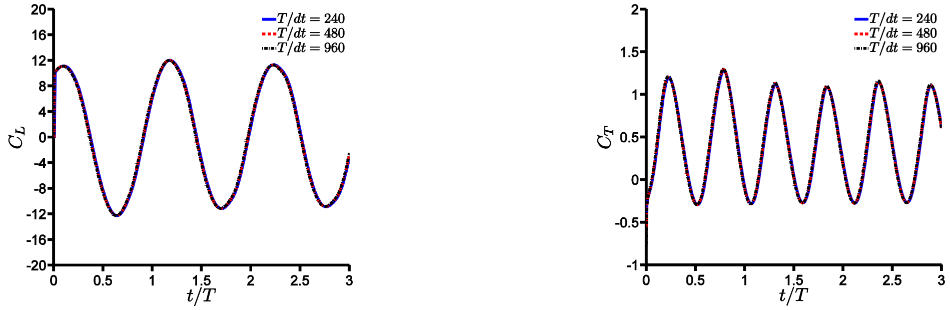

(c) lift coefficient (d) thrust coefficient

Figure A-5 Temporal and spatial sensitivity analyses for a rigid plunging airfoil at St = 0.17. Grid sizes are *Coarse*: 6×10^3, *Intermediate*: 25×10^3, and *Fine*: 100×10^3 cells.

A.4 Plunging Spanwise Flexible Wing in Water at Re = 3×10^4,

Unstructured grids around a rectangular wing of a NACA0012 airfoil with AR = 3 are utilized to solve for the flow field. In order to identify the suitable number of grid points and the time step, grid and time step sensitivity analyses are performed for the rigid wing. From the results shown in Figure A-6, the *Intermediate* grid (0.31×10^6 cells) and T/dt = 500 are chosen. As to the prescribed wing motion, the wing root is actuated by a sinusoidal plunge displacement with the normalized amplitude of 0.175. The fluid dynamics computation is assumed to be fully turbulent and is solved using the Menter SST turbulence model. The y^+ of the first cell away from the wing is set to be of the order of $O(1)$. For the outer boundary conditions, located around 20 chords away in radial direction from the wing and 9 chords from the wing tip, the freestream velocity, density, and turbulence quantities are assigned. On the wing surface the noslip condition is imposed. In order to compute the wing deformations, a triangle facet shell finite-element discretization with 768 elements is utilized. The degrees of freedom of the node relevant to the chordwise displacement are constrained since Heathcote, Wang, and Gursul [76] observed that the degree of chordwise flexion of the wing for all wings and all motion frequencies was negligible. In addition, the contribution of the poludimethysiloxane (PDMS) rubber material which was used in the experimental wing configuration to the overall mass and stiffness properties is assumed to be negligible; therefore only the stainless steel for the *Flexible* wing with ρ^* = 7.8 and Π_1 = 212 and the *Very Flexible* wing with ρ^* = 2.7 and Π_1 = 38 is considered. Note that the material properties of the *Very Flexible* wing are based on a static bending test (private communications with Drs. Wang and Gursul at University of Bath).

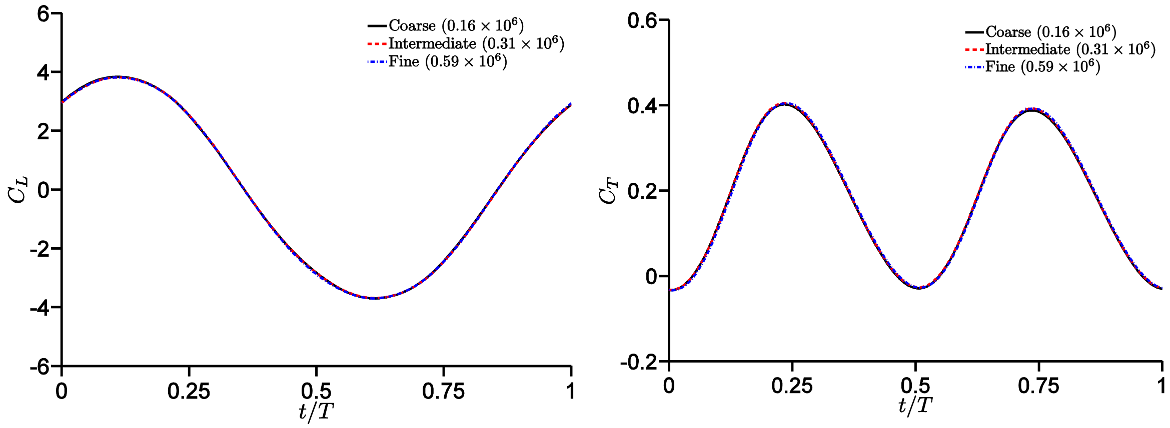

(a) lift coefficient (b) thrust coefficient

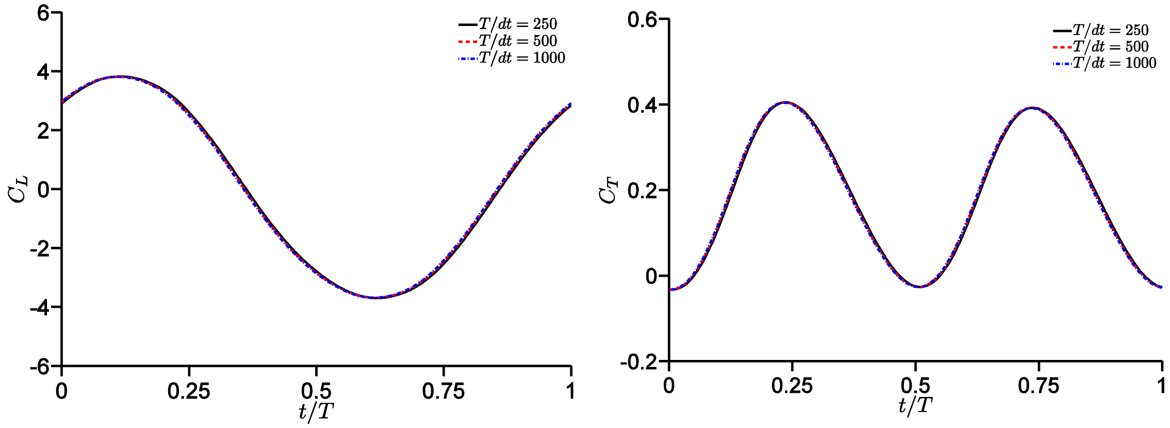

(c) lift coefficient (d) thrust coefficient

Figure A-6 Temporal and spatial sensitivity analyses for a rigid plunging NACA0012 wing at *k* = 1.82. Grid sizes are *Coarse*: 0.16×10^6, *Intermediate*: 0.31×10^6, and *Fine*: 0.59×10^6 cells.

A.5 Flapping Zimmerman Wing in Air at Re = 1.5×10^3,

To assess the grid size sensitivity three grids with different spatial resolutions around a Zimmerman wing are utilized for the fluid dynamic computation. The mesh to solve for the fluid equations consists of mixed brick near the wing and tetrahedral cells away from the wing. For the time step sensitivity analysis 250, 500, and 1000 time steps per motion cycle were chosen. The computational fluid dynamics (CFD) and the computational structural dynamics' (CSD) grid configurations are shown in Figure A-7. From the results shown in Figure A-8, the intermediate grid with 0.51×10^6 nodes and 500 time steps per motion cycle show grid and time step independent solution. The fluid flow is assumed to be laminar. The first grid spacing from the wing surface is set to 2.5×10^{-3} and the outer boundary of the computational grid is located at 30 chords away from the wing. At the outer computational boundary zero velocity and reference density are assigned. On the wing surface the noslip condition is applied. In order to compute the wing deformations, a triangle facet shell finite-element discretization with 767 elements is used.

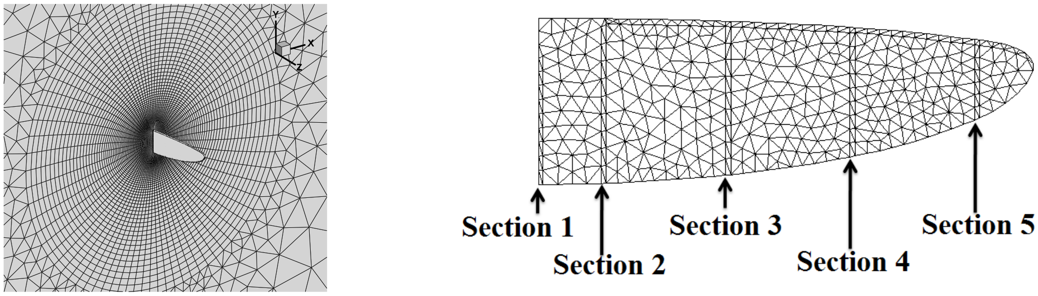

(a) CFD mesh (b) CSD mesh

Figure A-7 Computational grids for the isotropic Zimmerman wing in flap motion.

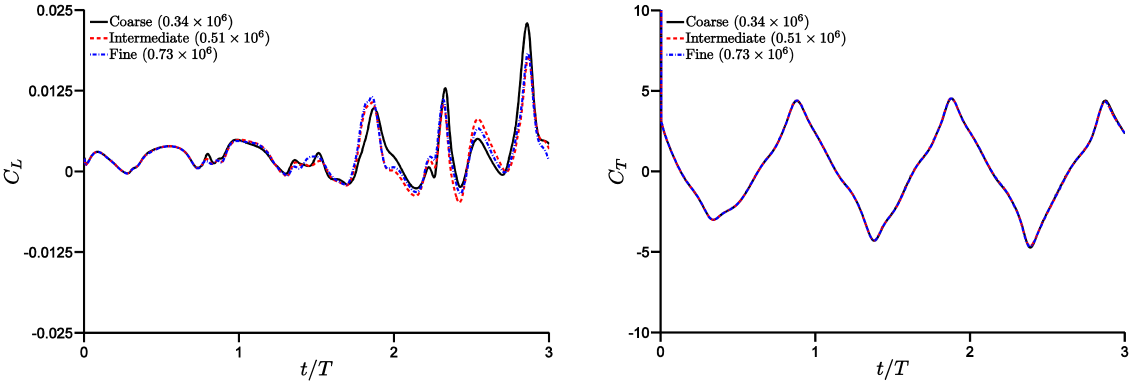

(a) lift coefficient

(b) thrust coefficient

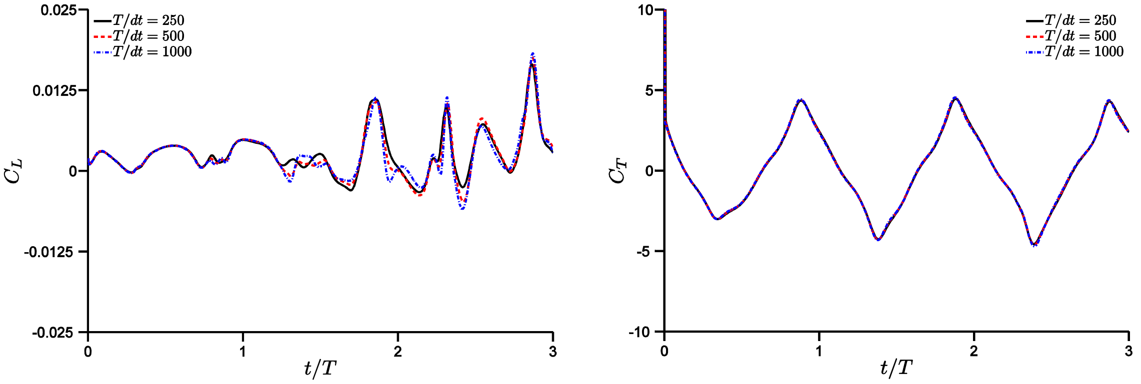

(c) lift coefficient

(d) thrust coefficient

Figure A-8 Temporal and spatial sensitivity analyses for a rigid flapping Zimmerman wing at $Re = 1.5\times10^3$, $k = 0.56$, and $St = 0.25$.

Appendix B.

Training and Testing Points in the Design of Experiment of the Hovering Zimmerman Wing Case

Tabel B-1 shows the lift of training and testing pointes in the design space for the flapping isotropic Zimmerman wing in hover in air (Section 5.2.3). The Π_1 and ρ^* are the design variables. In the computations the Young's moduli and the density of the wing are varied.

Different weighting strategies are employed to minimize the risk of generating surrogates that fit the training data well but perform less in other regions. The weighted average surrogates (WAS) use constant weights, meaning that a certain surrogate will have the same importance throughout the design space. The Polynomial Response Surface, Kriging, and Support Vector Regression are used for the individual surrogates, after which each surrogate is weighted in correlation to the RMS PRESS values, defined as

$$\text{RMS PRESS} = \sqrt{\frac{1}{N_s}\sum_{i=1}^{N_s}\left(y_i - \hat{y}_i^{(-i)}\right)}, \tag{97}$$

where $\hat{y}_i^{(-i)}$ is the prediction at $x^{(i)}$ using a surrogate model constructed with all training point except $x^{(i)}$, and N_s is the number of training points. Table B-2 shows the RMS PRESS values as predicted by the individual surrogate models $\langle C_L\rangle$, ψ, and θ. The cells with underlines indicate the lowest RMS PRESS values and the surrogates that are weighted in the WAS.

Table B-1 List of training points $(1-14)$ and testing points (15, 16) in the design space for the flapping isotropic Zimmerman wing at Re = 1.5×10^3 and k = 0.56 hovering in air. Π_1 and ρ^* are the design variables.

Case Nr.	Π_1	ρ^*	E	ρ_s
1	1.0×10^{2}	1.00×10^{1}	2.00×10^{8}	1.23×10^{1}
2	1.04×10^{5}	1.00×10^{1}	2.00×10^{11}	1.23×10^{1}
3	1.04×10^{5}	1.00×10^{4}	2.00×10^{11}	1.23×10^{4}
4	1.00×10^{3}	1.00×10^{3}	1.92×10^{9}	1.23×10^{3}
5	3.29×10^{3}	3.16×10^{2}	6.32×10^{9}	3.89×10^{2}
6	1.04×10^{5}	3.16×10^{2}	2.00×10^{11}	3.89×10^{2}
7	3.29×10^{3}	1.00×10^{1}	6.32×10^{9}	1.23×10^{1}
8	4.38×10^{4}	2.19×10^{3}	8.41×10^{10}	2.69×10^{3}
9	1.00×10^{4}	1.00×10^{2}	1.92×10^{10}	1.23×10^{2}
10	3.16×10^{2}	3.16×10^{1}	6.07×10^{8}	3.89×10^{1}
11	1.00×10^{2}	1.00×10^{2}	2.00×10^{8}	1.23×10^{2}
12	1.00×10^{3}	1.00×10^{2}	1.92×10^{9}	1.23×10^{2}
13	1.00×10^{4}	1.00×10^{3}	1.92×10^{10}	1.23×10^{3}
14	1.00×10^{4}	1.00×10^{4}	1.92×10^{10}	1.23×10^{4}
15	5.86×10^{2}	3.06×10^{2}	1.13×10^{9}	3.77×10^{2}
16	3.78×10^{3}	5.72×10^{1}	7.26×10^{9}	7.04×10^{1}

Table B-2 RMS PRESS values as predicted by the individual surrogate models for the lift, twist, and bending angle. Surrogate models indicated by the underlines are used for the WAS construction.

$[10^{-1}]$	KRG	PRS	SVR1	SVR2	SVR3	SVR4	SVR5	SVR6
$\langle C_T \rangle$	3.56	3.57	2.93	2.23	2.54	5.57	2.44	2.38
ψ	3.65	6.65	2.77	2.47	2.64	2.67	1.98	2.35
θ	3.63	3.62	2.63	2.05	2.51	2.53	1.32	2.47

Finally, the error measured at the independent testing points defined as the relative difference between the constructed WAS and the actual values from the simulations with respect to the range of the objective functions show, see Table B-3, that for the case 15 where the high gradients in the surrogates are located has larger error than for the more stiffer case 16.

Table B-3 Relative error at the independent testing points 15 and 16. The difference in the value predicted by the surrogate model and the numerical computations are normalized by the range of the surrogate response

Objective function	Relative error at testing point 15 (%)	Relative error at testing point 16 (%)
$\langle C_T \rangle$	23	8
θ	15	5
ψ	7	5

Appendix C.

Modal analysis of isotropic Zimmerman wing

Natural frequencies are computed using MSC.Marc and shown in Table C-1. Moreover, the mode shapes of the wing for each natural frequency are illustrated in Figure C-1. The first mode is related to the spanwise bending of the wing and the second mode the twist of the wing. Note that all the natural frequencies listed in Table C-1 are higher than the motion frequency of 10 Hz.

Table C-1 First two natural frequencies in Hz based on a modal analysis for the training and testing points in the design space for flapping isotropic Zimmerman wings at Re=1.5×10^3 and k = 0.56 in still air.

Case	Mode 1	Mode 2
1	7.46×10^1	3.04×10^2
2	2.36×10^3	9.61×10^3
3	7.46×10^1	3.04×10^2
4	2.31×10^1	9.41×10^1
5	7.46×10^1	3.04×10^2
6	4.19×10^2	1.71×10^3
7	4.19×10^2	1.71×10^3
8	1.03×10^2	4.21×10^2
9	2.31×10^2	9.41×10^2
10	7.31×10^1	2.98×10^2
11	2.36×10^1	9.61×10^1
12	7.31×10^2	2.98×10^2
13	7.31×10^1	2.98×10^2
14	2.31×10^2	9.41×10^2

15	3.20×10^{1}	1.31×10^{2}
16	1.88×10^{2}	7.65×10^{2}

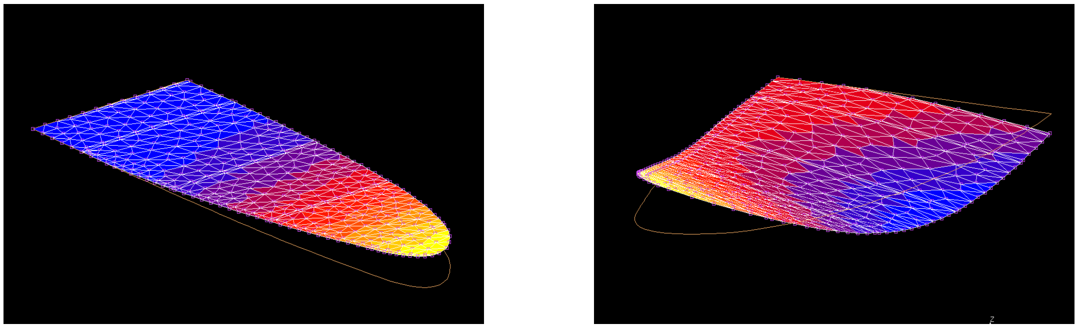

Mode 1

Mode 2

Figure C-1. Snapshots of the wing shapes for the first four modes based on a modal analysis for the training and testing points in the design space for the flapping isotropic Zimmerman wing at $=1.5\times10^{3}$ and $= 0.56$ in still air.

Bibliography

[1] T Reichert, C Robertson, and J. D. DeLaurier. (2010, Sep.) Human-powered Ornithopter Becomes First Ever to Achieve Sustained Flight. [Online]. http://www.engineering.utoronto.ca/About/Engineering_in_the_News/Human-powered_Ornithopter_Becomes_First_Ever_to_Achieve_Sustained_Flight.htm

[2] T.J. Muller, *Fixed and Flapping Wing Aerodynamics for Micro Air Vehicle Applications*. New York: AIAA, 2002.

[3] W. Shyy, Y. Lian, J. Tang, D. Viieru, and H. Liu, *Aerodynamics of Low Reynolds Number Flyers*.: Cambridge Univ Press, 2008.

[4] W. Shyy, M. Berg, and D. Ljungqvist, "Flapping and Flexible Wings for Biological and Micro air Vehicles," *Progress in Aerospace Sciences*, vol. 24, no. 5, pp. 455 - 505, 1999.

[5] D. Floreano, J.-C. Zufferey, M. Srinivasan, and C. Ellington, *Flying Insects and Robots*. Berlin, Germany: Springer-Verlag, 2009.

[6] W. Shyy, H. Aono, S. K. Chimakurthi, P. Trizila, C.-K. Kang, C. E. S. Cesnik, and H. Liu, "Recent progress in flapping wing aerodynamics and aeroelasticity," *Progress in Aerospace Sciences*, vol. 46, no. 7, pp. 284-327, 2010.

[7] Aerovironment. (2011, Feb.) Aerovironment Inc. [Online]. http://www.avinc.com/nano

[8] Festo. (2011, Mar.) Festo. [Online]. http://www.festo.com/cms/en_corp/11369.htm

[9] K. M. E. de Clercq, R. de Kat, B. Remes, B. W. van Oudheusden, and H. Bijl, "Flow Visualization and Force Measurements on a Hovering Flapping-Wing MAV," in *39th AIAA Fluid Dynamics Conference, San Antonio, Texas, 22-25 June 2009*, AIAA-2009-4035.

[10] R. J. Wood, "The First Takeoff of a Biologically Inspired At-Scale Robotic Insect," *IEEE Transactions on Robotic*, vol. 24, no. 2, pp. 341 - 347, 2008.

[11] G.C.H.E. de Croon, K.M.E. de Clerq, R. Ruijsink, B. Remes, and C. de Wagter, "Design, aerodynamics, and vision-based control of the DelFly," *In the*

International Journal of Micro Air Vehicles, vol. 1, no. 2, pp. 71 - 97, 2009.

[12] A. Azuma, *The Biokinetics of Flying and Swimming*, 2nd ed. Virginia: AIAA, Inc., 2006.

[13] U. M. Norberg, *Vertebrate Flight: Mechanics, Physiology, Morphology, Ecology, and Evolution*. New York: Springer, 1990.

[14] R. Dudley, *The Biomechanics of Insect Flight: Form, Function, Evolution*. New Jersey: Princeton University Press, 2002.

[15] A.A. Biewener, *Animal Locomotion*. New York: Oxford University Press, 2003.

[16] T. Weis-Fogh, "Quick Estimates of Flight Fitness in Hovering Animals, including Novel Mechanism for Lift Production," *Journal of Experimental Biology*, vol. 59, pp. 169 - 230, 1973.

[17] T. Maxworthy, "The fluid dynamics of insect flight," *Annual Review of Fluid Mechanics*, vol. 13, pp. 329 - 350, 1981.

[18] S.P Sane, "The Aerodynamics of Insect Flight," *Journal of Experimental Biology*, vol. 206, pp. 4191 - 4208, 2003.

[19] B.W. Tobalske, "Biomechanics of Bird Flight," *Journal of Experimental Biology*, vol. 210, pp. 3135 - 3146, 2007.

[20] Z.J. Wang, "Dissecting Insect flight," *Annual Review of Fluid Mechanics*, vol. 37, pp. 183 - 210, 2005.

[21] R.J. Cooter and P.S. Baker, "Weis-fogh Clap and Fling Mechanisms in Locusta," *Nature*, vol. 269, pp. 53 - 54, 1977.

[22] K.G. Götz, "Course-control, Metabolism and Wing Interference during Ultralong tethered flight in Drosophila Melangaster," *Journal of Experimental Biology*, vol. 161, pp. 77 - 95, 1991.

[23] A.K. Brodsky, "Vortex Formation in the Tethered Flight of the Peacock Butterfly Inachis Io and Some Aspects of Insect Flight Evolution," *Journal of Experimental Biology*, vol. 161, pp. 77 - 95, 1991.

[24] J. Brachenbury, "Wing Movements in the Bush Cricket Tettigonia viridissima and the mantis Ameles Spallanziana during Natural Leaping," *Journal of Zoology Long*, vol. 220, pp. 593 - 602, 1990.

[25] R.B. Srygley and A.L.R. Thomas, "Unconventional Lift-generating Mechanisms in Free-flying Butterflies," *Nature*, vol. 420, pp. 660 - 664, 2002.

[26] F.-O. Lehmann, S.P. Sane, and M.H. Dickinson, "The Aerodynamic Effects of Wing-Wing Interaction in Flapping Insect Wings," *Journal of Experimental Biology*, vol. 208, pp. 3075 -- 3092, 2005.

[27] M.H. Dickinson, F.-O. Lehmann, and S.P. Sane, "Wing Rotation and the Aerodynamic Basis of Insect Flight," *Science*, vol. 284, no. 5422, pp. 1954 - 1960, 1999.

[28] J.M. Birch and M.H. Dickinson, "The Influence of Wing-wake Interactions on the Productions of Aerodynamic Forces in Flapping Flight," *Journal of Experimental Biology*, vol. 206, pp. 2257 - 2272, 2003.

[29] W. Shyy, P. Trizila, C.-K. Kang, and H. Aono, "Can Tip Vortices Enhance Lift of a Flapping Wing?," *AIAA Journal*, vol. 47, pp. 289 - 293, 2009.

[30] C.P. Ellington, C. van der Berg, A.P. Willmott, and A.L.R. Thomas, "Leading-edge Vortices in Insect Flight," *Nature*, vol. 384, pp. 626 - 630, 1996.

[31] C. van den Berg and C.P. Ellington, "The Three-dimensional Leading-edge Vortex of a 'Hovering' Model Hawkmoth," *Philosophical Transactions of the Royal Society B: Biological Sciences*, vol. 352, pp. 329 - 340, 1997.

[32] C. van den Berg and C.P. Ellinton, "The vortex Wake of a 'Hovering' Model Hawkmoth," *Philosophical Transactions of the Royal Society B: Biological Sciences*, vol. 352, pp. 317 - 328, 1997.

[33] H. Liu and K. Kawachi, "A Numerical Study of Insect Flight," *Journal of Computational Physics*, vol. 146, no. 1, pp. 124 -- 156, 1997.

[34] H. Liu, C.P. Ellington, K. Kawachi, C. van den Berg, and A.P. Willmott, "A Computational fluid Dynamic Study of Hawkmoth Hovering," *Journal of Experimental Biology*, vol. 201, pp. 461 - 477, 1998.

[35] W. Shyy and H. Liu, "Flapping Wings and Aerodynamic Lift: The Role of Leading-Edge Vortices," *AIAA Journal*, vol. 45, pp. 2817 - 2819, 2007.

[36] H. Liu and H. Aono, "Size Effects on Insect Hovering Aerodynamics: an Integrated Computational Study," *Bioinspired Biomimetics*, vol. 4, pp. 1 - 13, 2009.

[37] J.D. Anderson, *Fundamentals of Aerodynamics*, 4th ed. New York: McGraw Hill Higher Education, 2006.

[38] R. Ramamurti and W.C. Sandberg, "A Computational Investigation of the Three-dimensional Unsteady Aerodynamics of Drophila Hovering and Maneuvering," *Journal of Experimental Biology*, vol. 210, pp. 881 - 896, 2007.

[39] H. Aono, F. Liang, and H. Liu, "Near- and Far-field Aerodynamic in Insect Hovering Flight: an Integrated Computational Study," *Journal of Experimental Biology*, vol. 211, pp. 239 -- 257, 2008.

[40] M.J. Ringuette, M. Milano, and M. Gharib, "Role of the Tip Vortex in the Force Generation of Low-aspect-ratio Normal Flat Plates," *Journal of Fluid Mechanics*, vol. 581, pp. 453 -- 468, 2007.

[41] K. Taira and T. Colonius, "Three-dimensional Flows around Low-aspect Ratio Flat-plate wings at Low Reynolds Numbers," *Journal of Fluid Mechanics*, vol. 623, pp. 187 - 207, 2009.

[42] A.R. Ennos, "Inertial and Aerodynamic Torques on the wings of Diptera in Flight," *Journal of Experimental Biology*, vol. 142, pp. 87 -- 95, 1989.

[43] D. Ishihara, T. Horie, and M. Denda, "A two-dimensional computational study on the fluid-structure interaction cause of wing pitch changes in dipteran flapping flight," *Journal of Experimental Biology*, vol. 212, no. 1, pp. 1-10, 2009.

[44] L. Zhao, Q. Huang, X. Deng, and S. P. Sane, "Aerodynamic effects of flexibility in flapping wings," *Journal of Royal Society Interface*, vol. 7, no. 44, pp. 485-497, 2010.

[45] J. Zhang, N.-S. Liu, and X.-Y. Lu, "Locomotion of a passively flapping flat plate," *Journal of Fluid Mechanics*, vol. 659, pp. 43 - 68, 2010.

[46] R. Godoy-Diana, J.-L. Aider, and J.E. Wesfried, "Transitions in the Wake of a Flapping Foil," *Physical Review E*, vol. 77, p. 016308, 2008.

[47] R. Godoy-Diana, C. Marias, J.-L. Aider, and J.E. Wesfried, "A Model For the Symmetry Breaking of the Reverse Benard-von Karman Vortex Street Produced by a Flapping Foil," *Journal of Fluid Mechanics*, vol. 622, pp. 23 - 32, 2009.

[48] J.-S. Lee, J.-H. Kim, and C Kim, "Numerical Study on the Unsteady-Force-Generation Mechanism of Insect Flapping Motion," *AIAA Journal*, vol. 26, no. 7, pp. 1835-48, 2008.

[49] J.M. Anderson, K. Streitlin, D.S. Barrett, and M.S. Triantafyllou, "Oscillating Foils of High Propulsive Efficiency," *Journal of Fluid Mechanics*, vol. 360, pp. 41 - 72, 1998.

[50] D.G. Bohl and M.M. Koochesfahani, "MTV Measurements of the Vortical Field in the Wake of an Airfoil Oscillating at High Reduced Frequency," *Journal of Fluid Mechanics*, vol. 620, pp. 63 - 88, 2009.

[51] D.A. Read, J.S. Hover, and M.S. Triantafyllou, "Forces on Oscillating Foils for Propulsion and Maneuvering," *Journal of Fluids and Structures*, vol. 17, pp. 163 - 93, 2003.

[52] F.S. Hover, O. Haugsdal, and M.S. Triantafyllou, "Effect of Angle of Attack Profiles in Flapping Foil Propulsion," *Journal of Fluids and Structures*, vol. 19, pp. 37 -- 47, 2004.

[53] L. Schouveiler, F.S. Hover, and M.S. Triantafyllou, "Performance of Flapping Foil Propulsion," *Journal of Fluids and Structures*, vol. 20, pp. 949--59, 2005.

[54] J.C.S. Lai and M.F. Platzer, "Jet Characteristics of a Plunging Airfoil," *AIAA Journal*, vol. 37, no. 12, pp. 1529 -- 37, 1999.

[55] G.C. Lewing and H. Haj-Hariri, "Modeling Thrust Generation of a Two-dimensional Heaving Airfoil in a Viscous Flow," *Journal of Fluid Mechanics*, vol. 492, pp. 339 -362, 2003.

[56] K.B. Lua, T.T. Lim, and K.S., Oo, G.Y. Yeo, "Wake-structure Formation of a Heaving Two-dimensional Ellipti Airfoil," *AIAA Journal*, vol. 45, no. 7, pp. 1571 -- 1583, 2007.

[57] M. Ol and et al., "Unsteady Aerodynamics for Micro Air Vehicle," RTO AVT-149, 2009.

[58] Y.S. Baik, J. Rausch, L. Bernal, and M. Ol, "Experimental Investigation of Pitching and Plunging Airfoils at Reynolds Number between 1x10^4 and 6x10^4," in *39th AIAA Fluid Dynamics Conference, San Antonio, Texas, June 22-25, 2009*, AIAA-2009-4030.

[59] Y.S. Baik, J. Rausch, L. Bernal, W. Shyy, and M.V. Ol, "Experimental Study of Governing Parameters in Pitching and Plunging Airfoils at Low Reynolds Numbers," in *48th AIAA Aerospace Sciences Meeting Including the New Horizons Forum and Aerospace Exposition, Orlando, Florida, January 4-7, 2010*, AIAA-2010-388.

[60] M. R. Visbal, Gordnier R. E., and M. C. Galbraith, "High-fidelity Simulations of Moving and Flexible Airfoils at Low Reynolds Numbers," *Experiments in Fluids*, vol. 46, pp. 903 - 922, 2009.

[61] G. I. Barenblatt, *Scaling*.: Cambridge University Press, 2003.

[62] G. I. Barenblatt, *Scaling, Self-similarity, and Intermediate Asymptotics*.: Cambridge University Press, 1996.

[63] W.E. Baker, P.S. Westine, and F.T. Dodge, *Similarity Methods in Engineering Dynamics*.: Elsevier, 1991.

[64] R. L. Bisplinghoff, H. Ashley, and R. L. Halfman, *Aeroelasticity*.: Dover publications, inc., 1996.

[65] G.I. Taylor, "The Formation of a Blast Wave by a Very Intense Explosion. II. The Atomic Explosion of 1945," *Proceedings of Royal Society A*, vol. 201, pp. 175 - 186.

[66] S.K. Chimakurthi, "A Computational Aeroelasticity Framework for Analyzing Flapping Wings," University of Michigan, PhD Thesis 2009.

[67] D. Ishihara, Y. Yamashita, T. Horie, S. Yoshida, and T. Niho, "Passive maintenace of high angle of attack and its generation during flapping translation in crane fly wing," *Journal of Experimental Biology*, vol. 212, pp. 3882-3891, 2009.

[68] B. Thiria and R. Godoy-Diana, "How wing compliance drives the efficiency of self-propelled flapping flyers," *Physical Review E*, vol. 82, no. 1, p. 015303, 2010.

[69] S. Ramananarivo, R. Godoy-Diana, and B. Thiria, "Rather than resonance, flapping wing flyers may play on aerodynamics to improve performance," *Proceedings of the National Academy of Sciences*, vol. 108, no. 15, pp. 5964-5969, 2011.

[70] S. A. Combes and T. L. Daniel, "Flexural stiffness in insect wings I. Scaling and the influence of wing venation," *Journal of Experimental Biology*, vol. 206, no. 17, pp. 2979-2987, 2003.

[71] P. Wu, P. Ijfu, and B. Stanford, "Flapping wing structural deformation and thrust correlation study with flexible membrane wings," *AIAA Journal*, vol. 48, no. 9, pp. 2111-2122, 2010.

[72] A. Gogulapati and P. Friedmann, "Approximate Aerodynamic and Aeroelastic Modeling of Flapping Wings in Hover and Forward Flight," in *52nd AIAA/ASME/ASCE/AHS/ASC Structures, Structural Dynamics and Materials Conference 19th AIAA/ASME/AHS Adaptive Structures Conference, Denver, CO, Apr. 4-7, 2011*, vol. AIAA-2011-2008, AIAA-2011-2008.

[73] S. Heathcote and I. Gursul, "Flexible flapping airfoil propulsion at low Reynolds

numbers," *AIAA Journal*, vol. 45, no. 5, pp. 1066-1079, 2007.

[74] P. Gopalakrishnan and D. K. Tafti, "Effect of wing flexibility on lift and thrust production in flapping flight," *AIAA Journal*, vol. 48, pp. 865-877, 2010.

[75] U. Gulcat, "Propulsive Force of a Flexible Flapping Thin Airfoil," *Journal of Aircraft*, vol. 46, no. 2, pp. 465 - 473, 2009.

[76] S. Heathcote, Z. Wang, and I. Gursul, "Effect of spanwise flexibility on flapping wing propulsion," *Journal of Fluids and Structures*, vol. 24, no. 2, pp. 183-199, 2008.

[77] S. K. Chimakurthi, J. Tang, R. Palacios, C. E.S. Cesnik, and W. Shyy, "Computational aeroelasticity framework for analyzing flapping wing micro air vehicles," *AIAA Journal*, vol. 47, pp. 1865-1878, 2009.

[78] J. D. Eldredge, J. Toomey, and A. Medina, "On the roles of chord-wise flexibility in a flapping wing with hovering kinematics," *Journal of Fluid Mechanics*, vol. 659, pp. 94-115, 2010.

[79] W. Zhu, "Numerical simulation of a flapping foil with chordwise or spanwise flexibility," *AIAA Journal*, vol. 45, pp. 2448-2457, 2007.

[80] T. L. Daniel and S. A. Combes, "Flexible wings and fins: bending by inertial or fluid-dynamic forces?," *Integrative and Comparative Biology*, vol. 42, no. 5, pp. 1044-1049, 2002.

[81] S. A. Combes and T. L. Daniel, "Into thin air: contributions of aerodynamic and inertial-elastic forces to wing bending in the hawkmoth Manduca sexta," *Journal of Experimental Biology*, vol. 206, no. 17, pp. 2999-3006, 2003.

[82] H. Masoud and A. Alexeev, "Resonance of flexible flapping wings at low Reynolds number," *Physical Review E*, vol. 81, p. 056304, 2010.

[83] S. Michelin and S.G. Llewellyn Smith, "Resonance and Propulsion Performance of a Heaving Flexible Wing," *Physics of Fluids*, vol. 21, 2009.

[84] S. Sunada, L. Zeng, and K. Kawachi, "The relationship between dragonfly wing structure and torsional deformation," *Journal of Theoretical Biology*, vol. 193, pp. 39 - 45, 1998.

[85] J.-S. Chen, J.-Y. Chen, and Y.-F. Chou, "On the natural frequencies and mode shapes of dragonfly wings," *Journal of Sound Vibration*, vol. 313, pp. 643-654, 2008.

[86] M. Vanella, T. Fitzgerald, S. Preidikman, E. Balaras, and B. Balachandran, "Influence of flexibility on the aerodynamic performance of a hovering wing," *Journal of Experimental Biology*, vol. 212, pp. 95-105, 2009.

[87] W. Shyy, H.S. Udaykumar, M.M. Rao, and R.W. Smith, *Computational fluid dynamics with moving boundaries*. New York, USA: Dover Publications, Inc., 2006.

[88] M. Lesoinne and C. Farhat, "Geometric Conservation Laws for Flow Problems with Moving Boundaries and Deformable Meshes and their Impact on Aeroelastic Computations," *Computational Methods in Applied Mechanics*, vol. 134, pp. 71 - 90, 1996.

[89] R. Mittal and G. Iaccarino, "Immersed boundary method," *Annual Review of Fluid Mechanics*, vol. 37, pp. 239-261, 2005.

[90] J. Katz and A. Plotkin, *Low-speed aerodynamics*.: Cambridge University Press, 2001.

[91] S.A. Ansari, R. Żbikowski, and K. Knowles, "Aerodynamic Modelling of Insect-like Flapping Flight for Micro Air Vehicles," *Progress in Aerospace Sciences*, vol. 42, no. 2, pp. 129 -- 172, 2006.

[92] J. Tang, S. Chimakurthi, R. Palacios, C.E.S. Cesnik, and W. Shyy, "Computational Fluid-Structure Interaction of a Deformable Flapping Wing for Micro Air Vehicle Applications," in *46th AIAA Aerospace Sciences Meeting and Exhibit, Reno, Nevada, Jan. 7-10, 2008*, AIAA-2008-615.

[93] H. Aono, S.K. Chimakurthi, P. Wu, E. Sällström, B.K. Stanford, C.E.S. Cesnik, P. Ifju, L, Ukeiley, and W. Shyy, "A Computational and Experimental Study of Flexible Flapping Wing Aerodynamics," in *48th AIAA Aerospace Sciences Meeting Including the New Horizons Forum and Aerospace Exposition, Orlando, Florida, January 4-7, 2010*, AIAA-2010-554.

[94] S. K. Chimakurthi, C. E. S. Cesnik, and B. Stanford, "Flapping-wing structural dynamics formulation based on a corotational shell finite element," *AIAA Journal*, vol. 49, no. 1, pp. 128-142, 2011.

[95] R. E. Gordnier, P. J. Attar, S. K. Chimakurthi, and C. E. S. Cesnik, "Implicit LES simulations of a flexible flapping wing," in *18th AIAA/ASME/AHS Adaptive Structures Conference, Orlando, FL, 12 - 15 April, 2010*, AIAA-2010-2960.

[96] A. McClung, B. Stanford, and P. Beran, "High-Fidelity Models for the Fluid-Structure Interaction of a Flexible Heaving Airfoi," in *51st AIAA/ASME/ASCE/AHS/ASC Structures, Structural Dynamics, and Materials*

Conference, Orlando, Florida, 2010, AIAA 2010-2959.

[97] B. Stanford, M. Kurdi, P. Beran, and A. McClung, "Shape-Structure, and Kinematic Parameterization of a Power-Optimal Hovering Wing," in *51th AIAA/ASME/ASCE/AHS/ASC Structures, Structural Dynamics, and Materials Conference, Orlando, Florida, 2010*, AIAA-2010-2963.

[98] K. Stein, T. Tezduyar, and R. Benney, "Mesh Moving Techniques for Fluid-Structure Interactions with Large Displacements," *Journal of Applied Mechanics*, vol. 70, pp. 58 -- 63, 2003.

[99] R. W. Smith and J. A. Wright, "A Classical Elasticity-Based Mesh Update Method for Moving and Deforming Meshes," in *48th AIAA Aerospace Sciences Meeting Including the New Horizons Forum and Aerospace Exposition, Orlando, Florida, Jan. 4-7, 2010* , AIAA 2010-164.

[100] A. de Boer, M. S. van der Schoot, and H. Bijl, "Mesh deformation based on radial basis function interpolation," *Computational Structures*, vol. 85, no. 11-14, pp. 784-795, 2007.

[101] T.C.S. Rendall and C.B. Allen, "Unified Fluid-Structure Interpolation and Mesh Motion using Radial Basis Functions," *International Journal for Numerical Methods in Engineering*, vol. 74, pp. 1519-1559, 2008.

[102] T.C.S. Rendall and C.B. Allen, "Efficient Mesh Motion Using Radial Basis Functions with Data Reduction Algorithms," *Journal of Computational Physics*, vol. 228, pp. 6231-6249, 2009.

[103] T.C.S. Rendall and C.B. Allen, "Reduced Surface Point Selection Options for Efficient Mesh Deformation using Radial Basis Functions," *Journal of Computational Physics*, vol. 229, pp. 2810-2820, 2010.

[104] W. Shyy. (2010) Flight InSight. [Online]. http://shyylab.engin.umich.edu/flightinsight

[105] M.S. Triantafyllou, G.S. Triantafyllou, and D.K.P. Yue, "Hydrodynamics of fishlike swimming," *Annual Review of Fluid Mechanics*, vol. 32, pp. 33 -- 53, 2000.

[106] M.S. Triantafyllou, G.S. Triantafyllou, and D.K.P. Yue, "Hydrodynamics of fishlike swimming," *Annual Review of Fluid Mechanics*, vol. 32, pp. 33 - 53, 2000.

[107] J. A. Wright and R. W Smith, "An edge-based method for the incompressible Navier-Stokes equations on polygonal meshes," *Journal of Computational Physics*,

vol. 169, pp. 24-43, 2001.

[108] R. W. Smith and J. A. Wright, "An implicit edge-based ALE method for the incompressible Navier-Stokes equations," *International Journal of Numerical Methods in Fluids*, vol. 43, pp. 253-279, 2003.

[109] R. Kamakoti, S. Thakur, J. Wright, and W. Shyy, "Validation of a new parallel all-speed CFD code in a rule-based framework for multidisciplinary applications," in *36th AIAA Fluid Dynamics Conference and Exhibit, San Francisco, California, June 5-8, 2006*, AIAA-2006-3063.

[110] S. Balay, W. D. Gropp, L. C. McInnes, and B. F. Smith, "Efficient management of parallelism in object oriented numerical software libraries," in *Modern Software Tools in Scientific Computing*, 1997, pp. 163-202.

[111] S. Balay, J. Brown, K. Buschelman, V. Eijkhout, W. D. Gropp, D. Kaushik, M. G. Knepley, L. C. McInnes, B. F. Smith, and H. Zhang, "PETSc Users Manual," Argonne National Laboratory, 2010.

[112] S. Balay, J. Brown, K. Buschelman, W. D. Gropp, D. Kaushik, M. G. Knepley, L. C. McInnes, B. F. Smith, and H. Zhang. (2011) PETSc Web page. [Online]. http://www.mcs.anl.gov/petsc

[113] R. Falgout and U. Yang, "hypre: A library of high performance preconditioners," in *Computational Science — ICCS 2002*, Peter Sloot, Alfons Hoekstra, C. Tan, and Jack Dongarra, Eds.: Springer Berlin / Heidelberg, 2002, pp. 632-641.

[114] E. A. Luke and T. George, "Loci: a rule-based framework for parallel multi-disciplinary simulation synthesis," *Journal of Functional Programming*, vol. 15, no. 03, pp. 477-502, 2005.

[115] P.D. Thomas and C. K. Lombard, "Geometric conservation law and its application to flow computations on moving grids," *AIAA Journal*, vol. 17, no. 10, pp. 1030-1037, 1979.

[116] R. Kamakoti and W. Shyy, "Evaluation of geometric conservation law using pressure-based fluid solver and moving grid technique," *International Journal of Heat and Fluid Flow*, vol. 14, no. 7, pp. 851-865, 2004.

[117] F.R. Menter, M. Kuntz, and R. Langtry, "Ten Years of Industrial Experience with the SST Turbulence Model. In: Hanjalic, K., Nagano, Y., Tummers, M. (Eds.)," *Turbulence, Heat and Mass Transfer 4, Begell House*, pp. 625 - 632, 2003.

[118] F.R. Menter, "Two-equation Eddy-viscosity Turbulence Models for Engineering

Application," *AIAA Journal*, vol. 32, pp. 269 - 289, 1994.

[119] C. Kang, H. Aono, P. Trizila, Y. Baik, J. M. Rausch, L. Bernal, M. V. Ol, and W. Shyy, "Modeling of Pitching and Plunging Airfoils at Reynolds Number between 1x10^4 and 6x10^4," in *27th AIAA Applied Aerodynamics Conference, San Antonio, Texas, June 22-25, 2009*, AIAA-2009-4100.

[120] A. Beckert and H. Wendland, ",Multivariate Interpolation for Fluid-Structure-Interaction Problems using Radial Basis Functions," *Aerospace Science and Technology*, vol. 5, no. 2, pp. 2 - 8, 2000.

[121] P. Khosravi, R. Ganesan, and R. Sedaghati, "Corotational non-linear analysis of thin plates and shells using a new shell element," *International Journal of Numerical Methods in Engineering*, vol. 69, no. 4, pp. 859-885, 2007.

[122] U. Küttler and W. A. Wall, "Fixed-point fluid-structure interaction solvers with dynamic relaxation," *Computational Mechanics*, vol. 43, pp. 61-72, 2008, 10.1007/s00466-008-0255-5.

[123] U. Küttler and W. A. Wall, "Vector extrapolation for strong coupling fluid-structure interaction solvers," *Journal of Applied Mechanics*, vol. 76, no. 2, p. 021205, 2009.

[124] L. Prandtl and O.G. Tietjens, *Fundamentals of Hydro- and Aeromechanics*, trans. L. Rosenhead ed. New York, 1934.

[125] P. G. Saffman, *Vortex dynamics*.: Cambridge Univ Press, 1995.

[126] H. Lamb, *Hydrodynamics*, 6th ed. Mineola: Dover Publications, Inc., 1945.

[127] F. Noca, "On the evaluation of time-dependent fluid-dynamic forces on bluff bodies," California Institute of Technology, PhD thesis 1997.

[128] P. Trizila, C.-K. Kang, H. Aono, M. Visbal, and W. Shyy, "Low-Reynolds-number aerodynamics of a flapping rigid flat plate," *AIAA Journal*, vol. 49, no. 4, pp. 806-823, 2011.

[129] William Graebel, *Advanced fluid mechanics*.: Academic Press, 2007.

[130] T. Theodorsen, "General theory of aerodynamic instability and the mechanism of flutter," NACA report 496, 1935.

[131] M. Ol, L. Bernal, C.-K. Kang, and W. Shyy, "Shallow and deep dynamic stall for flapping low Reynolds number airfoils," *Experiments in Fluids*, vol. 46, no. 5, pp.

883-901, 2009-05-01.

[132] C. Kang, Y. Baik, L. Bernal, M. Ol, and W. Shyy, "Fluid Dynamics of Pitching and Plunging Airfoils of Reynolds Number between 1×10^4 and 6×10^4," in *47th AIAA Aerospace Sciences Meeting including The New Horizons Forum and Aerospace Exposition, Orlando, Florida, Jan. 5-8, 2009*, AIAA-2009-536.

[133] Y. Baik, "Unsteady Force Generation and Vortex Dynamics of Pitching and Plunging," University of Michigan, PhD Thesis 2011.

[134] E. Polhamus, "Predictions of Vortex-Lift Characteristics by a Leading-edge Suction analogy," *Journal of Aircraft*, vol. 8, pp. 193 - 199, 1971.

[135] M. Ol, McAuliffe, Hanff B. R., E. S., U. Scholz, and Ch. Kaehler, "Comparison of Laminar Separation Bubble Measurements on a Low Reynolds Number Airfoil in Three Facilities," in *35th AIAA Fluid Dynamics Conference and Exhibit, Toronto, Ontario, June 6-9, 2005*, AIAA 2005-5149.

[136] J. Tang, D. Viieru, and W. Shyy, "Effects of Reynolds Number and Flapping Kinematics on Hovering Aerodynamics," *AIAA Journal*, vol. 46, pp. 967 - 976, 2008.

[137] H. Aono, S. K. Chimakurthi, P. Wu, E. Sällström, B. K. Stanford, C. E. S. Cesnik, P. Ifju, L. Ukeiley, and W. Shyy, "A computational and experimental study of flexible flapping wing aerodynamics," in *48th AIAA Aerospace Sciences Meeting Including the New Horizons Forum and Aerospace Exposition, Orlando, Florida, January 4-7,2010*, AIAA-2010-554.

[138] S. Timoshenko, D. H. Young, and JR. W. Weaver, *Vibration problems in engineering*.: John Wiley & Sons, Ltd., 1974.

[139] R. D. Mindlin and L. E. Goodman, "Beam vibrations with time-dependent boundary conditions," *Journal of Applied Mechanics*, vol. 17, pp. 353-356, 1950.

[140] J. P. Whitney and R. J. Wood, "Aeromechanics of passive rottion in flapping flight," *Journal of Fluid Mechanics*, vol. 660, pp. 197-220, 2010.

[141] A. P. Willmott and C. P. Ellington, "The mechanics of flight in the hawkmoth Manduca sexta. I. Kinematics of hovering and forward flight," *Journal of Experimental Biology*, vol. 200, pp. 2705-2722, 1997.

[142] A. P. Willmott and C. P. Ellington, "The mechanics of flight in the hawkmoth Manduca sexta. II. Aerodynamic consequences of kinematic and morphological variation," *Journal of Experimental Biology*, vol. 200, pp. 2723-2745, 1997.

[143] R. Buchwald and R. Dudley, "Limits to vertical force and power production in bumblebess (Hymenoptera: Bombus impatiens)," *Journal of Experimental Biology*, vol. 213, pp. 426-432, 2010.

[144] S. Vogel, "Flight in Drosophila: I. Flight performance of tethered flies," *Journal of Experimental Biology*, vol. 44, pp. 567-578, 1966.

[145] E. Shevtsova, C. Hansson, D. H. Janzen, and J. Kjaerandsen, "Stable structural color patterns displayed on transparent insect wings," *Proceedings of National Academy of Science*, vol. 108, no. 213, pp. 668-673, 2011.

[146] C. J. Pennycuick, "Wingbeat Frequency of Birds in Steady Cruising Flight: New Data and Improved Predictions," *Journal of Experimental Biology*, vol. 199, pp. 1613 - 1618, 1996.

[147] B. Yin and H. Luo, "Effect of wing inertia on hovering performance of flexible flapping wings," *Physics of Fluids*, vol. 22, p. 111902, 2010.